EVOLVE
Final Report

by

C.P.C. WONG, L. BARLEON, M.H. ANDERSON, J.G. MURPHY, M.E.
SAWAN, I.N. SVIATOSLAVSKY, M.L. CORRADINI,
S. MALANG, S. ZINKLE, B. NELSON, P. FOGARTY,
S. SHARAFAT, N. GHONIEM, S. MAJUMDAR, R. MATTAS,
B. MIRRILL, K. McCARTHY, R. NYGREN,
and D.L. YOUCHISON

OCTOBER 2002

EVOLVE
Final Report

by
C.P.C. WONG,[*] L. BARLEON,[*] M.H. ANDERSON,[†] J.G. MURPHY,[†]
M.E. SAWAN,[†] I.N. SVIATOSLAVSKY,[†] M.L. CORRADINI,[†]
S. MALANG,[‡] S. ZINKLE,[△] B. NELSON,[△] P. FOGARTY,[△]
S. SHARAFAT,[#] N. GHONIEM,[#] S. MAJUMDAR,[§] R. MATTAS,[§]
B. MIRRILL,[◆] K. McCARTHY,[◆] R. NYGREN,[□]
and D.L. YOUCHISON[□]

[*]General Atomics, San Diego, California.
[†]University of Wisconsin, Madison, Wisconsin.
[‡]Forschumgszentum Karlsruhe GmbH, Karlsruhe, Germany.
[△]Oak Ridge National Laboratory, Oak Ridge, Tennessee.
[#]University of California, Los Angeles, California.
[§]Argonne National Laboratory, Argonne, Illinois.
[◆]Idaho National Engineering Laboratory, Idaho Falls, Idaho.
[□]Sandia National Laboratories, Albuquerque, New Mexico.

OCTOBER 2002

EVOLVE FINAL REPORT

C.P.C. Wong, L. Barleon (consultant)
General Atomics,
P.O. Box 85608,
San Diego, California 92186-5608
(858) 455-4258

M.H. Anderson, J.G. Murphy, M.E. Sawan, I.N. Sviatoslavsky and M.L. Corradini
University of Wisconsin
1500 Engineering Dr.
Madison, WI 53706
(608) 265-4186

S. Malang
Forschungszentum Karlsruhe GmbH
Postfach 3640
D-76021 KARLSRUHE
Germany
07247 824101

S. Zinkle, B. Nelson, P. Fogarty
Oak Ridge National Laboratory
Oak Ridge, Tennessee

S. Sharafat, N. Ghoniem
University of California
Los Angeles

S. Majumdar, R. Mattas
Argonne National Laboratory
Argonne, Illinois

B. Merrill, K. McCarthy
INEEL
Idaho

R. Nygren, D.L. Youchison
Sandia National laboratories
Albuquerque, New Mexico

Table of Contents

Table of Contents (continued)

Table of Contents (continued)

Table of Contents (continued)

List of Figures

List of Figures (continued)

List of Figures (continued)

List of Figures (continued)

List of Figures (continued)

List of Tables

Abstract

This report presents the results of the second phase evaluation of the EVOLVE W-alloy first wall blanket design cooled by vaporized lithium, which is also called the transpiration-cooled first wall design. For the transpiration-cooled first wall and blanket concept, we identify the need to further quantify the data of lithium superheat from W-alloy heated surface and bulk lithium slabs. For the boiling lithium blanket we identify the need to elucidate the impacts of magnetic field on various stable-boiling regimes. We also find that this FW/blanket concept should have no problem in achieving adequate nuclear performance. With the addition of passive cooling loops, the concept has a strong possibility of achieving the safety requirement of not needing a public evacuation plan under the loss of power accident conditions. Even though the irradiated W-alloy could have projected problems in embrittlement, it is shown to be able to withstand large number of cracks due to the relatively low system pressure of the design. The fundamental issues of W-alloy properties under high neutron fluence and the technique of components fabrication remain. Preliminary investigations of W-alloy fabrication and heat flux removal through the Small Business Innovative Research (SBIR) programs have begun and the initial results are encouraging. We recommend that the investigation of critical issues of the EVOLVE concept should continue since this innovative design has a good possibility of showing a way to achieve high performance and passively safe designs that are necessary for the utilization of fusion power.

1. Introduction

To achieve high thermal performance at high power density, the Evaporation of Lithium and Vapor Extraction (EVOLVE) W-alloy first wall and blanket (FW/blanket) concept proposes to use the vaporization of lithium to remove the FW/blanket thermal power. The lithium is maintained at the saturation pressure of 0.037 MPa, and a high lithium vapor outlet temperature of 1200°C. When coupled to a helium closed cycle gas turbine system, a thermal efficiency of ~57% can be projected. The scoping design of this FW/blanket concept was completed at the first phase of the APEX work [1]. The basic design of the EVOLVE first wall boiling blanket configuration is shown in Figure 1-1. The first wall is composed of toroidally oriented tubes. Inside these tubes there are smaller feeding tubes connected to the first wall fluid channel formed by the capillary screen on the one side and the first wall on the other side. The blanket design schematic in Fig. 1 shows the lithium blanket trays. The lithium is fed from the top of the tray and fills up the top tray before it is overfilled and drained to the tray just beneath the top one. This process of overfilling the top tray and draining to the lower tray forms the supply approach of the lithium coolant. The vaporized lithium comes off the lithium surface and moves to the outlet vapor plenum located at the back of the blanket. For the second phase of the EVOLVE concept evaluation, we focused on addressing critical issues. When evaluating the vaporizing lithium first wall design we noticed that this approach can also be used for the blanket design, which we called the transpiration cooled blanket design as described in Chapter 3 of this report. After the introduction, this report begins with a description of the FW/blanket configuration. Detailed analyses of the thermal-hydraulics of the transpiration-cooled FW and transpiration-cooled blanket design are then presented. The boiling blanket analysis and proposed MHD experiment are then described. The issues of coolant leakage to the plasma chamber and passive safety were addressed. The neutronics performance of both boiling blanket and transpiration-cooled blanket approaches are presented. The initial demonstration of W-alloy fabrication and recent developments are also presented in this report. Critical issues of the EVOLVE design and conclusions from our work are then presented in the last chapter.

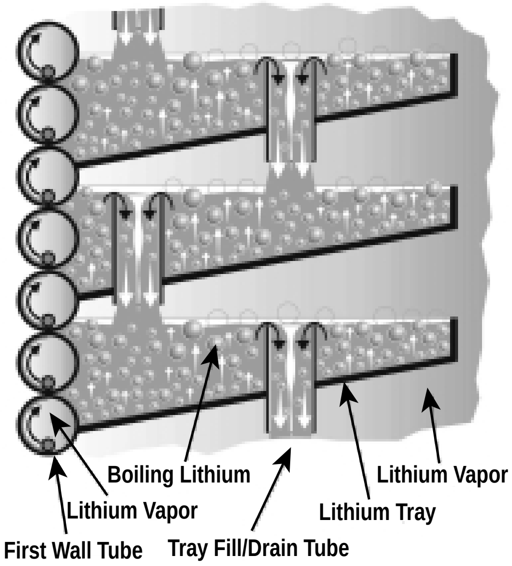

Figure 1-1. Schematic of EVOLVE first wall and boiling blanket concept.

Reference

[1] APEX Interim Report, “On the Expoloration of Innovative Concepts for Fusion Chamber Technology,” UCLA report, UCLA-ENG-99-206, UCLA-FNT-107, November 1999.

2. Configuration and Basic Design Description

The EVOLVE FW/blanket concepts are based on a modified ARIES-RS tokamak geometry. The same overall dimensions and the same replacement scheme (sector replacement through individual horizontal ports) is used for the EVOLVE concept. However, a single divertor located at the bottom replaces the double-null divertors and the FW/blanket/shield is divided into upper and lower halves in order to reduce size and flow path length of the coolant manifolds. Figure 2-1 shows a vertical cross section of the torus and the maintenance port. In the EVOLVE concept, the first wall and primary breeding zone are combined into one unit.

Behind this unit, there is as a separate component a high temperature shield at the inboard region and a secondary breeding blanket at the outboard region. Behind the secondary breeding zone there is, as a separate component, an additional high temperature shield in order to meet the shielding requirements of vacuum vessel and magnets.

The same coolant (lithium) and structural material is used in all FW/breeding zones/shields. Reference structural material is tungsten or a tungsten rhenium-alloy. An alternative material is a tantalum alloy, which is more ductile and more workable than tungsten. Tungsten has, however, considerably higher thermal conductivity, higher strength at operating temperature, and better compatibility with lithium.

An additional advantage of tungsten is the higher breeding rate achievable with this structural material. Another option is a combination of the two materials where the large elements of the structure are fabricated of W and some connection elements are made of Ta in order to combine the better neutronics features and the lower cost of W with the higher ductility and better weld-ability of Ta. Tungsten carbide is used as an efficient shielding material. Novel ideas are employed for the first wall and the primary breeding zone and these concepts will be described in some detail. The secondary breeding zone is a self-cooled blanket with lithium as a breeder and coolant. These components, as well as the high temperature shields, are more or less "standard" designs that have not been detailed in the context of this study.

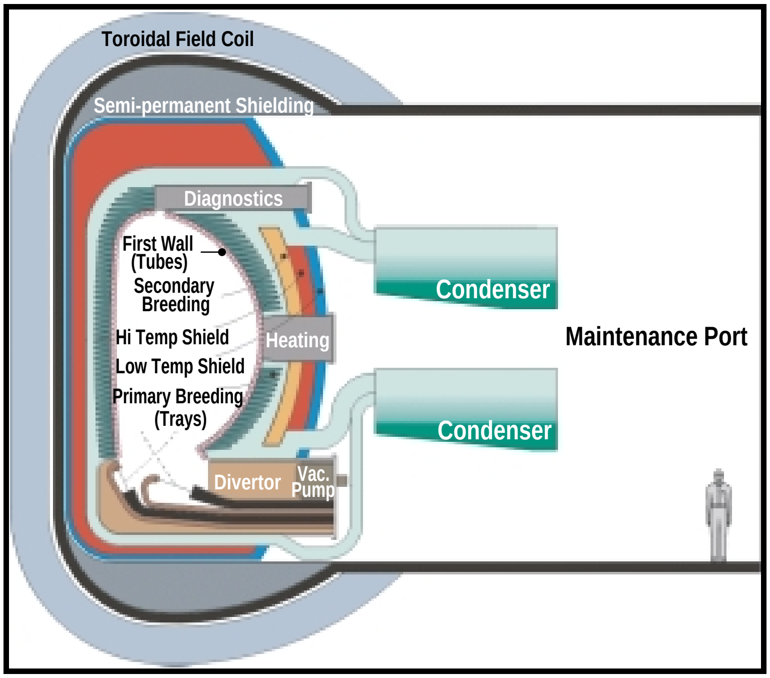

Figure 2-1. EVOLVE Concept – cross section.

2.1. First Wall Design-Option One

The basic design of the concept is shown in Figures 2-1 and 2.1-1. We studied two options of the first wall design. The first option is composed of U-shaped tubes, running in radial-toroidal-radial direction. Inside these tubes there are smaller feed tubes connected to the first wall feeding channels to cool the FW by vaporization. The diameter of this tapered feed tube has a maximum at the entrance and goes to zero at the exit, giving there the entire space to the vapor flow. Details of the thermal-hydraulics of this first wall design are presented in Chapter 3.

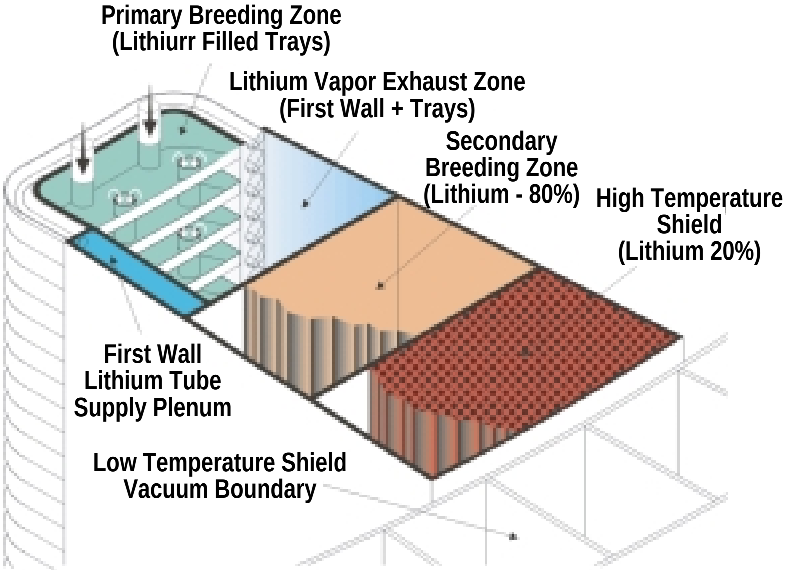

Figure 2.1-1. Cutaway view of a 7.5° segment showing a proposed first wall concept.

Given the large heat flux into the first wall, its thickness has to be kept to a minimum in order to minimize temperature differences and thermal stresses. This is facilitated by the low vapor pressure and circular tube geometry, allowing a wall thickness of less than 3 mm. Typical dimensions for the vapor tubes and the feed tubes are inner diameters of 50 mm and 10 mm respectively. For a surface heat flux of 2 MW/m^2, a toroidal segment width of 3 m, and the tube dimensions given above, a boiling temperature of 1200°C (saturation pressure 0.035 MPa) results in a liquid metal velocity in the feed tube of about 1 m/s and a vapor velocity of about 500 m/s. This is about 1/3 of the sonic velocity and results in a tolerable pressure drop. It is suggested to “overfeed” the FW by about 50% to avoid any dry-out. This means that the vapor at the exit of the tube will have entrained some liquid metal that will be separated in the manifold. In the present EVOLVE concept, there are combined vapor manifolds for the first wall and primary breeding zone.

2.2. First Wall Design-Option Two

Figure 2.2-1 shows the second configuration of the EVOLVE FW/blanket design, which is a transpiration-cooled first wall and boiling lithium blanket concept. This concept has a more complicated configuration than the boiling blanket option, but it has the advantage of a very passive system. Whereas the boiling blanket design has a much simpler configuration but requires the identification of stable operating regimes of boiling lithium in a magnetic field. Since both are innovative concepts that have no previous applications, we decided to evaluate

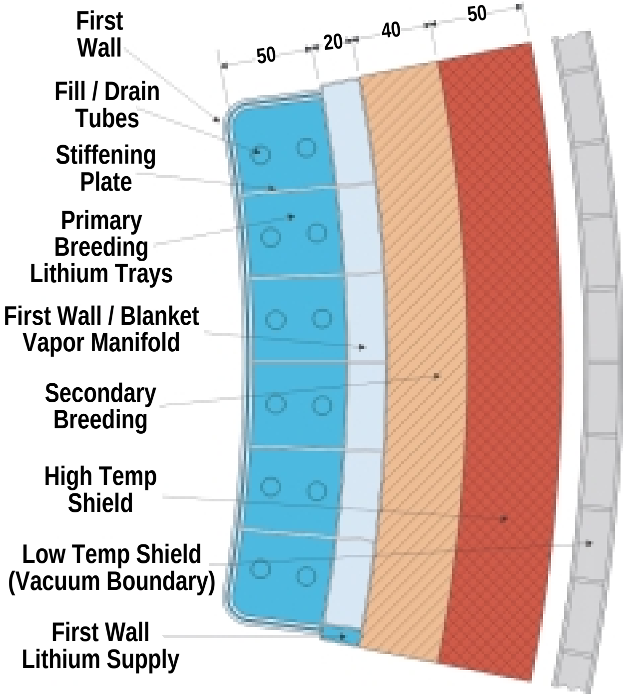

Figure 2.2-1. Midplane cross section of a 22.5° segment.

both transpiration-cooled and boiling-cooled blanket options and the results are summarized in the following chapters. For the second configuration we evaluated the concept under the same set of parameters as before, where the lithium vapor is nominally at 1200°C and saturated pressure of 0.037 MPa, with a first wall surface heat flux of 2 MW/m^2 and a neutron wall loading at 10 MW/m^2.

2.2.1. The Transpiration-Cooled First Wall and Blanket Concept with poloidal First Wall Channels

In the transpiration-cooled concept the heat from the solid first wall and the volumetric heat deposited in the blanket is removed by evaporation through capillary walls. The porous structure of these walls pumps the lithium by the capillary effect out of a sump to the evaporating surface formed by the capillaries with the diameter d_c. Additionally the fluid height in the tray is used to support this passive capillary pumping. Concepts with toroidal and poloidal oriented first wall channels are investigated. For the poloidal flow first wall design the routing of the liquid and vapor lithium of the poloidal flow first wall design is shown schematically in Figure 2.2-2, and the orientation of the magnetic field is indicated. The coolant lithium is routed from the back of the blanket to the bottom of the vertical blanket slab to the first wall and then through the first wall channel defined by the capillary sheet. The thin, 0.5 mm thick capillary sheet defines a first wall channel width (w) of 0.75 mm on the inner side of the first wall.

In the blanket region 2 mm thick capillary sheets are also used everywhere insuring transpiration cooling of the Li-slab held within the sheets and within the back and bottom ducts feeding the Li to the first wall channels. The vaporized Li from the capillaries is escaped between the lithium slabs. The transpiration-cooled concept works when the sum of the active and passive pumping head is higher than the total system pressure losses and when the temperature at the inner side of the first wall does not override the superheating limit of the coolant which would be about ΔT_{SH}=100 K for very smooth surfaces. The pressure losses, especially in the liquid Li, are

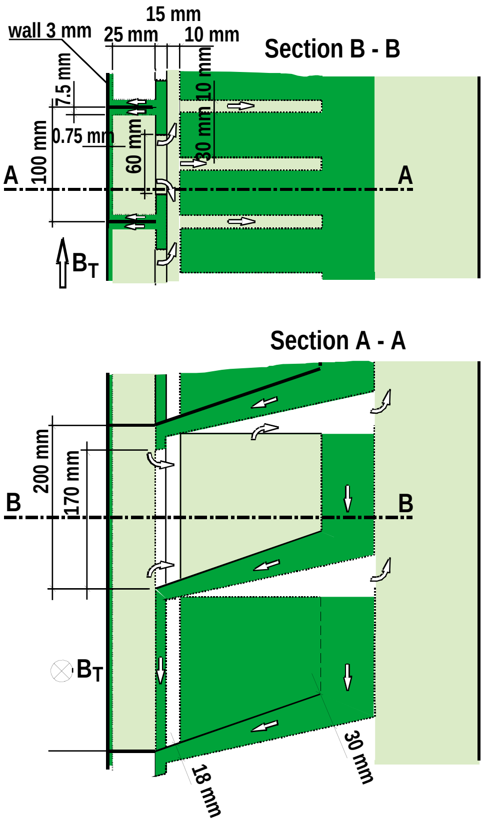

Figure 2.2-2. Transpiration cooled EVOLVE concept with poloidal first wall channels, all sketches out of scale.

governed by magnetohydrodynamic (MHD) effects induced by the strong magnetic field and the pressure jump across the evaporation capillary surface. The first wall feeding gap width w is the critical dimension that determines both the first wall MHD pressure drop and the coolant temperature at the first wall. The selected width of 0.75 mm has been optimized for this design. The width of the different liquid Li slabs, which is blanket heated volumetrically and cooled at their surfaces by transpiration cooling, is defined by the maximal allowed superheating at their centerline. For this case the superheat of 100 K was assumed before the formation of homogeneous nucleation. Details of these analyses are presented in Chapter 3.

2.3. Primary Breeding Zone

Use of lithium evaporation cooling in the breeding zone in combination with the FW cooling described above offers a number of advantages:

- Only one coolant is required.
- Required liquid metal flow rate is almost a factor of ten lower than in a self-cooled lithium blanket.
- High heat transfer typical for boiling liquid metals results in exceptionally low temperature variation in the blanket, and thus, in minimized thermal stresses.
- Low vapor pressure (reference value 0.035 MPa) leads to low primary stresses.
- High vapor temperature allows for a high efficiency power conversion system.

The blanket design option one, boiling trays design of the breeding zone can be seen in Figures 2.3-1 and 2.3-2. Flat trays are used as lithium containers in order to facilitate the vapor separation. Each tray contains a lithium pool with a height of 10 to 20 cm, which is maintained constantly by a system of overflow tubes. The large volume heating of the lithium could lead to rather violent boiling.

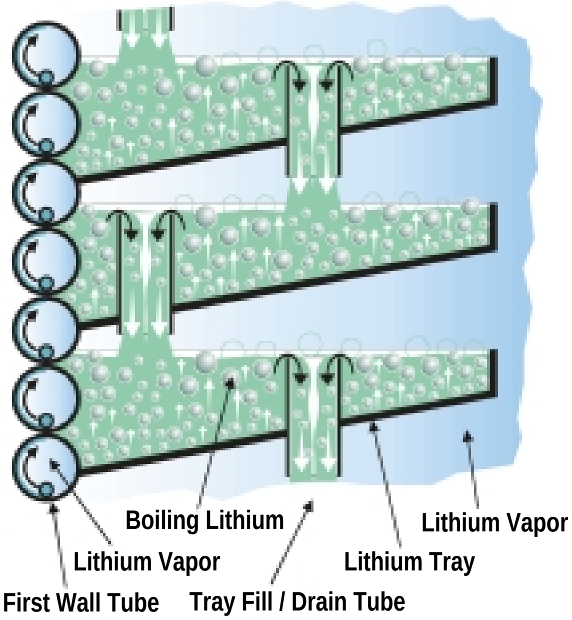

Figure 2.3-1. Secondary breeding zone schematic.

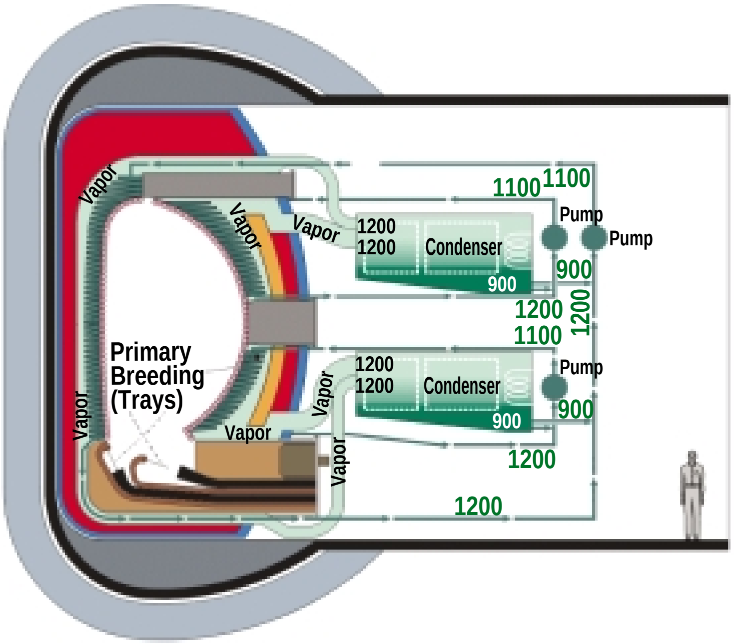

Figure 2.3-2. High temperature shield schematic.

The vapor bubbles have to rise in the pool and separate from the liquid metal at the surface. From here the vapor flows a short distance in parallel to the surface before it enters the vertical vapor manifold. Entrained liquid metal will be separated there.

The principle of the overflow system for maintaining constant lithium levels in all trays is also shown in Figure 2.3-1. There is a fill pipe at the top of the stack and a drainpipe at the bottom of it. There will always be excess flow at the top in order to assure that all trays are full. This means that at the bottom, continuous draining of a fraction of the total flow rate is required. The trays have a thickness of ~5 mm and are fabricated from flat sheets. They are attached to the FW, which is composed of a tube bank. The concept requires neither high precision in the fabrication nor high quality welds. Even large leaks between tray and FW tubes can be tolerated. The poloidal distances between the trays must be optimized with the goal of providing sufficient space for the vapor flow but avoiding large gaps for neutron streaming. A flat plate with a thickness of ~10 mm is used to close the vapor manifold in the radial direction. Stiffening plates connect it in the radial direction to the U-shaped FW box to support this plate. During operation, there is a vacuum at the outside of the component and a vapor pressure of 0.035 MPa at the inside, resulting in exceptionally low primary stresses. Due to the boiling heat transfer at the inside, the temperature of the structure will be close to the boiling temperature of the lithium and the total temperature variation will be very small, resulting in low thermal stresses.

2.4. Secondary Breeding Zone And High Temperature Shield

The total fraction of lithium in the primary breeding zone shown in Figure 2.3-1 is rather low due to the gaps for vapor flow between trays, the vapor content in the lithium pools, and the low specific lithium density at boiling temperature. Increasing the Li enrichment can increase a resulting low tritium-breeding ratio. There is still a need for arranging a secondary breeding zone in the outboard region where the space is not limited as much as in the inboard side. The neutron flux in the secondary breeding zone is considerably lower than at the front, allowing the use of a variety of blanket concepts. For simplicity reasons however, a self-cooled lithium/tungsten blanket concept has been selected as a reference solution in order to limit the number of materials used and to allow the generation of high-grade heat in this zone too as shown in Figure 2.4-1. The low volumetric heat generation and the absence of a surface heat flux probably enables a design without insulating coatings, where the MHD pressure drops are kept to a tolerable level by using thin-walled flow channel inserts. Neither design work nor analyses have been performed for this concept in the context of this study, because self-cooled blanket concepts have been investigated in a number of blanket and power plant studies. The same statements can be applied to the high temperature shields as shown in Figure 2.4-2, required both at the inboard and the outboard region for additional neutron shielding of vacuum vessel and magnets. They are also made of tungsten as structural material, cooled by flowing lithium. Tungsten carbide is used as shielding material. Reasonable assumptions about the volume composition of these components have been made for the neutronics analysis.

2.5. Primary Cooling Loops

Lithium is used as a primary coolant for all components (FW, Primary breeding zone, secondary breeding zone, high temperature shield) as shown in Figure 2.3-2. About 2/3 of the total heat is extracted by lithium vapor at a temperature of 1200°C, the remaining 1/3 by the liquid metal cooling of the secondary breeding zone and the shields. The heat sink for both loops are the lithium/helium heat exchangers where the helium of the closed cycle gas turbine power conversion system is heated up to about 1000°C. In the evaporation loop, the entire heat is transferred to the secondary helium by condensation. Due to the pressure drop in the vapor flow and vapor pressure, a consequence of this is that the saturation temperature will decrease. This means, that the liquid metal will exit from the IHX with a temperature of 900°C to 1000°C. It is probably advantageous to pre-heat this liquid metal flow to about 1100°C with a small by-pass flow of high temperature vapor before it enters the blanket in order to minimize thermal stresses. Figure 2.5-1 shown below is an overall flow schematic denoting inlet and outlet operating temperatures.

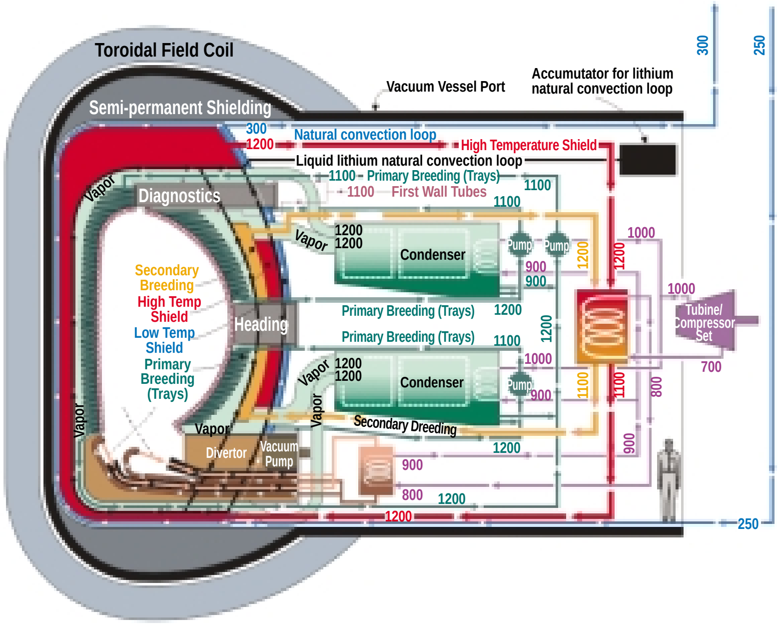

Figure 2.5-1. Primary cooling loops/flow schematic.

The liquid metal temperatures in the convection-cooled components can be chosen in a large range to optimize the power conversion system. The structure must be kept above 800°C in order to avoid embrittlement. The upper temperature limit is determined by compatibility issues, which would allow for tungsten/lithium values up to 1400°C. A third limitation for the allowable temperature range is set by the temperature rise between coolant inlet and outlet. Temperature rises above 200°C should be avoided in order to keep thermal stresses small. Altogether it may be advantageous to operate the convection loop between 1100°C at the inlet and 1200°C at the outlet at about the same level as the evaporation loop in order to minimize differential thermal expansion. Heat transfer in the HX of the evaporation loop is at the primary side by condensation and therefore very effective. There is a large temperature difference available for heat transfer to the helium in the convection loops. Both of these facts together minimize the heat transfer surface area in the HX.

The relatively small size of these HX enables a design where the entire lithium loops, including the intermediate heat exchanger, are located inside the horizontal maintenance ports. There is one port anticipated for each torus sector in order to speed up blanket replacement by exchanging the entire sector. Figure 2.5-2 illustrates sector removal. This offers the possibility to design modular heat exchangers, two for every torus sector (upper and lower halves). The result of this is an advantage in regard to safety and availability.

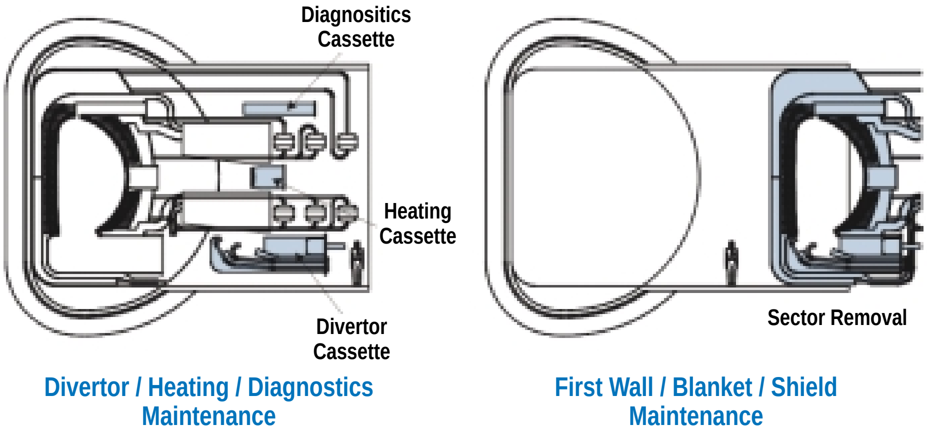

Figure 2.5-2. Component replacement/maintenance.

Keeping the entire amount of lithium inside the vacuum chamber minimizes the risk of chemical reaction between lithium with water, air, concrete or other gases. Malfunctions in the cooling system of one sector will not have an impact on the function of the other sectors and thus provides for functioning heat sinks for radiating the after heat from a failed sector. The downtime for a blanket exchange, and consequently, the availability of the blanket system, is increased by this design because no liquid metal coolant lines have to be cut and re-welded inside the plasma chamber during a blanket replacement. The argument that the relatively large number of HX has a negative impact on the failure rate is not valid because the number of heat exchanger tubes mainly determines this failure rate, which is independent from the degree of modularization. The arrangement of the IHX inside the vacuum vessel implies a risk of pressurization in case of a tube rupture. This risk has to be avoided by locating suitable rupture disks for a fast release of the accidental helium pressure.

2.6. Power Conversion System

A natural choice for the power conversion system is a closed cycle gas turbine system, since the heat is extracted from the first wall and blankets at temperatures above 1000°C. A thermal efficiency up to 57% is achievable in such a system with these high temperatures.

Additional advantages of this Brayton cycle compared to a Rankin steam turbine cycle are smaller problems with tritium permeation losses to the environment and the possibility to use heat exchanger materials not compatible with steam or impurities in helium. Tritium permeation losses are minimized by the fact that the only connection to the environment is the low temperature HX at the heat rejection system, and the intercooler between the different compression stages.

The impurity level in the helium can be maintained at very low values since there are no sources for ingress of oxygen, water vapor or other gases. This means that it is possible to remove impurities by hot trapping to very low concentrations prior to heating up the heat exchanger to operating temperatures. This would not help in a system with helium/steam HX where unavoidable micro leaks would always be a source for impurities.

3. Transportation FW, Blanket and Experiment

3.1 Introduction

In designing liquid metal (LM) cooled blankets of fusion reactor with magnetically confined plasma one has to deal with two special features:

- High peak heat load at the first wall, and the
- Magneto-hydrodynamic (MHD) effect of circulating LM coolants in a magnetic field.

The maximum allowable temperature of the structural material, which requires intensive cooling, limits the peak heat flux at the first wall. This usually means a good heat transfer from the first wall to the coolant together with a low coolant temperature, which means low coolant temperature increase. But a good heat transfer and low temperature increase can only be obtained by circulating the LM at high velocity, which leads to high MHD pressure drop. The MHD-flow pressure drop of LM (i.e. slug flow profile and strongly reduced turbulence) can be approximated by a simple correlation in non-electrically insulated channels perpendicular to the applied B-field, B, and is given by:

$$\Delta P \propto C \cdot \frac{q_0''^{2} \cdot L^2}{\Delta T^2} \qquad \text{where, } C = f\left(B^2, \frac{t_w \cdot \sigma_w}{a \cdot \sigma_{LM}}, F_{Geometry}\right)$$

q_0'' = heat flux on the first wall,
L = heat exposed length,
ΔT = coolant temperature increase,
σ_w = wall electrical conductivity,
σ_{LM} = LM electrical conductivity,
t_w = channel wall thickness.
a = channel width,
$F_{Geometry}$ = geometric factor.

The restricted ΔT together with the strong dependence on the heated length L limits the LM cooling of a fusion blanket to moderate heat flux q_0'' on the first wall. The challenge is to increase the heat transfer while keeping the velocity of the circulating LM low.

If we compare for example the heat, which can be transported with lithium at 1200°C by a temperature increase of ΔT= 200°C and with evaporative cooling one gets

Convective Cooling	Evaporative Cooling
$Cp \times \Delta T$	H_{Li}
4.4×10^5 J/kg	2.0×10^7 J/kg

We can see that evaporative cooling will be able to remove about 45 times more energy than convective cooling per unit mass of lithium.

This chapter presents how design concepts would look like with evaporative cooling when applied to the EVOLVE concept as presented in previous chapters. In the first part of this chapter the evaporative cooling of the first wall is outlined, and in the second part the analysis and results on the evaporation cooling of the blanket zones are presented. We then present the critical issues for this cooling approach and identify issues that will need further analysis or experimental investigation.

During the evaluation of cooling by evaporation, the question of a self-controlled lithium supply channels came up. Since all the supply channels also have to be cooled, we applied the same technique for the first wall cooling, which is by evaporation through a porous wall. This general approach we call it the transpiration cooling in the rest of this chapter.

3.2. Modeling and Analysis of the First Wall Cooling

Following sections present the models used and the analysis of the first wall cooling of the EVOLVE concept.

3.2.1. The Toroidal First Wall Cooling Tube Concept

Figure 3.2-1 shows schematically the cross section through the circular tube first wall, the capillary structure and the gap through which the liquid lithium is transported to the capillaries. The figure shows the separate functions of feeding, pumping and evaporation of lithium. The lithium is fed through an azimuthal gap of the width w and is evaporated and pumped in a capillary of diameter d_C. For the analysis the following simplifying assumptions and approximations are made: the toroidal field, B_T is exactly aligned with the tube, the magnetic field perpendicular to the tube is given by $B_\perp = B_p \times \cos \alpha$ where the poloidal field, B_p is approximated by 1/10 B_T.

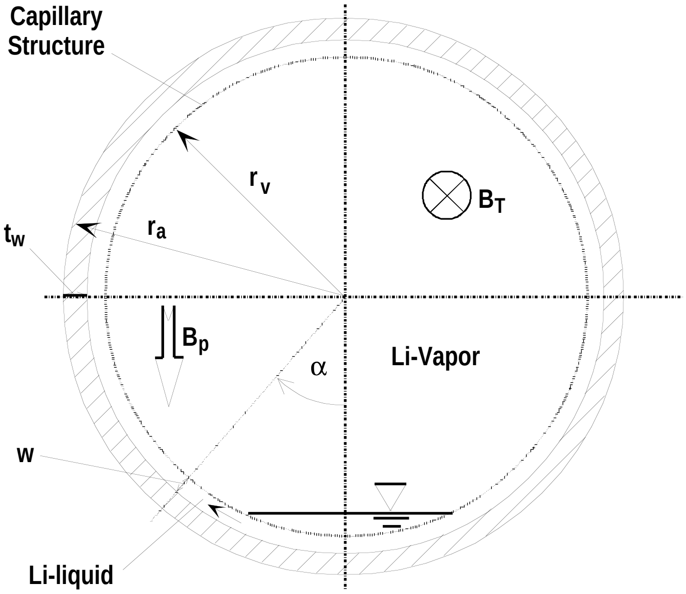

Figure 3.2-1. Schematic of the cross section through the toroidal first-wall cooling channel.

The importance of the assumption of the B_T being exactly aligned with the first wall channel will be highlighted when the influence of the B_p on capillary pumping is shown later in this chapter.

The principle of capillary pumping and evaporation is shown schematically in Figure 3.2-2 for a vertical structure. The corresponding configuration with toroidal (B_T) and poloidal (B_{pol}) fields are shown in Figure 3.2-3. With the help of the relatively simple correlations the dependence of the pumping pressure ΔP_c from the diameter of the capillary and the dependence of the MHD pressure drop ΔP_{MHD} on the feeding gap width w have been investigated and the need to separate the two functions, feeding and pumping is also illustrated. In the following, σ_s is the surface tension of lithium at saturation temperature, and λ is the thermal conductivity of the W-alloy first wall. T_{wP} and T_{wl} are the wall temperatures facing the plasma and the lithium, respectively and T_s is the lithium free surface temperature in the capillary corresponding to the saturation temperature. $QF \equiv q_0$ is the heat flux and $\Delta T_{superheat}$ is the superheat temperature between the lithium and the W-alloy surface.

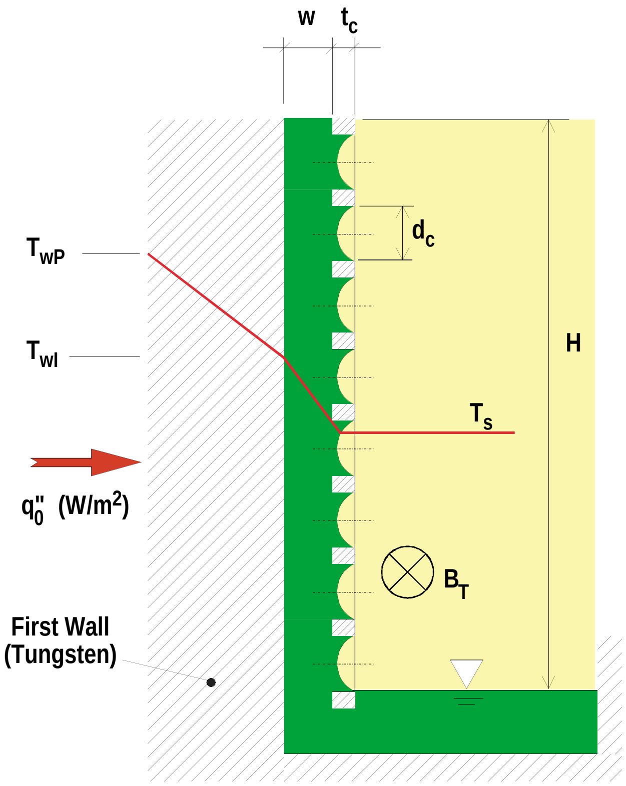

Figure 3.2-2. Evaporation cooling of a high heat loaded wall through a porous structure.

$$\Delta P_c = \frac{4 \cdot \sigma_s}{d_c} \propto \frac{1}{d_c} \qquad \text{and} \qquad T_{wl} - T_s = \frac{q_0'' \cdot w}{\lambda_{Li}} \leq \Delta T_{Superheat}$$

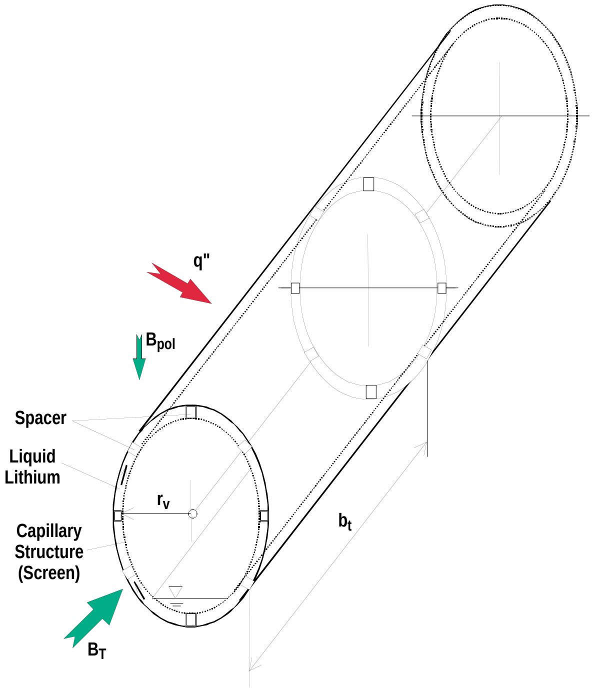

Figure 3.2-3. Capillary cooling, showing the capillary structure with the spacers, the direction of the heat flux and the toroidal and poloidal magnetic field components.

3.2.1.1. The pressure balance

In order to keep the lithium mass balance between the lithium evaporated in the capillary and the lithium fed from the sump the capillary pumping pressure Δp_c has always to be higher than the sum of all pressure losses of the lithium along its flow path. This forms the limiting condition for the design as shown in the following equation.

$$\Delta p_c \geq \Delta p_{H1} + \Delta p_{H2} + \Delta p_{H3} + \Delta p_{M1} + \Delta p_{M2} + \Delta p_{M3} + \Delta p_{LV} \tag{3.2.1}$$

where Δp_c = capillary pressure head,
Δp_{H1} = hydrostatic pressure head of the liquid,
Δp_{H2} = pressure drop of the liquid in the feeding gap,
Δp_{H3} = pressure drop of the liquid in the capillary,
Δp_{M1} = MHD pressure drop in the feeding gap due to the poloidal field,
Δp_{M2} = MHD pressure drop in the feeding gap due to the toroidal field,
Δp_{M3} = MHD pressure drop in the capillary due to the toroidal field,
Δp_{LV} = the pressure jump through the evaporation surface.

For our analysis the following parameters are selected for the calculation:

Outer tube radius (m)	$r_a = 0.03$
Wall thickness (m)	$t_w = 3.0\times10^{-3}$
Tube length (m)	$l_{ax} = 3.00$
Surface heat flux (MW/m^2)	$q''_0 = 2.0$
Toroidal magnetic field strength (Tesla)	$B_T = 6.0$
Thickness of the capillary structure (m)	$t_c = 0.5\times10^{-3}$
Area fraction of the capillaries	$\Delta_c = 0.5.$

3.2.1.2. The effective heat flux q''_{eff} at the feeding gap

For thermohydraulic calculations of the first wall channel an effective heat flux at the first wall will be used, which takes into account the surface heat flux and the heat flux generated by volumetrically heating of the first wall and the lithium within the feeding gap.

$$q''_{eff} = \frac{r_a}{r_v} \cdot q''_0 + t_{FW} \cdot \bar{q}''_{FW} + w \cdot \bar{q}''_{Li,gap} \tag{3.2.2}$$

where r_a is the outer and r_v is the inner radius of the capillary structure (screen), t_{FW} is the thickness of the first wall, w is the thickness of the lithium feeding gap, $\bar{q}''_{FW}$ is the heat flux at the first wall, $\bar{q}''_{FW}$ is the averaged volumetric power density in the tungsten first wall, and $q_{Li,gap}$ is the averaged volumetric power density of the lithium in the gap.

3.2.1.3. Pressure losses of the lithium flow loop

In the following we present the calculations of different pressure drop contributions as shown in Eq. (3.2.1).

The Capillary Pressure Head. The hemispherical shape of the surface of a liquid in a capillary causes a pressure difference across the surface, which can be written as [1],

$$\Delta p_C = \frac{2 \cdot \sigma s_{Li} \cdot \cos\theta}{r} \tag{3.2.3}$$

where σs_{Li} is the surface tension of the liquid lithium at the saturation temperature,
θ is the contact angle of the wetting lithium, and
$r = d_c/2$ is the radius of the capillary.

At temperatures above 900°C (1173 K) lithium wets the tungsten structures completely and the contact angle θ goes to zero and the $\cos\theta \sim 1$.

The Hydrostatic Pressure. The hydrostatic pressure is given by

$$\Delta p_{H1} = \rho_{Li} \cdot g \cdot r_v \cdot (1 - \cos\alpha) \tag{3.2.4}$$

where ρ_{Li} is the lithium density, g = 9.81 m/s^2 the gravity constant, r_v the inside radius of the capillary structure insert and α the angle of the specific position considered as shown in Figure 3.2-1. At full height $\alpha = \pi$, and

$$\Delta p_{H1} = \rho_{Li} \cdot g \cdot 2 \cdot r_v \quad .$$

The change of the mass flow rate $d\dot{m}(l)$ at an azimuthal position l of the heated circumference from lithium evaporation at a first wall surface element of $dl \cdot x$ to remove the heat flux $q''(l)$ is given by,

$$d\dot{m}(l) = -\frac{q''(l) \cdot x}{H_{Li}} \cdot dl \tag{3.2.5}$$

where $q''(l) = q''_{eff} \cdot \sin\alpha$ with x as the distance along the tube, $l = r_v \cdot \alpha$ and $dl = r_v \cdot d\alpha$, we get,

$$d\dot{m}(l) = -\frac{q''_{eff} \cdot \sin\alpha \cdot x}{H_{Li}} \cdot r_v \cdot d\alpha$$

and H_{Li} is heat of vaporization of the lithium.

Integrating $\dot{m}(l)$ over α and taking into account that the total mass flow rate needed to cool a tube with the length x equals to:

$$\dot{m}_{tot} = \frac{q''_{eff} \cdot 2 \cdot r_v \cdot x}{H_{Li}} \tag{3.2.6}$$

we get for the α-dependent mass flow rate,

$$\dot{m}(\alpha) = \frac{q''_{eff} \cdot r_v \cdot x}{H_{Li}} \cdot (1 + \cos\alpha) \quad . \tag{3.2.7}$$

The α-dependent flow velocity $v(\alpha)$ in the feeding gap of the width w can be calculated from the α-dependent mass flow rate $\dot{m}(\alpha)$ as,

$$v(\alpha) = \frac{\dot{m}(\alpha)}{\rho_{Li} \cdot w \cdot x} = \frac{q''_{eff} \cdot r_v}{\rho_{Li} \cdot w \cdot H_{Li}} \cdot (1 + \cos\alpha) \quad . \tag{3.2.8}$$

<u>Pressure Drop of the Liquid in the Feeding Gap.</u> For a thin gap, the pressure drop is given by [1]

$$\Delta p_{H2} = \frac{12 \cdot \mu_{Li} \cdot \dot{m}(l)}{x \cdot w^3 \cdot \rho_{Li}} \quad . \tag{3.2.9}$$

Using $\dot{m}(\alpha)$ from Eq. (3.2.7) the pressure gradient along the circumference l can be written as:

$$\frac{dp_{H2}}{dl} = \frac{12 \cdot \mu_{Li} \cdot q''_{eff} \cdot x}{x \cdot w^3 \cdot \rho_{Li} \cdot H_{Li}} \cdot r_v \cdot (1 + \cos\alpha) \quad . \tag{3.2.10}$$

Integrated over $l = r_v \cdot \alpha$, we get

$$\Delta p_{H2}(\alpha) = \frac{C_1}{w^3} \cdot \left(\alpha + \sin\alpha\right) \tag{3.2.11}$$

where

$$C_1 = \frac{12 \cdot \mu_{Li} \cdot q''_{eff} \cdot r_v^2}{\rho_{Li} \cdot H_{Li}} \quad . \tag{3.2.12}$$

Pressure Drop of the Liquid in the Capillary. The pressure drop in a capillary with the radius *a* and with an effective length l_{eff} and a velocity v_{cap} is given by [1],

$$\Delta p_{H3} = \frac{8 \cdot \mu_{Li} \cdot v_{cap} \cdot l_{eff}}{a^2} \quad . \tag{3.2.13}$$

The velocity v_{cap} is calculated from the *α*-dependent mass flow rate $\dot{m}(\alpha)$ needed to remove the heat from the first wall at an angle α by evaporation:

$$v_{cap}(\alpha) = \frac{\dot{m}_{FW}(\alpha)}{\beta_c \cdot \rho_{Li} \cdot r_v \cdot d\alpha \cdot x}$$

with

$$\dot{m}_{FW}(\alpha) = \frac{q''_{eff} \cdot \sin\alpha \cdot r_v \cdot d\alpha \cdot x}{H_{Li}}$$

we get

$$v_{cap}(\alpha) = \frac{q''_{eff} \cdot \sin\alpha}{\beta_c \cdot \rho_{Li} \cdot H_{Li}} \tag{3.2.14}$$

where β is the area fraction of the capillaries in the capillary structure (screen). $v_{cap}(\alpha)$ can be replaced in Eq. (3.2.13), and with $a = d_c/2$, we get

$$\Delta p_{H3} = \frac{32 \cdot \mu_{Li} \cdot q''_{eff} \cdot \sin\alpha \cdot l_{eff}}{d_C^2 \cdot \beta_c \cdot \rho_{Li} \cdot H_{Li}} \quad . \tag{3.2.15}$$

As an approximation the effective length of the liquid in the capillary l_{eff} is chosen as

$$l_{eff} = t_c - r_{miniscus}$$

where $r_{miniscus} \cong a$, the radius of the capillary.

MHD Pressure Drop in the Deeding Gap Due to Poloidal Magnetic Field. The Hartmann number M can be defined as:

$$M = B \cdot l_{char} \cdot \sqrt{\frac{\sigma e_{LI}}{\mu_{Li}}} \tag{3.2.16}$$

where B is the magnetic field component perpendicular to the flow direction, l_{char}, is a characteristic length, in this case the half width of the feeding gap. σe_{Li} and μ_{Li} are the electrical conductivity and the dynamic viscosity, respectively. When M is large compared with unity then the pressure gradient dp/dl in the lithium under the field component $B(\alpha)$ of the poloidal field, which is perpendicular to the flow direction can be expressed by:

$$\frac{dp}{dl} = \frac{\overline{Cw}}{1+\overline{Cw}} \cdot \sigma e_{Li} \cdot v(\alpha) \cdot \left(B_p \cdot \cos\alpha\right)^2 \quad . \tag{3.2.17}$$

Introducing $v(\alpha)$ from Eq. (3.2.8) and replacing dl by $r_v \cdot \alpha$ we get after some rearrangements

$$\frac{dp}{dl} = \frac{\overline{Cw}}{1+\overline{Cw}} \cdot \frac{\sigma e_{Li} \cdot q''_{eff} \cdot B_p^2 \cdot r_v^2}{w \cdot \rho_{Li} \cdot H_{Li}} \cdot (1+\cos\alpha) \cdot \cos^2\alpha \tag{3.2.18}$$

where $\overline{Cw}$ is the averaged wall conduction ratio of the Hartmann walls of the feeding gap (channel) defined as:

$$\overline{Cw} = \frac{1}{\sigma e_{Li} \cdot 0.5 \cdot w} \cdot \frac{\left\{\sigma e_W \cdot t_{FW} + \left[\beta_c \cdot \sigma e_{Li} + (1-\beta_c) \cdot \sigma e_W\right] \cdot t_C\right\}}{2} \quad . \tag{3.2.19}$$

For this case the Hartmann walls are the first wall with thickness t_{FW} and the capillary structure (screen) with thickness t_C.

We define the constants:

$$C2 = \frac{\overline{Cw}}{1+\overline{Cw}} \tag{3.2.20}$$

with $\overline{Cw}$ from Eq. (3.2.19) and

$$C3 = \frac{\sigma e_{Li} \cdot q''_{eff} \cdot B_p^2 \cdot r_v^2}{\rho_{Li} \cdot H_{Li}} \tag{3.2.21}$$

and integrating dp in Eq. (3.2.18) over α and keeping in mind that $\mathrm{dl} = r_v \cdot d\alpha$, we get the α-dependent MHD-pressure drop in the feeding gap caused by the poloidal field component as

$$\Delta p_{M1}(\alpha) = C2 \cdot C3 \cdot \frac{1}{w} \cdot \left\{ \frac{1}{2} \cdot \alpha + \frac{1}{4} \cdot \sin 2\alpha + \frac{1}{12} \cdot \sin 3\alpha + \frac{3}{4} \cdot \sin\alpha \right\} \quad . \tag{3.2.22}$$

MHD Pressure Drop in the Feeding Gap Due to Toroidal Magnetic Field. Under the same restrictions for the size of the Hartmann number as before a similar correlation for the pressure gradient caused in this case by the toroidal magnetic field component holds:

$$\frac{dp}{dl} = \frac{Cw_t}{1 + Cw_t} \cdot \sigma e_{Li} \cdot v(\alpha) \cdot B_t^2 \quad . \tag{3.2.23}$$

The wall conduction ratio Cw_t can be expressed in the form:

$$Cw_t = \frac{\sigma e_W \cdot 0.5 \cdot t_{W,t}}{\sigma e_{Li} \cdot 0.5 \cdot b_t} \tag{3.2.24}$$

where $t_{W,}$ is the effective thickness of the circumferential spacers (Fig. 3.2-3) and with b_t representing the toroidal direction.

If we insert $v(\alpha)$ from Eq. (3.2.8) into (3.2.23) and integrate over α we get the α-dependent pressure drop caused by the toroidal magnetic field component,

$$\Delta p_{M2}(\alpha) = C4 \cdot C5 \cdot \frac{1}{w} \cdot \left(\alpha + \sin\alpha \right) \tag{3.2.25}$$

where $C4 = \dfrac{Cw_t}{1 + Cw_t}$ (3.2.26)

and $C5 = \dfrac{\sigma e_{Li} \cdot q_0'' \cdot B_t^2 \cdot r_v^2}{\rho_{Li} \cdot H_{Li}}$. (3.2.27)

MHD Pressure Drop in the Capillary Due to Toroidal Magnetic Field.

$$\Delta p_{M3} = \frac{Cw_{cap}}{1 + Cw_{cap}} \cdot \sigma e_{Li} \cdot v_{cap}(\alpha) \cdot B_t^2 \cdot l_{eff} \tag{3.2.28}$$

$$Cw_{cap} = \frac{\sigma e_W \cdot t_{cap}}{\sigma e_{Li} \cdot a} \tag{3.2.29}$$

where tcap = $(1/2) \cdot d_c \cdot (1 - \beta_c)$ and $a = 0.5 \cdot d_c$ substituting the velocity $v_{cap}(\alpha)$ from Eq. (3.2.14) into (3.2.28) yields:

$$\Delta p_{M3} = C6 \cdot C7 \cdot \sin(\alpha) \tag{3.2.30}$$

where $C6 = \frac{Cw_{cap}}{1+Cw_{cap}}$ (3.2.31)

and $C7 = \frac{q''_{eff} \cdot \sigma e_{Li} \cdot B_t^2 \cdot l_{eff}}{\beta_c \cdot \rho_{Li} \cdot H_{Li}}$. (3.2.32)

The thickness of the effective Hartmann wall of the capillary t_{cap} is chosen $t_{cap} = r_c$ the radius of the capillary and the effective length of the capillary channel $l_{eff} = t_c$ the thickness of the screen.

The Pressure Jump Through the Evaporation Surface. A liquid surface is at equilibrium saturation condition when the momentum of the leaving and entering molecules is at balance. If more molecules are leaving the surface than entering (evaporation) a net momentum is exerted resulting in a pressure jump through the evaporation surface. The pressure jump caused by the nonequilibrium of the momentum can be expressed by [1]

$$\Delta p_{LV} = \frac{q''_{cap}(\alpha)}{H_{Li} \cdot \sqrt{\frac{M}{2 \cdot \pi \cdot R \cdot T_s}}} \tag{3.2.33}$$

where the heat flux within the capillary is given by

$$q''_{cap}(\alpha) = \frac{q''_{eff} \cdot \sin\alpha}{\beta_c}$$

and with $M = 6.94$ kg/kmole, molecular weight of lithium,
$R = 8314.4$ J/kmole-K, gas constant ,
$T_s = 1473$ K, saturation temperature,
$H_{Li} = 19.757\times10^6$ J/kg, heat of vaporization.

3.2.2. The Superheating of the Lithium at the Wall

Due to the pumping needed to feed the liquid lithium from the sump to the evaporation surface the pressure in the feeding gap is lower than at the evaporation surface where the saturation pressure corresponding to the saturation conditions exist. Therefore the superheating temperature at the first wall has to be related to this effective (“true”) saturation temperature $T_{s,true}$. In order to calculate the superheating of the lithium this means the temperature above the existent saturation conditions (true superheat) within the feeding gap we need the saturation pressure within the gap and the corresponding (fictitious) saturation temperature.

The saturation pressure within the gap is given by

$$p_N = p_S(T) - \Delta p_{tot} \tag{3.2.34}$$

where p_S is the saturation pressure of the system corresponding to the “true”saturation temperature of the lithium at the wall.

With the knowledge of p_N we can calculate the true saturation temperature, which can be obtained with vapor pressure as a function of temperature given by [2]

$$T_{s,true} = 1331.76101 + 399.7712 \cdot P_N \cdot 10^{-5} \quad . \tag{3.2.35}$$

The temperature difference ΔT_{LiG} over the capillary structure and the feeding gap can be written as

$$\Delta T_{LiG} = \Delta T_{FG} + \Delta T_{CA} \tag{3.2.36}$$

where $\Delta T_{FG} = q''_{eff} \cdot w / \lambda_{Li}$, the temperature difference over the feeding gap and

$$\Delta T_{CA} = q''_{eff} \cdot \left[\frac{\beta_c \cdot l_{effCA}}{\lambda_{Li}} + \frac{(1-\beta_c) \cdot t_c}{\lambda_W} \right] \tag{3.2.37}$$

the temperature difference over the capillary structure.

The above equation is based on the model in which saturation temperature is assumed at both free surfaces of lithium and of tungsten. With the knowledge of ΔT_{LiG} we can define an effective width w_{eff} of the lithium-feeding gap, given as

$$w_{eff} = w + \beta_c \cdot l_{effCA} + \frac{\lambda_{Li}}{\lambda_W} \cdot (1-\beta_c) \cdot t_c \quad . \tag{3.2.38}$$

The lithium temperature at the wall equals to $T_{wl} = T_s + \Delta T_{LiG}$. The true superheating of the lithium at the wall can now be determined as

$$\Delta T_{SH,true} = T_{wl} - T_{s,true} \, . \tag{3.2.39}$$

The Maximum Allowed Superheating Temperature at a Wall of a Roughness δ. The superheat of a heated liquid is a subject described in many text books, e.g. J.M. Delhaye [3]. Especially the superheating of liquid sodium at a heated wall, *heterogeneous nucleation*, was one of the main issues within the frame of the Liquid Metal Fast Breeder Reactor (LMFBR) research leading to many investigations and publications compiled in H.M. Kottowski-Duemenil, (editor, 1975) [4]. Superheat of sodium up to 200°C is reported but it is also shown that it is very difficult to reproduce these high values.

In detail, the incipient boiling superheat is affected by many parameters, for example:

- Gas content of the liquid metal
- Gas trapped in the pockets of the wall cavities (roughness)
- Oxide impurity of the liquid metal
- Pressure-temperature history
- Heating surface condition
- Velocity of the liquid metal
- Nuclear radiation
- Heat flux.

Taking into account, especially the influence of trapped gas in the pockets of the rough surface one has to be cautious to transfer these results to high temperature lithium boiling because the main aim of the past research was to show the opposite of what we want to have. Therefore the main question was how fast the roughness of the heated surface is activated by the gas dissolved in the liquid metal and how high is the superheat. In our case we would be dealing with condition after an extended out gassing procedure and after long period of high temperature evaporation. The probability of gas filled pockets acting as nucleation sites will be very low However, no reliable data on the superheat of lithium under such conditions could be found in the literature.

Therefore the following equation proposed by Dunn [1] should be considered as a conservative estimate. In this equation the maximum superheating $\Delta T_{Superheat}$ of a liquid contacting a heated wall with roughness $t_{roughness}$ is given by

$$\Delta T_{Superheat} = \frac{3.06 \cdot \sigma s_{Li} \cdot T_s}{\rho_{v,Li} \cdot H_{Li} \cdot \delta} \tag{3.2.40}$$

where δ is the standard depth of a rough surface, and $\delta = t_{roughness}$. For a rather smooth surface with a roughness $t_{roughness} = 25\times10^{-6}$ m and using $T_S = 1473$ K we get a superheat of $\Delta T_{Superheat} =$ 104 K.

The results for the critical surface heat load of heat pipes found in the literature [1,5] can not be used for drawing conclusion on the superheat involved because in these cases the critical heat flux was not dominated as in our case by the width of the feeding layer.

In publications from Dalle Donne [6,7], it is shown that with normal smooth stainless steel surfaces in presence of liquid metals, the biggest surface cavities were still active, i.e. still full with vapour or gas after a long time in contact with the liquid and were not displaced by the liquid. The cavity has a maximum radius of about 0.25µ. For our case with smooth tungsten surface and long time high temperature operation, similar behaviour could be expected.

Using the method developed by Dalle Donne [6], Figure 3.2-4 shows the superheating of a heated wall as a function of cavity radius. As an example, for a cavity radius of the rough surface of 1µ and at a saturation temperature of $T_s = 1500$ we get a superheat temperature of 350 K, corresponding to a wall surface temperature of 1850 K.

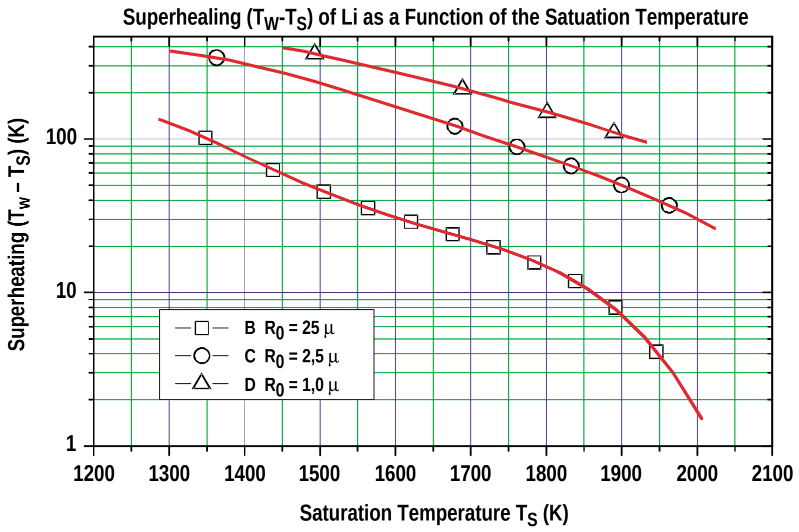

Figure 3.2-4. The superheat temperature of lithium (T_w - T_s) at a heated wall as a function of the saturation temperature T_s and cavity radius R_o.

3.2.3 Pressure Drop of the Vapor Along the First Wall Cooling Tube

For turbulent vapor flow in a tube the pressure drop over the length *x* can be calculated using the Fanning equation [1]:

$$\Delta p_{vapor} = \frac{4}{d_{hydr}} \cdot f \cdot \frac{1}{2} \cdot \rho_v \cdot \bar{v}_v^2(x) \cdot x \tag{3.2.41}$$

where $d_{hydr} = \frac{4 \cdot A}{Ci}$ the hydraulic diameter,

with $A = \frac{1}{2} \cdot r_v^2 \cdot \pi$ the area of the channel,

and $Ci = r_v \cdot \pi + 2 \cdot r_v$ the circumference of the channel, (3.2.42)

$$d_{hydr} = \frac{2 \cdot \pi \cdot r_v}{2 + \pi}$$

$f = \frac{0.0791}{Re^{1/4}}$ the friction factor $2100 < Re < 10^5$.

The velocity $\bar{v}_v(x)$ as a function of the toroidal position *x* can be written:

$$\bar{v}_v(x) = \frac{\dot{m}_v(x)}{\rho_v \cdot A}$$

with $\dot{m}_v(x) = \frac{d\dot{m}_v(x)}{dx} \cdot x \quad \text{if} \quad q''_{eff} \neq f(x)$

$$\frac{d\dot{m}_v(x)}{dx} = \frac{q''_{eff}(x) \cdot 2 \cdot r_v}{H_{Li}} = \text{const. and} \tag{3.2.43}$$

therefore $\dot{m}_v(x) = \frac{q''_{eff} \cdot 2 \cdot r_v \cdot x}{H_{Li}}$

we get $\bar{v}_v(x) = \frac{q''_{eff} \cdot 2 \cdot r_v \cdot x}{H_{Li} \cdot \rho_{v,Li} \cdot \frac{1}{2} \cdot r_v^2 \cdot \pi} = \frac{4 \cdot q''_{eff} \cdot x}{H_{Li} \cdot \rho_{v,Li} \cdot r_v \cdot \pi} \quad \text{(m/s)}$.

Using $\bar{v}_v(x)$ from Eq. (3.2.43) the x-dependent Reynolds-number Re(x*)* can be defined as

$$\text{Re}(x) = \frac{\rho_v \cdot v_v(x) \cdot d_{hydr}}{\mu_v}$$

can be written in the form

$$\text{Re}(x) = \frac{8 \cdot q''_{eff} \cdot x}{\mu_{v,Li} \cdot H_{Li} \cdot (2 + \pi)} \quad .$$

3.2.4 Results of the First Wall Toroidal Channel Modeling

The calculations are done using the MATHCAD 2000 [8] software and the material data are compiled in Appendix 3.A.1. The complete MathCad-program for the toroidal FW-channel concept with a list of all relevant parameters is given in Appendix 3.A.2.

The main parameters used for the calculations are given in Table 3.2-1.

Figure 3.2-5 shows the dependence of the capillary pressure head from the capillary diameter d_c and the total pressure drop of the liquid lithium needed to remove a heat flux of q_0 = 2.0 MW/m^2 from the first wall for the chosen parameters independence of the gap width w and the capillary diameter d_c respectively.

The contributions of the different pressure drops are taken for an angle α where the total pressure drop Δp_{total} has its maximum value. The calculations of the MHD pressure drop are conducted neglecting three-dimensional effects, which may happen due to the changing magnetic field and/or mass flow through within the feeding gap along the flow direction.

Table 3.2-1. The Main Parameters Used for the Calculations

Parameters common for toroidal and poloidal first wall channels:

Surface heat flux, MW/m^2	$q_0'' = 2$
Toroidal magnetic field strength, Tesla	$B_T = 6.0$
Wall thickness, m	$t_w = 3.0\times10$
Thickness of the capillary structure, m	$t_c = 0.5\times10^{-3}$
Area fraction of the capillaries	$\Delta_c = 0.5$
Thickness of the porous tungsten sheet, m	$t_{WB} = 2.0\times10^{-3}$
Porosity of the tungsten sheet	$\varepsilon_{Sh} = 0.5$

Toroidal first wall channels:

Outer tube radius, m	$r_a = 0.05$
Tube length, m	$l_{ax} = 3.00$
Toroidal distance of the spacers, m	$b_t = 0.04$
Effective thickness of the spacers, m	$t_{WT} = 0.5\times10^{-3}$

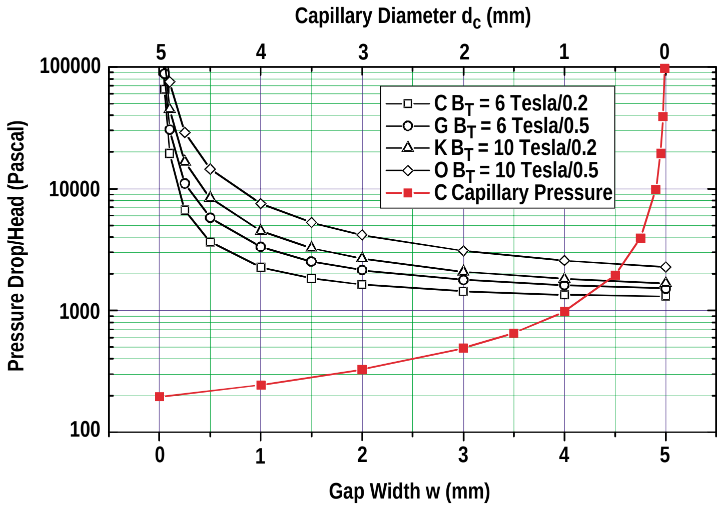

Figure 3.2-5. Capillary pressure head and the total pressure drop in dependence of the capillary diameter d_c and of the first wall feeding gap width w respectively, for toroidal field components B_T = 6 and 10 T and for toroidal spacer thickness 0.2 and 0.5 mm.

From Figure 3.5 we can derive the minimal gap width w for a chosen capillary diameter d_c needed in order to satisfy the pressure balance. The effect of a misalignment of the toroidal FW channel with respect to the direction of the magnetic field can be assessed using Figure 3.6, which shows the influence of the poloidal to toroidal magnetic field ratio on the capillary diameter needed to supply the lithium to the first wall. As shown the maximum allowed superheating temperature is reached at a B_p to B_T ratio of 0.4 due to the high pumping pressure needed. If the total pressure drop due to a high magnetic field strength becomes high corresponding to a small capillary diameter for the needed increased pumping the true saturation pressure, correspondingly the true saturation temperature $T_{s,true}$ decreases and the superheating temperature $\Delta T_{s,true}$ increases. The dashed line in Figure 3.6 represents the assumed limiting value of 100 K superheating. Below this line higher superheating results.

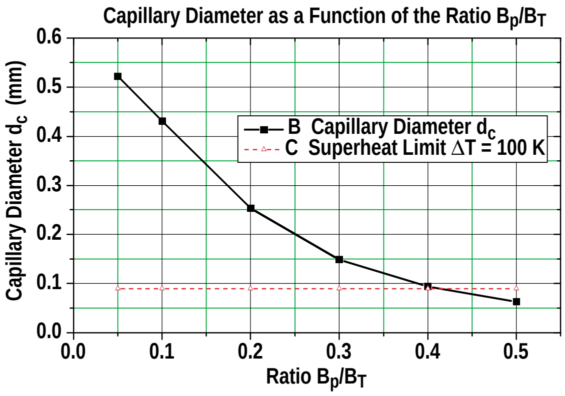

Figure 3.2-6. The dependence of the capillary diameter from the B_p/B_T-ratio for B_T = 6 Tesla, a feeding gap width of w = 1 mm and an effective thickness of the spacers of 0.2 mm.

The main results for the selected set of parameters of the toroidal first wall channel are given in Table 3.2-2.

Table 3.2-2. Key results of the Toroidal First Wall Channel Transpiration Cooling

Denomination		Value
The FW feeding gap width, mm	w	1.0
Effective heat flux at the FW, W/m^2	q''_{eff}	2.5×10^6
Total pressure drop, Pa	Δp_{tot}	2.271×10^3
Capillary diameter needed, mm	dcN1	0.43
Temperature increase over the gap, K	ΔT_{LiG}	52.6
Temperature at the inner side of the FW (K)	T_{wl}	1526
Maximum temperature at the outside of the FW, K	T_{MAXW}	1614
Theoretical limit of superheat, K	$\Delta T_{Superheat}$	103
The *true* superheat, K	ΔT_{SHtrue}	65.9
Vapor mass flow rate at the outlet of the tube, kg/s	$\dot{m}_{FW}(z_0)$	0.035
Vapor velocity at the outlet, m/s*	v_{vo}	241
Pressure loss along the tube, Pa	Δp_{vapor}	179
The integrated FW channel mass flow rate, kg/s	$\dot{m}_{int,FWCh}$	2.837
Needed manifold diameter, m**	D_{Mani}	0.68

*The reduction of the vapor area by the feeding tube (FT) not considered.
**For a limited vapor velocity of 400 m/s.

3.2.5 The Feeding of Liquid Lithium to the Toroidal First Wall Channels

Figure 3.2-7 shows the schematic of the feeding tube with the toroidal field aligned parallel to the tube. The arrangement of the lithium feeding and tap concentric tubes is also shown. The lithium in the feeding tube with a velocity $v_{FT}(z)$ as a function of z is heated up by volumetrically heating, heat deposited within the tungsten tube wall and by the condensation of the lithium vapor. The feeding tube toroidal length is selected to be 3 m in this calculation.

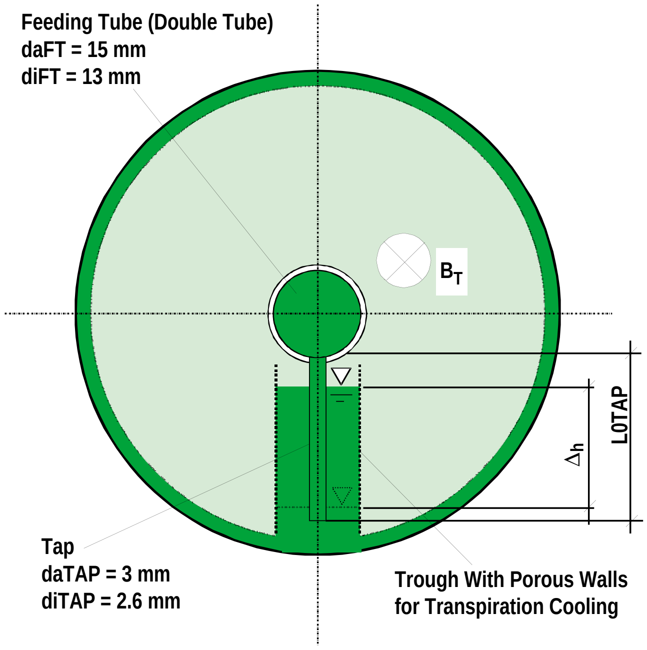

Figure 3.2-7. Sketch of the MHD controlled lithium level in the trough (Sump).

First scooping calculation shows that a double tube concept with a thermal and an electrical insulation as shown in Figure 3.2-7 is needed to avoid that the heat input and the MHD pressure drop reaching prohibitively high values.

Combining the equations for the energy and the mass balance gives the following equations

$$\dot{m}' \cdot dz = \dot{m}_{FT}(z) \cdot Cp_{Li} \cdot dT \tag{3.2.44}$$

$$\dot{m}_{FT}(z) = \dot{m}_{FT0} - \dot{m}'_{FW}(z) \cdot z \tag{3.2.45}$$

where

$$\dot{m}' = q'''_{LiR0} \cdot A_I + q'''_{WR0} \cdot A_{tuwa} + \overline{q''_{cond}} \cdot d_{iFT} \cdot \pi \tag{3.2.46}$$

and

$$m'_{FW}(z) = \frac{q''_{eff} \cdot 2 \cdot r_V}{H_{Li}}$$

q''_{eff} = 2.5×10^6 W/m^2, effective heat flux at the first wall (Eq. 3.2.2),
q'''_{LiR0} = 37×10^6 W/m^3, volumetric heat source in Li at the first wall,
q'''_{WR0} = 100×10^6 W/m^3, volumetric heat source in tungsten at the first wall,
q''_{Cond} W/m^2, mean heat flux due to condensing Li-vapor,
A_I m^2, inner area of the feeding tube,
A_{tuwa} m^2, area of the tube wall.

We get the differential equation

$$dT = \frac{B}{A - z} \cdot dz \tag{3.2.47}$$

where $A = \frac{\dot{m}_{FT0} \cdot H_{Li}}{q''_{eff} \cdot 2 \cdot r_V}$

with $\dot{m}_{FTO} \neq f(z)$

$$B = \frac{q' \cdot H_{Li}}{Cp_{Li} \cdot q''_{eff} \cdot 2 \cdot r_V} \quad . \tag{3.2.48}$$

After integration and some re-arrangement we get finally the equation to calculate the mass flow rate at the inlet, which would fulfil the temperature requirement of the lithium at the outlet of the tube to be kept below the saturation temperature within the tube:

$$\dot{m}_{FT0} = \frac{A \cdot q''_{eff} \cdot 2 \cdot r_V}{H_{Li}} \tag{3.2.48}$$

where

$$A = \frac{L_{AZ}}{1 - e^{\left(T_{out} - T_0\right)/B}}$$

with $T_{out} \leq T_{sat}$.

The condensation heat flux on the feeding tube is calculated under the assumption that the heat transfer of the condensation process is dominated by the heat transport through the film of condensed lithium at the surface of the tube and through the tube wall. Due to the complex conditions to which this film is subjected it is very difficult to calculate its thickness. Therefore we use the thickness of the film also as a parameter within a small window (from 0.5 to 2.0 mm).

$$q''_{Cond}(z) = \frac{T_{sat} - T_{Li}(z)}{\frac{t_{FT}}{l_W} + \frac{w_{Film}}{l_{Li}}} \tag{3.2.49}$$

where $T_{Li}(z)$ is the z-dependent temperature of the lithium within the feeding tube,
t_{FT} is the wall thickness of the feeding tube,
w_{Film} is the lithium film thickness,
λ is the corresponding thermal conductivity.

In order to determine the condensation heat flux on the feeding tube (FT) a linear temperature increase along the tube is assumed. This allows the use of a mean value of the condensation heat flux.

$$\overline{q''_{\text{Cond}}} = \frac{1}{2} \cdot \left[q''_{\text{Cond}}(z1) + q''_{\text{Cond}}(z0) \right] \tag{3.2.50}$$

where z1= LAZ, the toroidal length of the FT,
z0 = 0.

3.2.5.1 Design calculations of the active pumped feeding tube (FT)

In order to reduce the heat flux due to condensation of the lithium vapor on the feeding tube a double tube is used with an evacuated 1 to 2 mm gap in between. To simplify the heat transfer calculations the temperature at the outside of the outer tube is assumed to be at saturation condition, which is a conservative approach.

Chosen parameters:
do_{FTi} = 15×10^{-3} m, outer diameter of the inner feeding tube;
t_{FTi} = 1.0×10^{-3} m, wall thickness of the inner feeding tube;
di_{Fti} = do_{FTi}- $2 \times t_{\text{Fti}}$;
di_{Fti} = 0.013 m, inner $_{\text{diameter}}$ of the inner feeding tube;
w_{ins} = 1.0×10^{-3} m, width of the insulation gap;
t_{FTo} = 1.0×10^{-3} m, wall thickness of the outer feeding tube;
do_{FTo} = 19×10^{-3} m, outer diameter of the outer feeding tube;
ε_1 = 0.5 /, emissivity of the outer feeding tube;
ε_2 = ε_1 /, emissivity of the inner feeding tube;
CS = 5.67×10^{-8} $\text{W} \cdot \text{m}^{-2} \cdot \text{K}^{-4}$, black body radiation constant;
da_{tap} = 3.0×10^{-3} m, outer diameter of the tap;
t_{tap} = 0.2×10^{-3} m, wall thickness of the tap;
di_{tap} = $da_{\text{tap}} - 2 \times t_{\text{tap}}$ m, inner diameter of the tap;
Sp_{tap} = 0.1 m, spacing of taps;
N_{tap} = $L_{\text{AZ}}/Sp_{\text{tap}}$, number of taps over the toroidal width LAZ.

The temperature difference across the outer tube wall is given by

$$\Delta T_{\text{FTo}} = \frac{1}{2} \cdot q'''_{\text{WR0}} \cdot \frac{t_{\text{FTo}}^2}{\lambda_{\text{W}}} \tag{3.2.51}$$

$$\Delta T_{\text{FTo}} = 0.588$$

$T1_i$ = $T_s + \Delta T_{\text{FTo}}$ K, temperature at the inner side of the outer tube;
$T2_o(z)$ = $T_{\text{Li}}(z)$ K, temperature at the outer side of the inner tube;
z1 = L_{AZ} = 3.0 m;
T_s = 1.473×10^3 K;
ΔT_0 = 500 K, chosen subcooling of the lithium at the inlet;
T_{out} = $T_s - \Delta T_0$ K;
T_{out} = 973 K.

$$AI_i = \left(\frac{do_{FTi} - 2 \cdot t_{FTi}}{2} \right)^2 \cdot \pi$$

$$AA_i = \left(\frac{do_{FTi}}{2} \right)^2 \cdot \pi \qquad .$$

$$A_{tuwa} = AA_i - AI_i = 4.398 \cdot 10^{-5} \quad \left(m^2 \right)$$

3.2.5.2 The heat flux on the feeding tube due to condensation of lthium vapor

The liquid film formed by the condensed vapor dominates the heat transfer of condensing vapor. We assume as a conservative approximation the film thickness to be zero so the surface temperature will be at saturation temperature T_s.

This means: $w_{Film} = 0 \;\rightarrow\; T_{oFTo} = T_s$.

In this case the condensation heat flux is given by the driving temperature difference between the surface of the outer tube and the inner surface of the inner tube $\Delta T = T_{oFTo} - T_{iFTi}$ and the heat transfer between the outer and the inner tube, where now $T_{oFTo} = T_s$.

For the calculations of the condensation heat flux on the inner feeding tube a linear increase of the lithium temperature along the feeding tube from T_0 to T_{out} is assumed, where T_{out} is limited to $\leq T_s$.

$$T_{Li}(z) = T_0 + \frac{T_{out} - T_0}{L_{AZ}} \cdot \left(z - z0 \right) \quad . \tag{3.2.52}$$

3.2.5.3 The heat transfer from the outer to the inner tube

In the case of an evacuated insulation gap the heat transfer from the outer to the inner tube is governed by radiation heat transfer.

$$q''_{rad}(z) = CR12 \cdot \left(T1_i^4 - T2_o^4 \right) \tag{3.2.52}$$

$$q''_{rad}(z) = CR12 \cdot \left(T1_i^4 - T2_o^4 \right)$$

$$CR12 \;\; = \frac{CS}{\frac{1}{\varepsilon_1} + \frac{1}{\varepsilon_2} - 1} \qquad CR12 = 1.89 \cdot 10^{-8}$$

$$\overline{q''_{rad}} \;\; = \frac{1}{L_{AZ}} \cdot \int_{z0}^{LAZ} q''_{rad}(z) \cdot dz \;\; = \;\; 4.33 \cdot 10^4 \quad \left(W/m^2 \right)$$

$$q'_{FT} \;\; = q'''_{LiR0} \cdot AI_i + q'''_{WR0} \cdot A_{tuwa} + \overline{q''_{rad}} \cdot d_{oFTi} \cdot \pi$$

where

$$q'''_{LiR0} = 3.7 \cdot 10^7 \left(W/m^3\right) \quad \text{and} \quad q'''_{WR0} = 1 \cdot 10^8 \left(W/m^3\right)$$

$$q'_{FT} = 1.134 \cdot 10^4 \ (W/m) \quad .$$

Assuming a homogeneous feeding rate $\dot{m}'_{FT}(z) = \dot{m}'_{FW}(z)\,(kg/m \cdot s)$ along the azimuthal length of the feeding tube a correlation for the azimuthal temperature gradient dT/dz of the lithium in the feeding tube can be derived,

$$\frac{dT}{dz} = B \cdot \frac{1}{A - z} \quad . \tag{3.2.53}$$

The integration of dT over the azimuthal length, LAZ, provides an equation for the unknown value A,

$$A = \frac{LAZ}{1 - e^{-\left(T_s - T_{out}/B\right)}} = 3.379$$

where B is defined

$$B = \frac{q'_{FT} \cdot H_{Li}}{Cp_{Li} \cdot q''_{eff} \cdot 2 \cdot r_V} = 228.457 \quad .$$

With the knowledge of A the mass flow rate $\dot{m}'_{FT0}$ can now be determined:

$$\dot{m}_{FT0} = \frac{A \cdot q''_{eff} \cdot 2 \cdot r_V}{H_{Li}} \quad . \tag{3.2.54}$$

$\dot{m}_{FT0} = 0.04$ kg/s, mass flow rate at the entrance of the feeding tube;
$\dot{m}_{FW}\left(L_{AZ}\right) = 0.035$ kg/s, mass flow rate of Li evaporated at the FW;
$\Delta\dot{m}_{FT} = \dot{m}_{FT0} - \dot{m}_{FW}(L_{AZ}) = 4.476 \cdot 10^{-3}\,(kg/s)$;

$$\dot{m}_{FT}(z) = \dot{m}_{FT0} - \frac{q''_{eff} \cdot 2 \cdot r_V}{H_{Li}} \cdot z \quad .$$

With the knowledge of the z-dependent mass flow rate $\dot{m}_{FT}(z)$ within the feeding tube the z-dependent flow velocity can be determined which is needed for the pressure drop calculation.

$$v_{FT}(z) = \frac{\dot{m}_{FT}(z)}{r_{Li} \cdot AI_i} \quad . \tag{3.2.55}$$

$$v_{FT}(z0) \equiv v_{FT0} = 0.727 \text{ m/s}.$$

3.2.5.4 Results of the Pressure Drop Calculations

The Hydraulic Pressure Drop. The Reynolds number of the lithium flow in the feeding tube is given by

$$\mathrm{Re}_{LiFT}(z) = \frac{v_{FT}(z) \cdot d_{hydrFT}}{\upsilon_{Li}} \tag{3.2.56}$$

where $d_{hydrFT} = d_{iFTi} = 0.013\,\mathrm{m}$, and $\upsilon_{Li} = \frac{m_{Li}}{r_{Li}} = 4.375 \cdot 10^{-7}\ \mathrm{m^2/s}$.

If the Reynolds number >2100 the flow start to get turbulent and the following pressure drop correlation can be applied:

$$FF(z) = \frac{0.0791}{\mathrm{Re}_{LiFT}(z)^{1/4}} \quad \text{friction factor of turbulent liquid flow} \tag{3.2.57}$$

$$\Delta p_{HFT} = \int_{z0}^{z1} \frac{4}{d_{hydrFT}} \cdot FV(z) \cdot \frac{1}{2} \cdot \rho_{Li} \cdot v_{FT}(z)^2 \cdot dz \tag{3.2.58}$$

$$\Delta p_{HFT} = 268.97\ (\mathrm{Pa}) \quad \text{this is the hydraulic pressure drop in the FT.}$$

3.2.5.5 The MHD pressure loss due to the poloidal field component

$$CW_{FT} = \frac{\sigma e_W \cdot t_{FTi}}{\sigma e_{Li} \cdot 0.5 \cdot d_{iFTi}} = 0.162$$

$$C1_{FT} = \frac{CW_{FT}}{1 + CW_{FT}} = 0.14$$

$$\Delta P_{MFT} = \int_{z0}^{z1} C1_{FT} \cdot \sigma e_{Li} \cdot B_p^2 \cdot v_{FT}(z) \cdot dz \tag{3.2.59}$$

with v_{FT0} + 0.727 m/s, $\sigma e_{Li} = 1.894 \cdot 10^6$ A/Vm, $B_p = 0.6$ Tesla, $L_{AZ} = 3.0$ m, we get for the MHD pressure drop in the feeding tube (FT):

$$\Delta P_{MFT} = 1.159 \cdot 10^5\ \mathrm{Pa} \quad .$$

3.2.5.6 The total pressure drop along the feeding tube

$$\Delta P_{FTtotal} = \Delta P_{HFT} + \Delta P_{MFT} = 1.159 \cdot 10^5\ \mathrm{Pa} \quad . \tag{3.2.60}$$

3.2.5.7 The flow control along the tube feeding the sump

In order to control the level of the liquid lithium sump along the first wall cooling channel we propose to take profit of the change of MHD pressure drop with changing sump height.

A sketch of this method and the corresponding MHD fundamentals are shown in Figure 3.2-7. But this method can only work if at least the pressure drop over the whole length of the feeding tube is less than the highest pressure drop in the taps.

The calculations of this pressure drop are conducted for two different conditions

1. With lithium vapor surrounding the tap and
2. With the tap fully immersed in liquid lithium.

Using the above listed parameters the following pressure drops were calculated.

3.2.5.8 The pressure drop in the taps

The hydraulic pressure losses are very small compared with the MHD losses; therefore they are omitted.

Case 1: Lithium vapor surrounding the tap

$$CW_{tap0} = \frac{t_{tap} \cdot \sigma e_{w}}{0.5 \cdot di_{tap} \cdot \sigma e_{Li}} = 0.162$$

$$C0_{tap} = \frac{CW_{tap0}}{1 + CW_{tap0}} = 0.14$$

$$A_{tap} = \left(\frac{di_{tap}}{2}\right)^{2} \cdot \pi = 5.309 \cdot 10^{-6}$$

$$v_{tap} = \frac{\dot{m}_{FW}(z1)}{N_{tap} \cdot A_{tap} \cdot \rho_{Li}} = 0.538 \text{ m/s} \qquad (3.2.61)$$

$$L0_{tap} = r_{v} - 0.5 \cdot do_{FTo} = 0.038 \text{ m}$$

$$\Delta P_{tapM0} = C0_{tap} \cdot v_{tap} \cdot \sigma e_{Li} \cdot B_{T}^{2} \cdot L0_{tap} = 1.921 \cdot 10^{5} \text{ Pa}.$$

Case 2: MHD pressure drop for the tap fully immersed in Lithium (Figure 3.2-7). In this case the "lithium wall" determines the wall conduction ratio CW_{tap} and for simplification we use a fictitious wall thickness of the tap $t_{tapf} = t_{Li}$.

$$L1_{tap} = L0_{tap}$$

$$t_{Li} = 5 \cdot d0_{tap} \quad \text{arbitrary chosen}$$

$$CW_{tap1} = \frac{t_{tapf} \cdot \sigma e_{Li}}{0.5 \cdot di_{tap} \cdot \sigma e_{Li}} = 11.538$$

$$C1_{tap} = \frac{CW_{tap1}}{1 + CW_{tap1}} = 0.92$$

$$\Delta P_{tapM1} = C1_{tap} \cdot v_{tap} \cdot \sigma e_{Li} \cdot B_T \cdot L1_{tap} = 1.265 \cdot 10^6 \text{ Pa} \quad . \tag{3.2.62}$$

Comparing the ten times higher pressure drop ΔP_{tapM1} of the fully immersed feeding tap with the total pressure drop $\Delta P_{FTtotal}$ along the feeding tube we can conclude that the principal of controlling the uniformity of feeding the lithium along the toroidal length of the blanket module is proven.

3.2 References

[1] P.D. Dunn and D. A. Reay, Heat Pipes, Pergamon, 4th edition, 1994

[2] N.B. Vargaftik, Tables on the Thermophysical Properties of Liquids and Gases, 2nd edition, Hemisphere Publishing Corp., 1975.

[3] J.M. Delhaye, M. Giot, M.L. Riethmueller, (editors), Thermohydraulics of Two-Phase Systems for Industrial Design and Nuclear Engineering,Hemisphere Publ. Company.

[4] H.M. Kottowski-Duemenil (editor), Liquid Metal Thermohydraulics, INFORUM-Verlag, 1977.

[5] V.A. Kirillin (Editor), Liquid-Metal Coolants for Heat Pipes and Power Plants, Hemisphere Publishing Corp., 1990.

[6] M. Dalle Donne, A New and Simple Method of Estimating the Liquid Superheat Due to Surface Conditions in Nucleate Boiling and its Application to Sodium, Nukleonik **8**. Band 3. Heft, 1966, s. 133–137.

[7] M. Dalle Donne and M.P. Ferranti, The Growth of Vapor Bubbles in Superheated Sodium, Int. J. Heat Mass Transfer. **18**, pp. 477– 493 (1975).

[8] MathCad, MathSoft, Inc.,101 Main Street, Massachusetts 02142, USA, http://www.mathsoft.com/

3.3 The Integrated Poloidal First Wall Cooling Channel Concept

In the poloidal first wall cooling channel concept the liquid lithium can no longer be supplied out of a sump at the bottom of the channel. Therefore pursuing this concept the idea of an integrated transpiration cooled concept came up. Figure 3.3-1 shows schematically the geometry of this concept including the routing of the liquid lithium from the tray to the first wall and of the vapor generated there and elsewhere in the system.

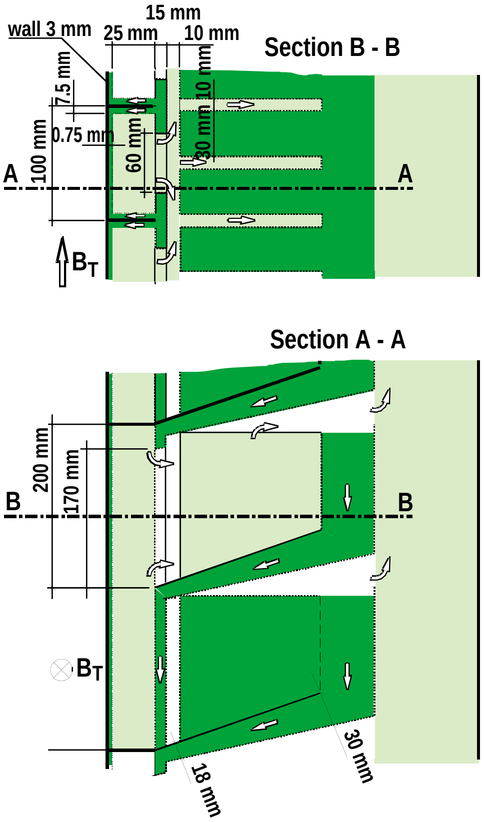

Figure 3.3-1. Transpiration cooled EVOLVE concept with poloidal first wall channels, all sketches out of scale.

Since this is a relatively new concept we will first explain the basic features and design principles.

3.3.1 Basic Features of the Transpiration Cooling

- Avoid any boiling, use only evaporation cooling through free porous surfaces.
- Take profit of the high superheat capability of volumetrically heated pure lithium (up to 200 K) in the breeding zone.
- Keep the MHD pressure losses of the liquid lithium in feeding channels by a proper design as low as possible.
- The thickness of the porous walls of breeding zone should be minimized.
- At any position in the system the applied pressure has to be kept below the break through pressure of the capillary surfaces.
- Optimise the width of the vapor channels with respect to pressure drop and void fraction.

3.3.2 Design Principals

- All liquid lithium feeding slots has to be cooled by evaporation cooling through porous walls.
- Depending on whether the slot is cooled only from one side or from both sides the width of the feeding slots has to fulfill the following condition:

$$w(R) = \sqrt{\frac{2 \cdot \Delta T_{max} \cdot \lambda_{Li}}{q'''(R)}} \quad \text{or} \quad w(R) = 2 \cdot \sqrt{\frac{2 \cdot \Delta T_{max} \cdot \lambda_{Li}}{q'''(R)}} \quad \text{respectively.}$$

- where: ΔT_{max} = the maximal temperature in the slab, $\Delta T_{max} \leq \Delta T_{superheat}$, λ_{Li} = the thermal conductivity of lithium, and $q'''(R)$ = the average volumetric power density.

  This principle is outlined schematically in Figure 3.3-2 where a volumetrically heated, lithium filled slot with the porous sidewalls is shown.
- Choose the surface capillary size corresponding to the pumping needs.
- The lithium filled porous walls has to be taken into account in calculating the thickness of the feeding gaps and the Li-slots using an averaged volumetric power density QVWE and an effective heat conductivity λ_{eff} of this walls.
- At any position in the system the applied pressure has to be kept below the break through pressure of the capillary surfaces.

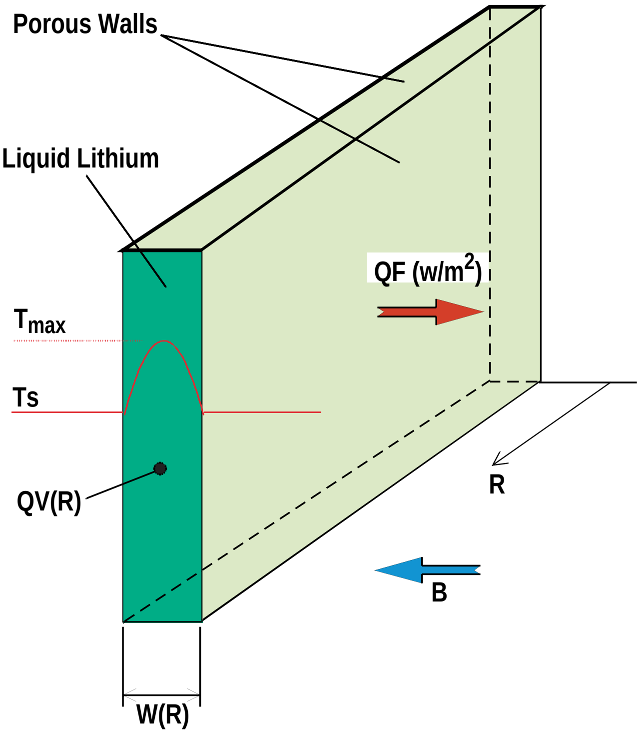

Figure 3.3-2. Principle sketch of a transpiration cooled, volumetrically heated lithium slab.

The main difference between the poloidal and the toroidal first wall channel is that for the poloidal oriented channel the first wall is flat and assumed to be strictly aligned with the toroidal magnetic field component. Therefore the flow of the lithium at the first wall can also be regarded as aligned with the toroidal field so that no MHD pressure drop by this field component is induced. Only the poloidal field component may cause MHD pressure losses. As a consequence the first wall feeding gap can be kept very thin which mitigates the problem of the superheating the lithium across the gap drastically. On the other hand the width of the radial gap feeding the front wall gap is almost not restricted by the temperature difference across the gap caused by the volumetrically heating of the lithium. Therefore the width of this gap has to be optimized only according to the restrictions of the MHD pressure drop induced by the toroidal magnetic field.

The total pressure drop of the first wall has to include the pressure drop of the first wall radial feeding gap. Since the radial feeding gap has to be cooled by transpiration cooling the mass flow rate in the gap will depend on the radial position R. The mass flow rate can be calculated,

$$\dot{m}_{FWRFG}(R) = \dot{m}(z1) + \left\{ q'''_{WE}(R) \cdot \frac{tw_{SW}}{2} + q'''_{Li}(R) \cdot wr0 \right\} \cdot \frac{SPH \cdot R}{H_{Li}} \qquad (3.2.63)$$

where

$$q'''_{WE}(R) = \left(1 - \beta_{Sh}\right) \cdot q'''_{W}(R) + \beta_{Sh} \cdot q'''_{Li}(R) \qquad (3.2.64)$$

the effective volumetric power density in the porous wall, with

β_{Sh}	the area fraction (in our case = volume fraction) of the capillaries of the porous wall,
tw_{SW}	the thickness of separation wall,
wr0	the chosen width of the radial feeding gap,
SPH	the poloidal spacing,

$q'''_{W}(R)$ and $q'''_{Li}(R)$ are defined above.

As a conservative assumption we use for $q'''_{W}(R)$ and for $q'''_{Li}(R)$ constant values at R = R0.

$$w(R) = 2 \cdot \sqrt{\frac{2 \cdot \Delta T_{max} \cdot \lambda_{Li}}{q'''(R)}}$$

where $\Delta T_{max} \leq \Delta T_{Superheat}$

$$QV \equiv q''' \text{ and } QF \equiv q'' \quad .$$

For the calculations the same basic equations as given in Section 3.3.2 are used. The main parameters for the Poloidal First Wall Channel are shown in Table 3.3-1. The complete MathCad-program for the poloidal FW-channel concept with a list of all relevant parameters is given in Appendix 3.A.3.

Table 3.3-1. Main Parameters for the Poloidal First Wall Channel

Radial width, m	SRW = 0.025
Toroidal width, m	STW = 0.100
Spacing of the poloidal separation walls, m	SPH = 0.200
Thickness of the poloidal separation walls, m	SPW = 2.0×10^{-3}
Thickness of the radial feeding gap, m	TRG = 7.5×10^{-3}

In Figure 3.3-3 the pressure drop integrated over the whole liquid and vapor routing is shown as a function of the feeding gap width w with the width of the radial FW channel gap width wr0 as a parameter. Additionally the capillary pressure head is shown in order to evaluate the pressure balance.

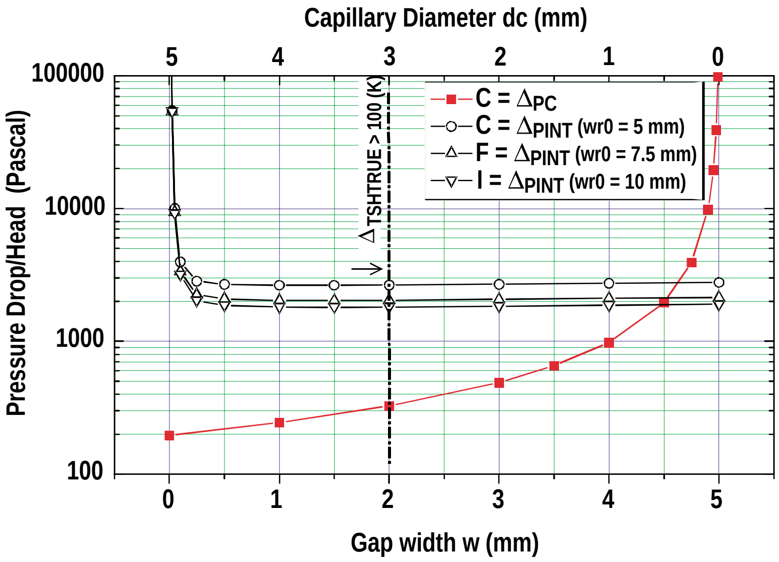

Figure 3.3-3. The integral pressure drop and the capillary pressure head independence of the first wall feeding gap width w and of the capillary diameter dc respectively, for a toroidal field component B_T = 6 T and for radial feeding gap thickness 5, 7.5, and 10 mm.

In Figure 3.3-4 the capillary diameter needed to pump the lithium to the first wall is shown as a function of the applied toroidal magnetic field for different true superheating temperatures. The figure shows once again that this concept exhibits higher margins with respect to superheating limits. The key results of the calculations are shown in Table 3.3-2.

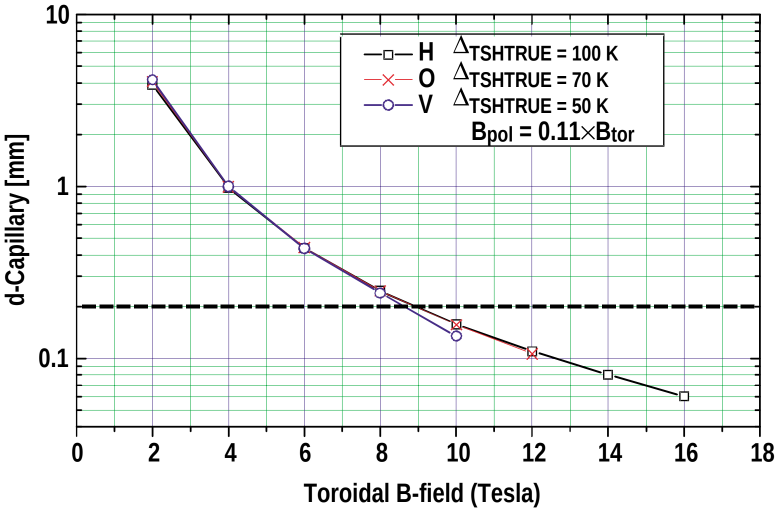

Figure 3.3-4. Integrated transpiration cooled EVOLVE concept with poloidal first wall channels. Capillary diameter versus the toroidal B-field with the superheat ΔT_{sh} as a parameter and for $B_p = 0.11 \times B_T$.

Table 3.3-2. The Integrated Transpiration Cooled Blanket Concept with Poloidal First Wall Channels. Key results of the Mathcad Calculations.

	Dimension	Value
The FW feeding gap width, m	w	1.0
Effective heat flux at the FW, W/m^2	q''_{eff}	2.38×10^6
Total pressure drop within the FW-channel. Pa	Δp_{tot}	2.257×10^3
Capillary diameter needed, mm	dcN1	0.43
Temperature increase over the gap, K	ΔT_{LiG}	48
Temperature at the inner side of the FW, K	T_{wl}	1521
Maximum temperature at the outside of the FW, K	T_{MAXW}	1605
Theoretical limit of superheat, K	$\Delta T_{superheat}$	104
The *true* superheat, K	ΔT_{shtrue}	61.4
Vapor mass flow rate at the outlet window, kg/s	mtot	6.53×10^{-3}
Vapor velocity at the outlet window, m/s	VVO	34
Pressure loss along the channel, Pa	ΔpVTU0Y	<22
The integrated pressure drop in the system, Pa	Δp_{int}	2268
Capillary diameter needed, mm	dcN2	0.43
The total pumping head, Pa	Δp_{Pump}	3893
The overall pressure losses in the system, Pa	Δp_{Drop}	3893
Mass flow rate at the outlet of the blanket manifold, kg/s	$\dot{m}_{outmani}$	12.36
Resulting manifold width,* m	$w_{outmani}$	0.49

*For a limited vapor velocity of 400 m/s.

3.4 The Integrated Transpiration Cooled Blanket Concept with Toroidal First Wall Channels

In the integral toroidal first wall cooling channel concept the liquid lithium is no longer supplied by an separate feeding tube but similar to the integral poloidal concept directly fed from the blanket pool. Figure 3.4-1 shows schematically the geometry of this concept including the routing of the liquid lithium from the tray to the first wall and of the vapor generated there and elsewhere in the system.

The pressure drop of the lithium supply to the first wall within the blanket zone is calculated using the same algorithm as used as in Chapter 3.3.1.

In Figure 3.4-2 the pressure drop integrated over the whole liquid and vapor routing is shown as a function of the feeding gap width w with the width of the radial FW channel gap as an parameter. Additionally the capillary pressure head is shown in order to evaluate the pressure balance.

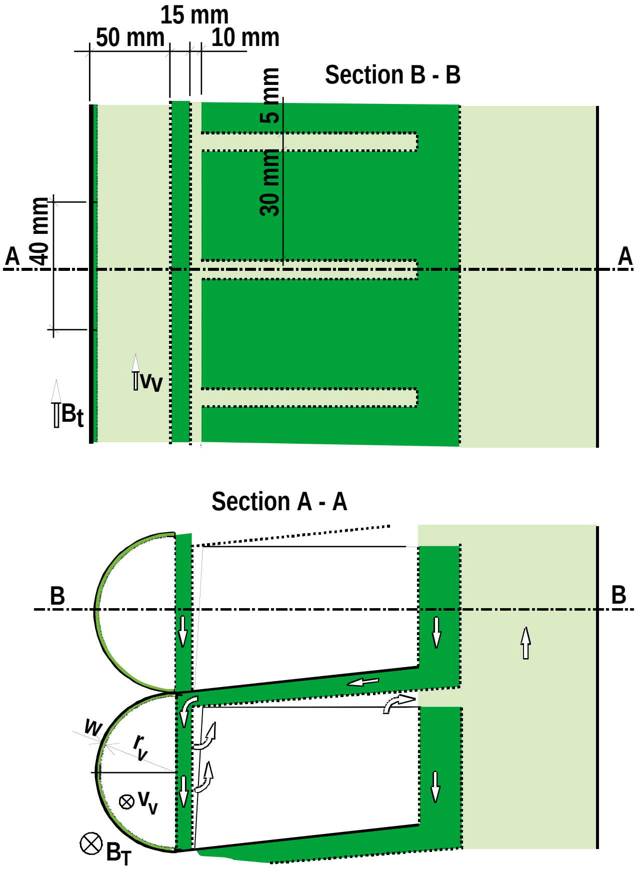

Figure 3.4-1 Transpiration cooled EVOLVE concept with toroidal first wall channels, all sketches are out of scale.

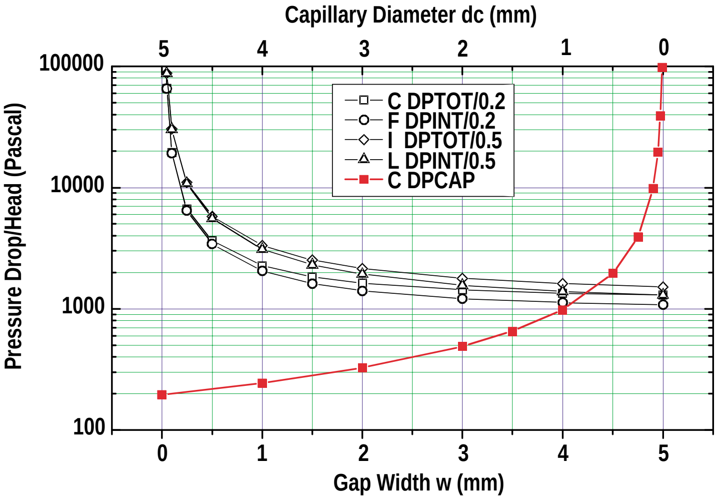

Figure 3.4-2. Integrated transpiration cooled EVOLVE concept with toroidal first wall channels: Pressure drop DPINT as a function of the gap width w, with the effective toroidal thickness of the spacers (Figure 3.2-3) as a parameter and the capillary pressure head DPCAP as a function of the capillary diameter d_c. For comparison the results of the Toroidal First Wall Channel Concept are also given. DPINT ≡ Δp_{int} and DPCAP ≡ Δp_c.

As expected the figure shows the same strong dependence of the integrated pressure drop from the gap width w like the pure Toroidal First Wall Channel Concept. With the selected parameters the additional pressure drop of the lithium in the blanket zone is nearly counterbalanced by the hydrostatic pressure of the lithium pool. Figure 3.4-3 shows the sensitivity of the Integrated Toroidal First Wall Channel Concept from the allowed superheating temperature at the first wall.

From this figure we see that for fusion relevant toroidal field strength >6 Tesla the needed capillary diameter can be kept above 0.2mm — a plausible limiting value with respect to corrosion and plugging — only for true superheating of the lithium at the first wall of about 60 K.

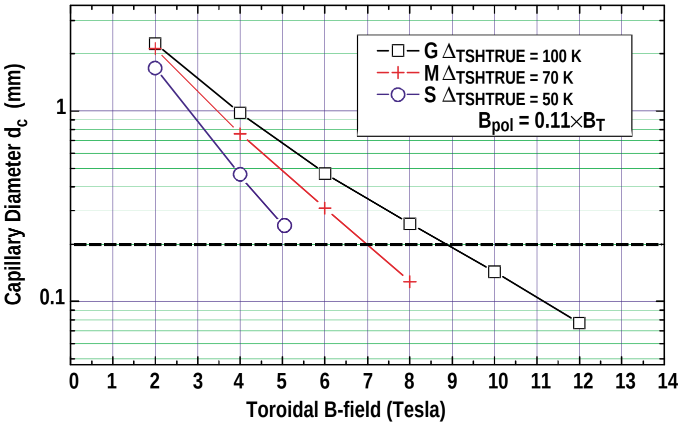

Figure 3.4-3. Integrated transpiration cooled EVOLVE concept with toroidal first wall channels: capillary diameter as a function of the toroidal B-field with the true superheat ΔT_{shtrue} as parameter and for $B_p = 0.11 \times B_T$.

3.5. Comparison between the Integral Transpiration Cooled Blanket Concepts with Toroidal and with Poloidal First Wall Channels

For comparison we listed the results of the toroidal and poloidal flow first wall channel concepts in Table 3.5-1.

Table 3.5-1. Comparison of the Integrated Transpiration Cooled Blanket Concept with Poloidal and Toroidal First Wall Channels.

	Poloidal	Toroidal
The FW feeding gap width, mm	1.0	1.0
Effective heat flux at the FW, W/m^2	2.38×10^6	2.48×10^6
Total pressure drop within the FW-channel, Pa	2257	3280
Capillary diameter needed, mm	0.43	0.30
Temperature increase over the gap	48	41.3
Temperature at the inner side of the FW, K	1521	1514
Maximum temperature at the outside of the FW, K	1605	1590
Theoretical limit of superheat, K	104	104
The *true* superheat, K	61.4	57.7
Vapor mass flow rate at the outlet window, kg/s	6.53×10^{-3}	0.038
Vapor velocity at the outlet window, m/s	34	513
Pressure loss along the channel, Pa	<22	1116
Temperature difference along the channel, K		4.5
The integrated pressure drop in the system, Pa	2268	3062
Capillary diameter needed, mm	0.43	0.32
The total pumping head, Pa	3893	3874
Mass flow rate at the outlet of the blanket manifold, kg/s	12.36	6.63
Resulting manifold width,* m	0.49	0.26
Volume fractions of the tray zone:		
ω_{Li}	0.679	0.621
ω_{Vapor}	0.280	0.323
$\omega_{Tungsten}$	0.041	0.056
Total power of a blanket module, MW	246	192

*For a limited vapor velocity of 400 m/s.

Advantages and disadvantages of the two versions can be stated in the following.

3.5.1 Toroidal Flow

Advantage: Vapor volume of the first wall channel and of the breeding chamber are separated. This allows the application of a higher pressure to the blanket chamber while reducing the pumping needs of the first wall capillary.

Disadvantage: The contribution of high MHD pressure drops in the front wall feeding channel and the high velocity of the vapor at the outlet of the first wall channel is restricting its toroidal length.

3.5.2 Poloidal Flow

Advantage: Short vapor outlet path, therefore problem of the MHD-pressure drop in the first wall feeding gap strongly mitigated due to the parallel flow to the toroidal magnetic field. The radial width of the front channel can be kept small, together with the larger radial feeding gap width (only the volumetrically heat deposition has to be removed) reduce the total MHD pressure drop.

Disadvantage: The vapor volume of the first wall channel and the breeding chamber are directly connected. Therefore an increase of the vapor pressure in the breeding chamber would not enhance the liquid lithium supply to the first wall. Furthermore, a comparison of the dependence of the total pressure drop from the feeding gap width at the first wall in Figures 3,3-3 and 3.4-2 demonstrates that the overall pressure drop of the poloidal flow channel concept is less sensitive to the thickness of the feeding gap than the toroidal flow channel concept.

3.5.3 Parameter Variations:

In Figures 3.5-1 and 3.5-2 the influence of the capillary area fraction β_c of the first wall screen and of the ratio B_p/B_T on the necessary capillary diameter needed for the pressure balance of the FW-channel are compared for the toroidal and poloidal FW-channel concept. The results show that both concepts exhibit nearly the same dependence of the capillary diameter from the area fraction β_c of the capillaries but exhibit very different dependence from the B_p to B_T ratio.

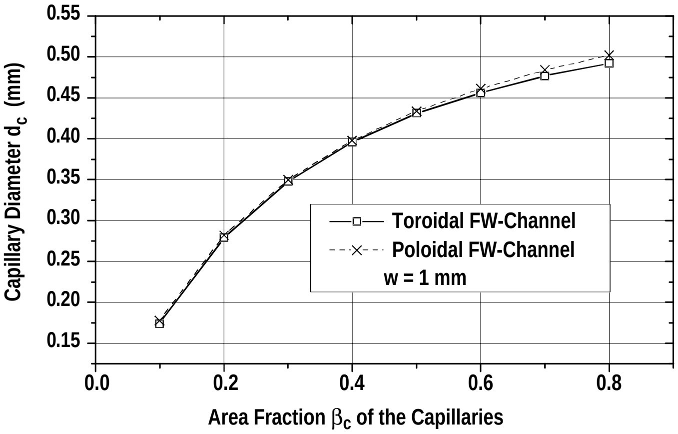

Figure 3.5-1. Capillary diameter d_c as a function of the area fraction β_c for the toroidal FW tube concept.

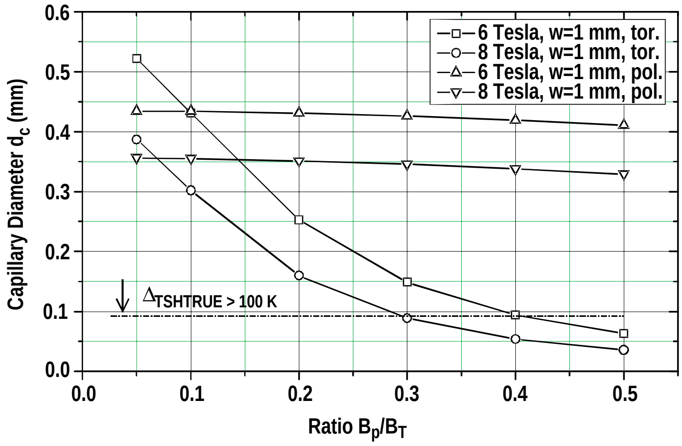

Figure 3.5-2. Capillary diameter d_c as a function of the ratio B_p/B_T for the toroidal and poloidal FW channel concept.

3.6 The Hybrid Transpiration Cooling Concept with Poloidal First Wall Channels

The Hybrid Transpiration Cooling Concept with Poloidal First Wall Channels (Figure 3.6-1) combines a transpiration cooled poloidal first wall channel with the boiling pool blanket concept. In this concept the lithium feeding flow within the pool is mainly in toroidal direction, which reduces the pressure drop in the blanket zone drastically.

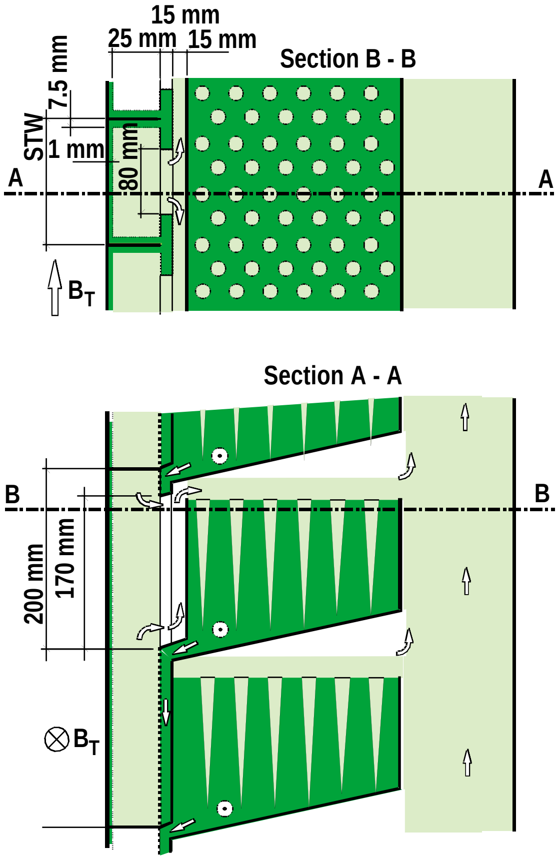

Figure 3.6-1. The hybrid transpiration cooling concept.

The pressure drop of the lithium supply to the first wall within the boiling pool zone is calculated taking into account only the downward flow component in a layer of an assumed thickness $2 \times w_{Li}(R1) \cong 72$ mm. The complete MathCad-program for the Hybrid Transpiration Cooling Concept with poloidal FW-channels including a list of all relevant parameters is given in Appendix 3.A. The main results are given in Table 3.6-1.

Table 3.6-1. The Hybrid Transpiration Cooling Concept. Main Results of the Calculations.

Denomination	Dimension	Value
The FW feeding gap width, mm	w	1.0
Effective heat flux at the FW, W/m^2	q''_{eff}	2.38×10^6
Total pressure drop within the FW-channel, Pa	Δp_{tot}	2.257×10^3
Capillary diameter needed, mm	d_cN1	0.43
Temperature increase over the gap, K	ΔT_{LiG}	48
Temperature at the inner side of the FW, K	T_{wl}	1521
Maximum temperature at the outside of the FW, K	T_{MAXW}	1605
Theoretical limit of superheat, K	$\Delta T_{superheat}$	104
The *true* superheat, kg/s	ΔT_{shtrue}	61.4
Vapor mass flow rate at the outlet window, kg/s	$\dot{m}_{tot}$	6.81×10^{-3}
Vapor velocity at the outlet of FW-channel, kg/s	V_{Vo}	34
Pressure loss along the channel, Pa	ΔPVTU0Y	<20
The integrated pressure drop in the system, Pa	Δp_{int}	1846
Capillary diameter needed, mm	dcN2	0.53
The total pumping head, Pa	Δp_{Pump}	3471
The overall pressure losses in the system, Pa	Δp_{Drop}	3471

3.7 The Transpiration Cooling Experiment

A key heat transfer issue in the feasibility of the transpiration concept is the superheat temperature of lithium on characteristic W-alloy surface. Key verification of this and other assumptions on the conceptual design will be needed.

Figure 3.7-1 shows a schematic of an experiment that could address some of the issues. The goal for this experiment is to demonstrate the proof of principle of the transpiration-cooling concept with a heated surface. The experimental parameters – surface area, heat flux, saturation temperature, chosen liquid metal and finally the applied size and direction of the magnetic field – should allow beside the proof of principle to verify the model given in Section 3.2.2. To enable such verification the following items has to be taken into account:

- Use a screen (capillary structure) on the inner side of a tube with a feeding gap (width w) in between.
- The heated spot as shown should have a cross section of at least $(20*w)^2$ with a heat flux of $>2\ MW/m^{2.}$
- To easy the experiment use for the first tests molybdenum alloy could be used as the structural material.
- The operation in a magnetic field parallel and/or perpendicular to the tube axis should be accommodated.

- Use lithium as liquid metal.
- Keep the whole test section (tube) at saturation condition of lithium at 1200°C.
- Before starting the experiment degas the inner surface of the test section and the lithium at high temperature to guarantee blanket relevant conditions, especially with respect to the possible superheating of lithium at the first wall.

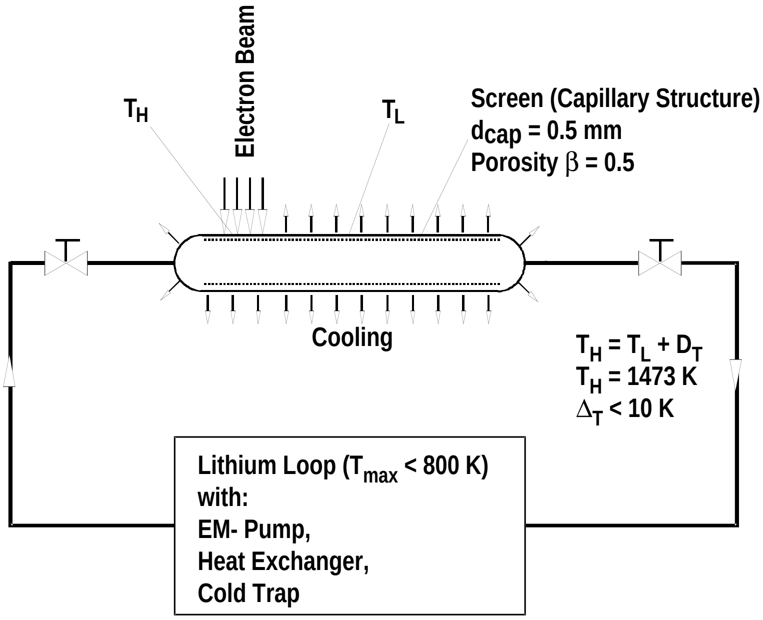

Figure 3.7-1. The proposed transpiration cooling experiment at Sandia Laboratories.

For the proposed experiment the following parameters are recommended:

Tube diameter, mm	D_{Tube}	= 30 to 50
Gap width, mm	w	= 1
Capillary diameter, mm	d_c	= 0.5
Screen thickness, mm	t_c	= 0.5
Capillary open area, %	β_c	= 50
Saturation temperature of lithium, K	T_s	= 1473
Corresponding pressure, MPa	p_{sat}	= 0.034

3.8 Summary, Critical Issues and Conclusion

Based on detail analysis, results from our calculations show that the concept of transpiration cooling of the first wall is feasible. Integral transpiration cooled first wall and blanket concepts are also modelled. Finally a hybrid transpiration cooling concept, combining a poloidal oriented transpiration cooled FW-channel and a tray with a boiling pool has been investigated showing also that the concept is feasible.

Related critical issues are:

- Roughness of the first wall would limit the superheating.
- Superheating of volumetrically heated liquid metal. What is the influence of the Helium generated within the liquid metal with respect to the formation of nucleation centers?
- Influence of the thermal conductivity and the wetting behaviour of the structural material on the capillary pressure (pumping) under very high heat load.
- Does it exist a self-healing mechanism if boiling in the feeding gap occurs?
- How to restore transpiration conditions after an unintended break through of the liquid lithium through the porous walls, during operation (less probable) or during start up?
- Filling and wetting of the first wall feeding gap and the porous structure at the startup.

From the modeling calculations conducted we conclude:

- Using a thermally insulated double walled lithium feeding tube the pressure drop along the feeding tube fulfils the criteria for MHD controlled feeding.
- The overall pressure drop and the resulting capillary diameter of the toroidal flow FW concept are very sensitive to an increase of the B_p/B_T ratio, which would be different between inboard and outboard blankets.
- The overall pressure drop of the poloidal flow FW concept is less sensitive to the thickness of the feeding gap than the toroidal flow FW concept.
- Due to the shorter length of the vapor flow path the velocity at the corresponding outlet of the vapor is much lower for the poloidal design.
- Poloidal front channel concepts allow larger margin on the superheat uncertainty. Therefore they allow more freedom on the selection of tray geometric parameters.
- A hybrid system as sketched in Figure 3.6-1 is analyzed and may help to reduce the problem of high vapor velocities in the FW channels.

The elaborated Integrated Transpiration Cooling Concepts are only first proposed, but are based on supporting thermo-hydraulic and magneto-hydrodynamic calculations using first principle correlations. For any further development intense design work in close connection with MHD thermal hydraulics experts is necessary.

Appendix 3.A <u>Thermo-Physical Data of Lithium and Tungsten</u>

In order to perform the calculations a consistent set of the thermo-physical data of lithium and tungsten are collected from the relevant literature and correlations of the temperature dependence of the different quantities generated:

3.A.1 <u>Lithium, Liquid</u>

3.A.1.1 <u>Melting point [A1]:</u>

$$T_{MP} = 454 \ K$$

3.A.1.2 Saturation ressure as a function of the temperature T (K) in the range $T < T_{MP} < 1800$ K [A1]

$$P_S(T) = 10^5 \cdot e^{17.307 - \frac{1.929 \cdot 10^4}{T} - 0.724 \cdot \ln(T)} \quad [Pa]$$

$$P_S(T) = 3.429 \cdot 10^4 \quad [Pa]$$

3.A.1.3 Density in the range $T < T_{MP} < 1800$ K [A1]

$$\rho_{Li}(T) = 564.823 - 0.10229 \cdot T \quad [kg/m^3]$$

$$\rho_{Li}(1473) = 414.15 \quad [kg/m^3]$$

3.A.1.4 Specific heat in the range $T < T_{MP} < 1700$ K [A1]

$$\begin{aligned} cp_{Li}(T) = {} & (10.31995 - 0.03276 \cdot T + 7.17476 \cdot 10^{-5} \cdot T^2 - 8.21098 \cdot 10^{-8} \cdot T^3 + 5.14743 \cdot 10^{-11} \cdot T^4 \\ & - 1.67108 \cdot 10^{-14} \cdot T^5 + 2.19718 \cdot 10^{-18} \cdot T^6) \cdot 10^3 \quad [Ws/kgK] \end{aligned}$$

$$cp_{Li}(1473) = 4.203 \cdot 10^3 \quad [Ws/kgK]$$

3.A.1.5 Thermal conductivity in the range $T_{MP} < T < 3600$ K [A2]

$$\lambda_{Li}(T) = 24.8 + 45.0 \cdot 10^{-3} \cdot T - 11.6 \cdot 10^{-6} \cdot T^2 \quad [W/mK]$$

$$\lambda_{Li}(1473) = 65.92 \quad [W/mK]$$

3.A.1.6 Electrical conductivity in the range $T_{MP} < T < 2200$ [A2]

$$\sigma e_{Li}(T) = 0.9249 \cdot 10^9 \cdot T^{-1} + 2.3167 \cdot 10^6 - 0.7131 \cdot 10^3 \cdot T$$

$$\sigma e_{Li}(1473) = 1.894 \cdot 10^6 \quad [A/Vm]$$

3.A.1.7 Surface tension in the range $T_{MP} < T < 1700$ [A2]

$$\sigma s_{Li}(T) = (438.98 - 18.44 \cdot 10^{-3} \cdot T - 132.20 \cdot 10^{-6} \cdot T^2 + 37.44 \cdot 10^{-9} \cdot T^3) \cdot 10^{-3} \quad [N/m]$$

$$\sigma s_{Li}(1473) = 0.245 \quad [N/m]$$

3.A.1.8 Dynamic viscosity in the range $T_{MP} < T < 3600$ [A2]

$$\mu_{Li}(T) \quad = e^{-4.16435-0.63740\cdot\ln T+\frac{292.1}{T}} \quad [Pa\cdot s]$$

$$\mu_{Li}(1473) = 1.812\cdot 10^{-4} \quad [Pa\cdot s]$$

3.A.1.9 Heat of vaporization in the range 500 < T < 1800 K [A1]

$$H_{Li}(T) \quad = (21815.728+3.75633\cdot T-0.00582\cdot T^2+1.92067\cdot 10^{-6}\cdot T^3-2.09696\cdot 10^{-10}\cdot T^4)\cdot 10^7$$

$$H_{Li}(1473) = 1.987\cdot 10^7 \quad [Ws/kg]$$

3.A.2 Lithium Vapor at Saturation

3.A.2.1 Density ρv_{Li} in the range 1300 < T < 1800 [A1]

$$\rho v_{Li}(T) \quad = e^{-158.202-7.532\cdot 10^{-3}\cdot T+\frac{292.1}{T}+22.679\cdot\ln T} \quad [kg/m^3]$$

$$\rho v_{Li}(1473) = 0.021 \quad [kg/m^3]$$

3.A.2.2 Viscosity μv_{Li} in the range 1300 < T < 1800 [A1]

$$\mu v_{Li}(T) \quad = (-5.59048 + 0.10371\cdot T)\cdot 10^{-7} \quad [Pa\cdot s]$$

$$\mu v_{Li}(1473) = 1.472\cdot 10^{-5} \quad [Pa\cdot s]$$

3.A.3 Tungsten (W-5Re) [A3]

3.A.3.1 Density

$$\rho_W = 19300 [kg/m^3]$$

3.A.3.2 Specific heat

$$cp_W(T) \quad = 128 + 0.033\cdot T - 3.4\cdot 10^{-6}\cdot T^2 \quad [Ws/kg K]$$

$$cp_W(1473) = 162.704 \quad [Ws/kgK]$$

3.A.3.3 Heat conductivity in the range 1000 < T < 2400 K decreases with increase in Re content

$$\lambda_W(1500) = 85.0 \quad [W/mK]$$

3.A.3.4 Electrical conductivity in the range 1000 < T < 2400 K

$$\sigma e_W(1400) = 2.0 \cdot 10^6 \quad [A/Vm]$$

3.A.4 Reference

[A1] N.B. Vargaftik, Tables on the Thermophysical Properties of Liquids and Gases, 2nd edition, Hemisphere Publishing Corp., 1975.

[A2] V.A. Kirillin (Editor), Liquid-Metal Coolants for Heat Pipes and Power Plants, Hemisphere Publishing Corp., 1990.

[A3] “APEX Interim Report, On the Exploration of Innovative Concepts for Fusion Chamber Technology,” UCLA-ENG-99-206, UCLA-FNT-107, November, 1999.

4 Boiling Blanket and Experiments

4.1. Introduction

In order to achieve high power density and high power conversion efficiency in future fusion plants, several first wall and blanket features are required. High power density means the coolant heat removal capability must be significant and high power conversion implies that the first wall and blanket must operate at high temperatures. The first wall material must have high thermal conductivity and high performance at elevated temperature, which leads to a refractory alloy such as tungsten. Because of its reduced tensile strength at high temperature and neutron fluence, the operating pressure should be minimized to reduce primary stress and uniform temperatures should be maintained throughout the blanket to reduce thermal stresses. Finally, the large heat of vaporization for lithium makes it ideal as a heat removal medium for such a blanket. For this evaluation, we analyzed an EVOLVE system design that operates nominally at 1200°C and 0.037 MPa (saturation conditions), with a surface heat flux of 2 MW/m^2 and a maximum neutron wall loading of 10 MW/m^2.

The EVOLVE [1] (EVaporation Of Lithium and Vapor Extraction) concept was developed to address these specific issues. It uses the vaporization of liquid lithium to remove heat from the fusion system. Trays of liquid lithium are stacked poloidally behind the first wall and receive nuclear heating from the neutrons. At issue in this study is the localized vapor fraction distribution produced in the trays. This vapor fraction determines the total nuclear heating in the lithium, the tungsten trays and the surrounding wall. To address this issue three magnetic field and liquid lithium pool interaction regimes were envisioned and studied.

First, a generalized methodology is proposed for the determination of the vapor fraction profile for the regime of limited or negligible magnetic field interaction with the liquid lithium pool. This methodology uses an empirically derived formulation based on isothermal experiments conducted at the University of Wisconsin [2]. A standard drift-flux model was used to empirically fit data from liquid metal experiments utilizing nitrogen gas as the vapor. We apply this model to the liquid lithium trays. Neglecting magnetic field effects on the liquid lithium trays, predictions indicate large vapor fractions extending up to 65% at the top of the pool.

A second methodology, proposed by Malang [3], is utilized to determine the vapor fraction when magnetic field effects are moderately coupled to the liquid lithium. We define moderate magnetic interaction regime as one where the magnetic field influences the liquid lithium by damping its motion, but does not significantly affect the nucleate boiling process. Mass, momentum and energy balances are performed to validate a potential heat removal scenario where vapor channels are assumed to be held open by vapor momentum, frictional and magnetic field effects. Vapor fraction distributions in this situation for the pool are significantly reduced with values in the range of 6%–12%.

Finally, large magnetic field effects could have significant damping on the nucleate point process. In this regime the pool depth would have to be sized to control the heat input and the maximum temperature of the tungsten structure. For this regime, the effects of magnetic field on boiling liquid metal are reviewed and potential experiments to study this effect are proposed.

References

[1] C.P.C. Wong et al., “Evaluation of the Tungsten Alloy Vaporizing Lithium First Wall and Blanket Concept,” Proc. of the 14th ANS Topical Meeting on the Technology of Fusion Energy, Fusion Technology, Vol. **39**, 2, Part 2, (2001) p. 815.

[2] J. Casas and M.L. Corradini, “Study of Void Fraction and Mixing of Immiscible Liquids in a Pool Configuration by an Upward Gas Flow,” Nuclear Technology, Vol. **24** (1) August (1993).

[3] S. Malang, personal communication, consultant to the APEX program, year 2000–2001.

4.2. Vapor Fraction Distribution with Negligible Magnetic Effect on the Lithium Pool

In a situation where the magnetic effect on the lithium is minimal or none, it can be expected that the liquid lithium will boil like any other liquid metal. The vapor fractions will affect energy deposition in the liquid lithium from neutron streaming. As a first approximation it is assumed that the nuclear deposition or heating is directly proportional to the fluid density or inversely proportional to the vapor fraction. A drift-flux model was used with empirically based data from liquid metal experiments with nitrogen gas injection.

A two-dimensional calculation was performed on the nominal design of a tungsten tray filled with liquid lithium. The tray is 50 cm long with a nominal lithium pool depth of 15 cm. The depth of liquid lithium was divided into five axial regions for analysis (3 cm each), with lateral nodes characterized by the boiling length scale [Eq. (4.2.1)] given by the Taylor bubble size,

$$\text{width} = 2\pi\,[3\sigma/(g\Delta\rho)]^{1/2} \quad . \tag{4.2.1}$$

Based on the above approximation, 8–10 cm is the lateral “cell size”. Based on a 50 cm tray width, our analysis considered a “slice” of the blanket with 5 radial cells and 5 axial regions to model the boiling process. A uniform void distribution of 17% [1] was initially chosen to estimate the neutronic loading (heat deposition).

All the energy deposited in the liquid lithium and in the tungsten tray at the bottom of the cell would vaporize the saturated lithium pool. For each axial region within an individual cell, the quantity of lithium vaporized is then used to determine the volumetric vapor flux (j_g) and the dimensionless superficial gas velocity (J_g), used in the drift-flux model, for bubbly or churn-turbulent flow regimes [2]. Provided below are Eqs. (4.2.2–4.2.7) relating the drift-flux formulation for the vapor fraction.

$$\langle \text{void} \rangle = J_g/[C_o\langle J_g\rangle + C_1] \quad , \tag{4.2.2}$$

$$J_g = j_g/[\sigma_f \Delta\rho g/\rho_f^2]^{1/4} \quad , \tag{4.2.3}$$

$$Z = \mu_f/[\rho_f(\sigma_f/(\Delta\rho g))^{1/2}\sigma_f]^{1/2} \quad \text{(Ohnesorge number)} \quad , \tag{4.2.4}$$

$$j_g = m_g/(\rho_g A) \quad , \tag{4.2.5}$$

$$C_o = 0.248\ln(Z)+3.52 \quad , \tag{4.2.6}$$

$$C_1 = 0.502(H/D) + 0.00727\ln(Z) - 0.124(H/D)\ln(Z) - 0.0295 \quad . \tag{4.2.7}$$

The constants C_o and C_1 were empirically derived from prior tests with mercury, woods metal, water, Freon, dodecane and silicone oils. Representative values for C_o and C_1 are 1.5 and 2.2 respectively, for the boiling lithium scenario. C_o and C_1 were derived from experimental fits from these other fluids. The correlations [Eqs. (4.2.6) and (4.2.7)] were applied with the appropriate dimensionless groups to obtain these values. Nitrogen gas was bubbled up through the pool and the vapor fraction was determined. In the drift-flux model the vapor fractions are driven by the low vapor density of lithium at saturation conditions of 1200°C, and by the nuclear heating loads applied to the tungsten and lithium. Figure 4.2-1 shows the relationship of vapor fraction versus superficial gas velocity.

Because of the low vapor density of lithium at the nominal conditions large superficial gas velocities (ranging between 7 and 30) are seen for this boiling scenario. This means that generally we see vapor fractions in the range of 60% for the boiling of lithium. The superficial gas velocity scales directly with the nuclear heating, but at sufficiently high values of superficial gas velocity (~ 5) changes in nuclear heating will minimally affect the vapor fraction.

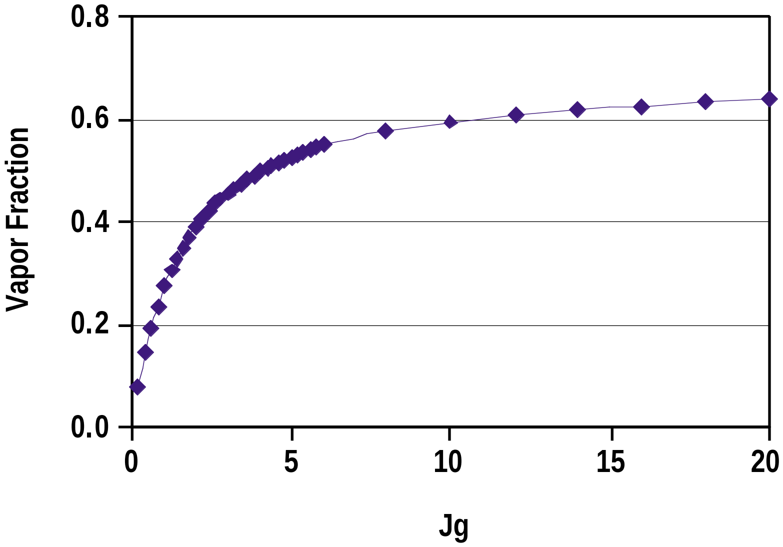

Figure 4.2-1. Vapor fraction versus superficial gas velocity for lithium at 1200°C and 0.037 MPa.

The calculations are iterated with the two-dimensional neutronics calculations as follows. The assumed initial void fraction was 17%, which gives us heating loads that are applied to the drift-flux model. New vapor fraction values are obtained and used to define densities in the neutronics calculation [3]. New nuclear heating values were determined based on the calculated vapor fractions and the iteration process continued until convergence is reached on the vapor fraction. Figure 4.2-2 shows the final iterated vapor fraction values at various vertical positions in the pool for the five cells. Because the outer channel, number 5, receives added heat load from the tungsten wall the vapor fraction distribution is slightly larger than in channel 4.

Large vapor fractions were predicted using the Casas and Corradini drift-flux correlation. Other analytical expressions were found in the literature to check against. A study of void distribution in a fuel pool in the event of a liquid metal fast breeder reactor (LMFBR) accident was examined [4]. This study was concerned with analytical and empirical expressions of vapor distribution in an internally heated boiling pool. Vertical profiles of the vapor fraction in the heated pool were experimentally obtained and favorably compared to proposed analytical models. An analytical expression for bubbly flow was proposed [Eq. (4.2.8)]:

$$\alpha = \quad 1-\exp[-GY/(\lambda\rho_v BV_{inf})] \quad . \tag{4.2.8}$$

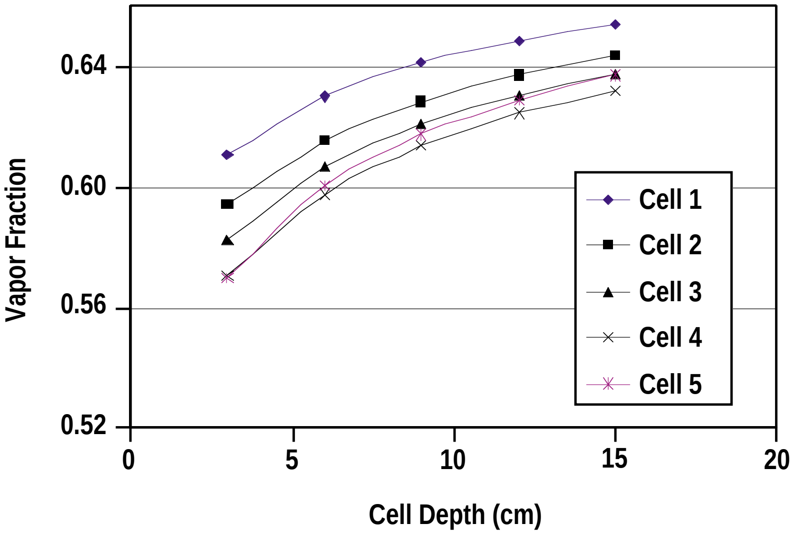

Figure 4.2-2. Final cell vapor fractions.

The paper also proposed a classic drift-flux expression [Eq. (4.2.9)] to predict macroscopic pool vapor fraction behavior:

$$\alpha = 1-1/[1+2GY/(\lambda\rho_v V_{inf})]^{1/2}. \qquad (4.2.9)$$

G = heat consumed in vaporization
Y = axial elevation
λ = heat of vaporization
ρ_v = vapor density
B = $1.55(J_g/V_{inf})^{0.65}$ (empirical parameter)
V_{inf} = terminal rise velocity
J_g = Superficial vapor velocity

Both analytical expressions use average heat generation rates for the entire pool. Figure 4.2-3 shows a comparison of the Casas and Corradini drift-flux void distribution using the central channel, with the two analytical expressions from Kazimi and Chen.

One can see that general agreement exists between the three correlations as to predicting vapor fraction distribution in a boiling pool of liquid lithium with negligible magnetic fluid coupling. It is also apparent that the vapor fractions may be very large (>60%) in this instance.

The vapor fraction appears to be significant but can be reduced by increasing the operating pressure. Figure 4.2-4 shows the center channel vapor fraction distribution for various operating pressures using this drift-flux model. It is clear that increases in pressure can significantly reduce pool vapor fractions. Problems arise because of operating limitations on the tungsten metal in the trays. Nevertheless, it is important to understand the effect for potential redesigns and in case of material changes in future designs. Higher operating pressure is advantageous to reducing system vapor fraction.

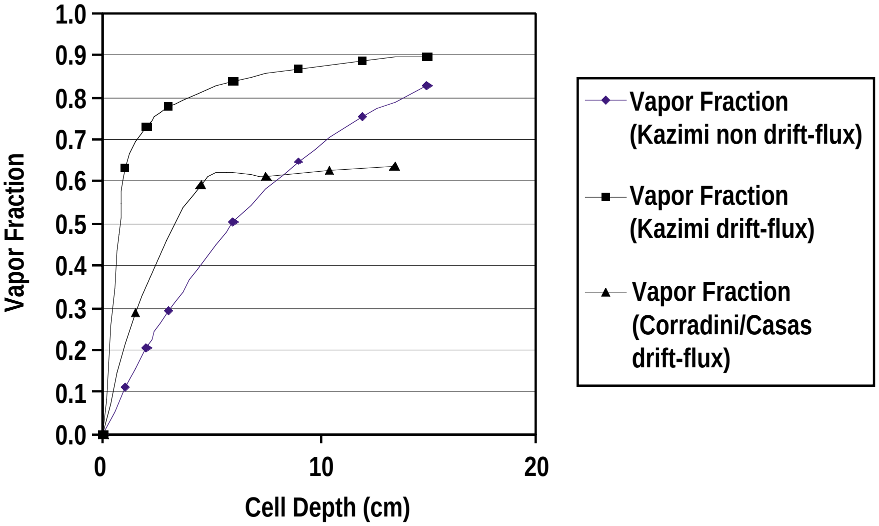

Figure 4.2-3. Total pool vapor fraction versus pool depth.

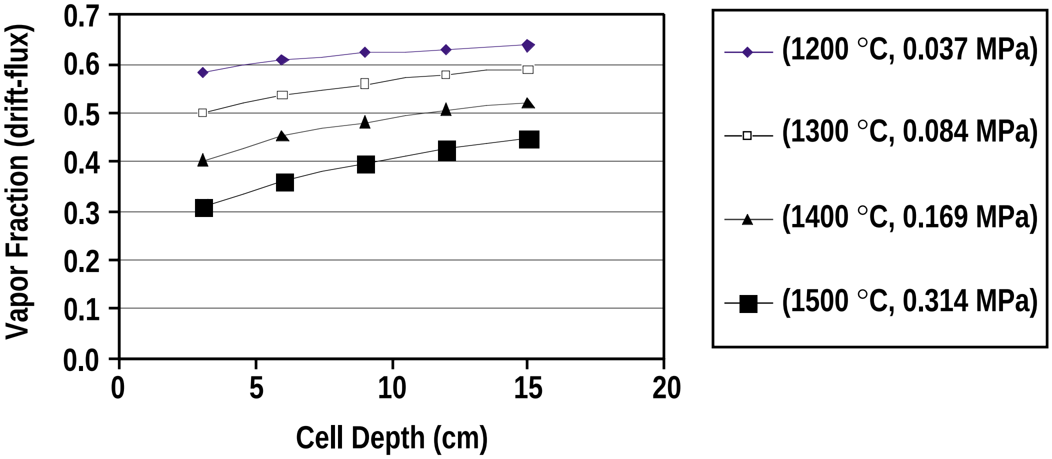

Figure 4.2-4. Vapor fraction comparison at different operating saturation conditions.

References

[1] S. Malang, personal communication, consultant to the APEX program, year 2000–2001.

[2] J. Casas and M.L. Corradini, "Study of Void Fraction and Mixing of Immiscible Liquids in a Pool Configuration by an Upward Gas Flow," Nuclear Technology, Vol. **24** (1) August (1993).

[3] M.E. Sawan, "Neutronics Performance Characteristics of the EVOLVE First Wall/Blanket System," Proc. of the 14th ANS Topical Meeting on the Technology of Fusion Energy, October 15-19, 2000, Park City, Utah, to be published in Fusion Technology.

[4.] M.S. Kazimi and J. C. Chen, "Void Distribution in Boiling Pools with Internal Heat Generation," Nuclear Science and Engineering, Vol. **64**, (1), January (1978).

4.3. Vapor Fraction Distribution with Moderate Magentic Effect on the Lithium Pool

Given a moderate magnetic effect an alternative boiling/evaporation picture may emerge with lower vapor fractions. If there is a moderate magnetic interaction with the boiling liquid lithium pool, the magnetic field with vapor momentum and frictional effects may be adequate to maintain open vapor channels and allow high speed evaporation from the channel interface with lower vapor fraction. We define moderate magnetic interaction as one where the magnetic field influences the liquid lithium by damping its bulk motion but does not affect the nucleate boiling process. By providing artificial nucleation sites, we could trigger the formation of vapor channels on the bottom of the lithium trays and space them as needed for heat removal. The potential for smaller vapor fractions will exist with the stable vapor channels. Figure 4.3-1 provides a schematic of the vapor channels along with a definition of channel and cell size.

Conduction heat transfer analysis and liquid superheat determine the maximum cell spacing. Past liquid metal boiling data indicate superheats as large as 200°C, which would correspond to a maximum cell size of approximately 8 cm. Now a complete analysis combining mass, momentum (pressure) and energy balances will determine the appropriate vapor distribution and spacing to maintain channel integrity and remove sufficient nuclear heat loads. Parameters held constant throughout the analysis were heat generation rate, channel height (15 cm), applied magnetic field (10 T) and electrical conductivity (3×10^6 A/Vm). Using final iterated heat loading values, a conservative average was utilized to produce the heat generation rate of 20 W/cm^3.

The iterative process starts with a specific cell size. A guess is then made as to the vapor exit velocity from the channel. Based on that guess an energy balance is performed equating the energy deposited in the cell and the flux of lithium vaporized and exiting the channel. Again, all energy is used to vaporize the saturated liquid lithium. From this the channel exit diameter is determined. Directly from the channel diameter the vapor fraction is geometrically determined and using mass continuity the vapor velocity from the interface of the channel can be found. This leads directly to the liquid lithium velocity that is feeding the liquid/vapor interface. This liquid velocity is important because the movement of the liquid lithium provides the magnetic retarding force (J×B) for the liquid. This is included in the pressure balance that determines whether the vapor channel is stable. The static head of the liquid lithium must be balanced against the kinetic, friction and magnetic pressure head loss terms defined below. Equations (4.3.1–4.3.4) provide specifics about the various terms.

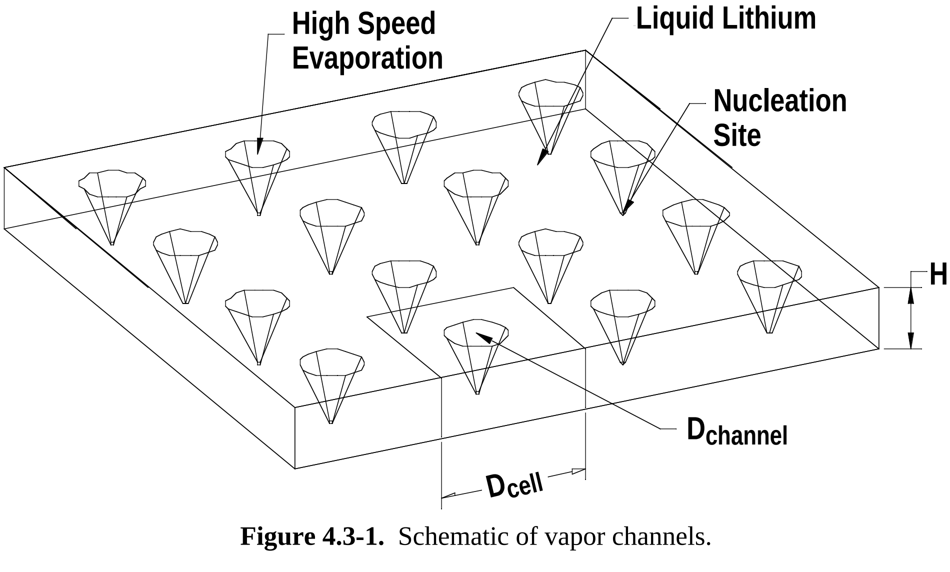

Figure 4.3-1. Schematic of vapor channels.

$$\Delta P(\text{static}) = \rho_{\text{liq}} gH = \Delta P(\text{friction}) + \Delta P(\text{kinetic}) + \Delta P(\text{magnetic}) \quad , \tag{4.3.1}$$

$$\Delta P(\text{friction}) = (0.03)\rho_{\text{vap}}(H/D)v^2 \quad , \tag{4.3.2}$$

$$\Delta P(\text{kinetic}) = \rho_{\text{vap}} v^2/2 \quad , \tag{4.3.3}$$

$$\Delta P(\text{magnetic}) = \sigma v_{\text{liq}} B^2 (L/2) \quad . \tag{4.3.4}$$

If these pressure terms do not balance then the channel will collapse. Iteration on the channel vapor exit velocity is performed until a balance is achieved. Parametric analyses were performed for various cell sizes to determine critical operating characteristics (i.e., channel diameter, void fraction and vapor exit velocity). The balances were performed using two potential length scales (L) in the magnetic head term, the vapor channel or cell size. Since there was uncertainty as to which diameter to use (cell or channel), both were considered and plotted. Significant differences are not seen on the channel diameter or cell vapor fraction plots (Figures 4.3-2 and 4.3-3).

It is clear from Figure 4.3-2 that significantly reduced vapor fractions occur with a moderate magnetic field effect in conjunction with vapor momentum and frictional effects to balance the static liquid head and hold open the channels for vapor outflow.

The presence of the previously calculated vapor channels is not dependent on the allowable superheat of the lithium fluid. Conduction heat transfer analyses were performed to determine the maximum cell spacing for 200 K and 50 K superheat values for the liquid lithium. At 200 K, the cells can be spaced, as much as 8 cm apart before bulk nucleation will occur, and at 50 K superheat the cells can be up to 4 cm apart. From Figure 4.3-2, it is apparent that the optimized cell size is less than either value (4 or 8 cm) and that the superheat issue should not be a problem for the high-speed evaporation scenario presented. Cell spacing will probably end up in the 2 to 3 cm range based on the vapor fraction optimization presented in Figure 4.3-2.

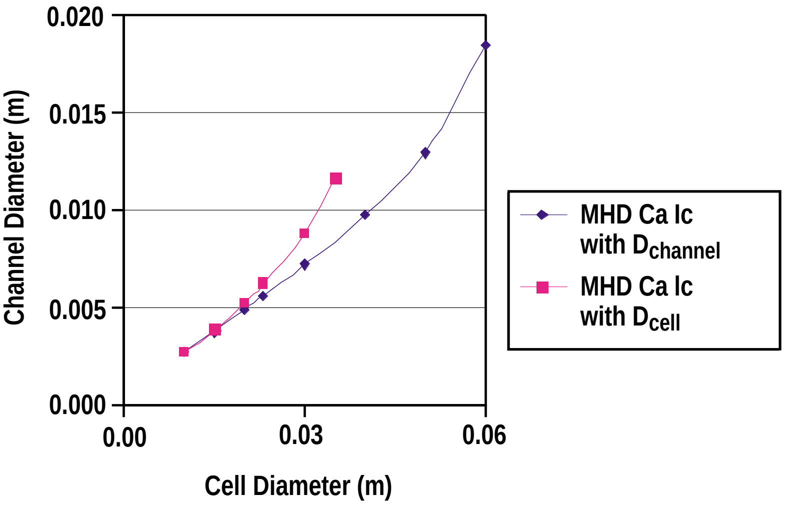

Figure 4.3-2. Channel diameter versus cell diameter.

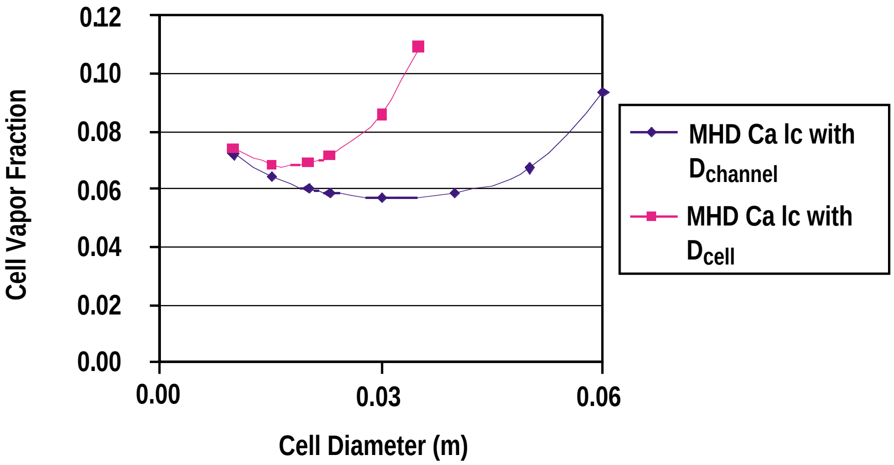

Figure 4.3-3. Cell vapor fraction versus cell size.

4.4. Future Work and Experiments

The possibility that the magnetic field may produce a significant interaction with the liquid lithium pool boiling must be addressed. A study of mercury pools in magnetic fields of strengths around 0.45 T, showed significant effects on the bubble departure diameter and its departure frequency during boiling [1]. This has a marked impact on the boiling heat transfer process, but does not seem to alter the onset of boiling at these field strengths. This could be confirmed by flow visualization experiments and at larger magnetic fields. These experiments will also be useful in studying the possibility of vapor channel formation discussed in Chapter 3.

Based on previous work [2] and the current state of knowledge regarding pool boiling of liquid metals in the presence of a magnetic field, experiments are required to understanding further the magnetic field effects on the boiling of lithium. A set of experiments is needed to determine the onset of nucleate boiling and to quantify the effect of various magnetic field strengths on the boiling process; i.e., its onset and bubble dynamics. Once boiling is achieved with the liquid metal in the presence of a magnetic field, real-time visualization experiments of the developing flow patterns would be of great help in identifying the expected flow regime with surface heating and the addition of heating the fluid. Then a physical model explaining the effects of the magnetic field on the onset of boiling and the boiling flow regime can be developed. These experiments will allow us to determine the boiling rate and heat transfer for a given volumetric heat flux, which in turn will lead to the pool depth needed to balance heat generation and heat removal.

References

[1] M.S. Kazimi and J. C. Chen, "Void Distribution in Boiling Pools with Internal Heat Generation," Nuclear Science and Engineering, Vol. **64**, (1), January (1978).

[2] M.A. Bertodano and P.S. Lykoudis, "Nucleate Pool Boiling of Mercury in the Presence of a Magnetic Field," Int. Journal of Heat and Mass Transfer, Vol. **41**, (1998) 3491-3500.

4.5. Conclusions

The EVOLVE plant design has developed a solid wall concept that employs a liquid lithium pool with boiling for power production behind the first wall. Analyses were performed to determine the vapor fraction distribution within this pool of boiling liquid lithium subjected to a transverse magnetic field. Values for vapor fraction ranging up to 65%, and as low as 6% to 12% were estimated depending on the assumed effect the magnetic field had on the pool of liquid lithium (small or moderate). Experiments to examine the effect the magnetic field has on liquid lithium have been proposed. These experiments are crucial in the development of the EVOLVE plant design concept in order to confirm the expected flow regime and verify its performance and feasibility.

5. Leakage Assessment for EVOLVE First Wall

5.1. Introduction

The first wall of EVOLVE will be cooled by the evaporation of lithium whose temperature will be in the range 1200 and 1400°C, corresponding to saturation pressures of 0.035 and 0.15 MPa, respectively. In the toroidal flow concept, these pressures will create very low primary stresses in tungsten first wall tubes of 6 cm diameter and 3-mm wall thickness. However, cyclic surface heat flux will create cyclic thermal stresses, which may lead to initiation and propagation of fatigue cracks through the first wall. This section first provides an estimate of the number of cycles necessary to propagate a crack through the first wall as a function of initial flaw depth (which may be initiated as a fatigue crack or is present initially as a defect). Next, the leakage rate of lithium through a fatigue crack is calculated approximately. Finally, the impact of the lithium leakage rate on cooling of the first wall and plasma contamination is discussed. It should be noted that the impact of lithium leakage on reactor performance was analyzed earlier by Jones et al. [1] in connection with UWMAK-II and NUWMAK design studies. However, the temperature of lithium in these designs was much lower than in EVOLVE.

5.1 References

[1] R.H. Jones, R.W. Conn, and R.F Schafer, “Effect of First Wall Flaws on Reactor Performance,” Nuclear Engineering and Design/Fusion, Vol. 2, pp. 175-188 (1985).

5.2. Fatigue Crack Growth

Consider a section of the EVOLVE first wall tube of inner radius r_i and outer radius r_o, as shown in Figure 5.2-1(a), subjected to a cosinusoidally varying surface heat flux Q Cos θ. It is cooled internally by lithium at a temperature T_c. It is assumed that a semi-elliptical axial o.d. surface crack [Figure 5.2-1(b)] is initiated (or pre-exists) at the plasma edge ($\theta = 0$) of the first wall, which is subjected to cyclic thermal stresses due to plasma on-off cycles. The objective is to calculate the number of cycles required to drive the crack through the thickness until it becomes throughwall. Details of the thermal and fracture mechanics analyses are given in Appendix 5.A.

5.2.1. Thermal Analysis

The solution for the temperature field in the first wall is as follows:

$$T(r,\theta) = \begin{cases} T_c + \dfrac{Q\, r \operatorname{Cos}\theta}{\kappa} + \left\{ \dfrac{r}{r_i}\left(\dfrac{r_i}{r_o}\right)^2 + \dfrac{r_i}{r} \right\} b_1 \operatorname{Cos}\theta \text{ for } |\theta| \le \dfrac{\pi}{2} \\ T_c \text{ for } \pi > |\theta| > \dfrac{\pi}{2} \end{cases} \qquad (5.2\text{-}1a)$$

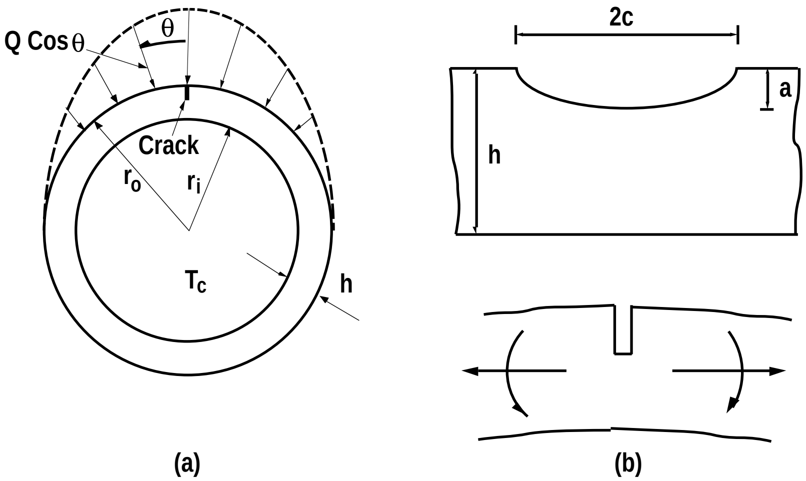

Figure 5.2-1. (a) Geometry and surface heat flux loading on EVOLVE first wall and (b) two views of the geometry of semi-elliptical surface crack and the membrane and bending loading on it.

where κ is thermal conductivity, and

$$b_1 = -\frac{Qr_i}{\kappa}\,\frac{1-\dfrac{\kappa}{h_f r_i}}{1+\left(\dfrac{r_i}{r_o}\right)^2+\dfrac{\kappa}{h_f r_i}\left\{1-\left(\dfrac{r_i}{r_o}\right)^2\right\}}. \tag{5.2-1b}$$

where h_f is the heat transfer coefficient. The section-averaged temperature T_{avg} is given by

$$T_{avg} = T_c + \frac{\dfrac{Qr_o}{3\kappa}\left[1-\left(\dfrac{r_i}{r_o}\right)^3\right]+\dfrac{b_1 r_i}{3r_o}\left[1-\left(\dfrac{r_i}{r_o}\right)^3+3\left(1-\dfrac{r_i}{r_o}\right)\right]}{\dfrac{\pi}{2}\left[1-\left(\dfrac{r_i}{r_o}\right)^2\right]} \tag{5.2-2}$$

5.2.2. Stress Analysis

For generalized plane strain deformation conditions, the equibiaxial stresses in the first wall are given by the following equation:

$$\sigma_\theta(r,\theta)=\sigma_z(r,\theta)=\frac{E\alpha}{1-\nu}\left(T_{avg}-T(r,\theta)\right) \tag{5.2-3}$$

where σ_θ and σ_z are the hoop and axial stresses, respectively, E and ν are Young's modulus and Poisson's ratio, respectively, and α is coefficient of thermal expansion. The maximum stress occurs in the section at θ = 0. The average membrane stress at this section is given by

$$\sigma_m = -\frac{E\alpha}{1-\nu}\left[\frac{Qr_o}{2\kappa}\left(1+\frac{r_i}{r_o}\right)+b_1\left\{\frac{r_i}{2r_o}\left(1+\frac{r_i}{r_o}\right)+\frac{r_i}{h}\ln\left(\frac{r_o}{r_i}\right)\right\}+T_c-T_{avg}\right] \tag{5.2-4a}$$

and the maximum bending stress at the plasma edge (from equivalent linearized stress distribution) is

$$\sigma_b = -\frac{E\alpha}{1-\nu}\left[\frac{Qh}{2\kappa}+b_1\left\{\frac{h}{2r_i}\left(\frac{r_i}{r_o}\right)^2+\frac{6r_i}{h}\left(1-\frac{r_i+r_o}{2h}\ln\frac{r_o}{r_i}\right)\right\}\right] \tag{5.2-4b}$$

where $h = r_o - r_i$ = thickness of first wall tube.

5.2.3. Fatigue Crack Growth Analysis

Consider an elliptical axial surface flaw of axial length (2c) and depth (a) at the plasma edge (θ = 0) of the o.d. surface [Figure 5.2-2(b)]. The elastic stress analysis results [Eqs. (5.2-4a-b)] show that initially the plasma edge is under compressive stresses, which would imply that cracks initiating at this location would not propagate under normal conditions. However, with the accumulation of creep strain (both thermal and irradiation-induced), the stresses in the first wall will relax during plasma burn. Here it is assumed conservatively that the compressive stresses are fully relaxed during plasma burn, but reappear as tensile stresses of equal magnitude when the plasma is turned off. These cyclic tensile stresses will create driving forces for fatigue crack propagation both in the axial and the thickness directions. The axial and through-thickness crack driving forces (stress intensity factor ranges) are given in Appendix 5.A.

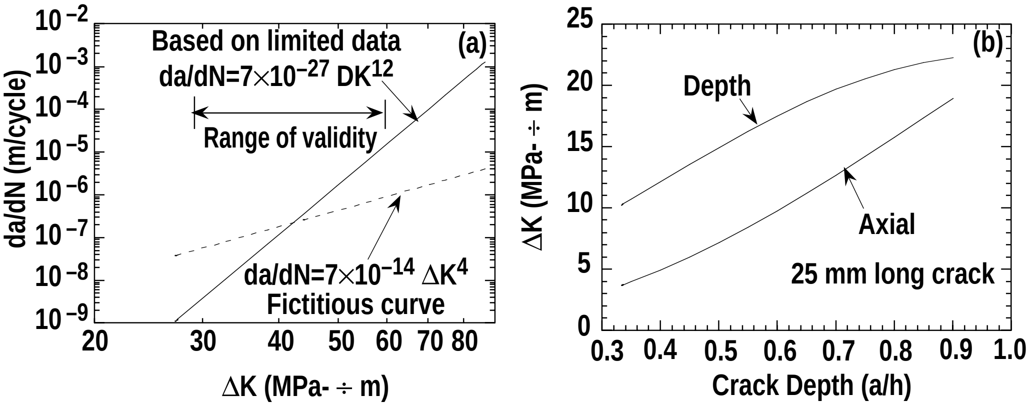

Figure 5.2-2. (a) Available fatigue crack growth curve and a fictitious fatigue crack growth curve for tungsten at room temperature and (b) variations of axial and through-thickness stress intensity factor ranges with crack depth for a 25 mm long crack subjected to 2 MW/m^2 surface heat flux; calculations assume T_c = 1200°C and h_f = 40,000 W/m^2/°C.

To conduct fatigue crack growth analysis, fatigue crack growth data for tungsten are needed. Limited room temperature data [1] including the equation [given in Eq. (5.2-5)] and its range of validity, are shown as a solid line in Figure 5.2-2(a).

$$\frac{da}{dN} = 7x10^{-27}(\Delta K)^{12} \tag{5.2-5}$$

where da/dN is in m/cycle and ΔK is in MPa-√m and the range of validity is for ΔK between approximately 30 and 60 MPa-√m.

Typical stress intensity factor ranges for a 25 mm long surface crack of various depth subjected to 2 MW/m^2 surface heat flux are shown in Figure 5.2-2(b). Note that the stress intensity factors are significantly below the range of validity of the fatigue crack growth data. Therefore, the predicted life is dependent strongly on how the available data is extrapolated to lower stress intensity factors. Two lines, one solid and one dashed [Figure 5.2-2(a)], were used for extrapolation. The solid line is an extrapolation using Eq. (5.2-5) (exponent = 12) as suggested by the limited data. The exponent appears to be relatively large compared to those for other materials (usually between 2 and 6). Therefore, the dashed line was also used as a fictitious curve with a lower exponent (= 4) but with approximately the same da/dN value as at the midrange of the data. Figure 5.2-3(a) shows the variation of calculated crack depth (a/h) with cycles for an initially 25 mm long, 1 mm deep surface crack subjected to a surface heat flux of 2 MW/m^2. Figure 5.2-3(b) shows the variation of the cycles to failure (defined as cycles to propagate the crack to 90% depth) with initial flaw depth. As expected, the predicted fatigue crack growth lives could vary between 4×10^5 to 10^{10} cycles, depending on whether the data is extrapolated using an exponent 4 or an exponent 12. The predicted lives also depend on the initial flaw depth.

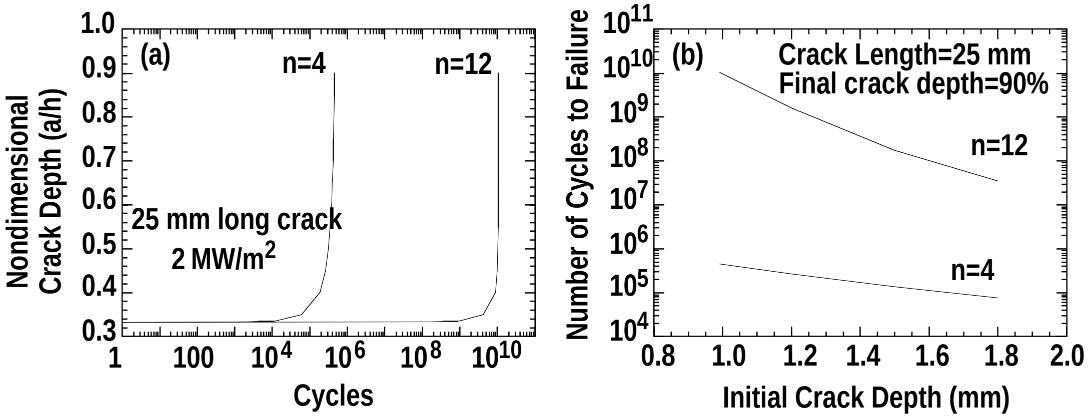

Figure 5.2-3. (a) Crack depth versus cycle plots for an initially 25 mm long, 1 mm deep (a/h=0.33) crack and (b) number of cycles to failure versus initial crack depth for an initially 25 mm long crack subjected to 2 MW/m^2, calculated using the two fatigue crack growth curves in Figure 5.2-2(a).

5.2.4. Conclusions for Fatigue Crack Growth Analysis

A model for analyzing fatigue crack growth life of the EVOLVE first wall due to plasma on-off cycles has been developed. An initially semi-elliptical surface crack is assumed to exist and the number of cycles required to propagate the crack axially and through the thickness is calculated using the model and available fatigue crack growth data for tungsten. Unfortunately, the available range of fatigue crack growth data of tungsten is at room temperature and is significantly above the expected stress intensity factor range for a surface heat flux of 2 MW/m^2. Consequently, the calculated life is strongly dependent on how the data is extrapolated. The predicted fatigue crack growth lives could vary between 4×10^5 to 10^{10} cycles, depending on whether the data is extrapolated using an exponent 4 or an exponent 12. However, fatigue crack growth data for tungsten at lower stress intensity factor ranges and at ≥1200°C are needed to make a more reliable prediction of fatigue life of the EVOLVE first wall.

Reference

[1] I. Roman and D. Jinchuk, "Fatigue Crack Growth in a Sintered Tungsten Alloy," Fatigue of Engineering Materials and Structures, Vol. 5, No.1, pp. 71-76 (1982).

5.3. Leakage Analysis

Since the pressure of the lithium vapor in the EVOLVE first wall tube is quite low (0.035–0.15 MPa), surface tension effects will play an important role in determining if leakage of liquid lithium will occur through a tight fatigue crack in the first wall into the plasma chamber. Capillary effects may even prevent leakage of liquid lithium through a tight fatigue crack if lithium does not wet the crack flanks [Figure 5.3-1(a)].

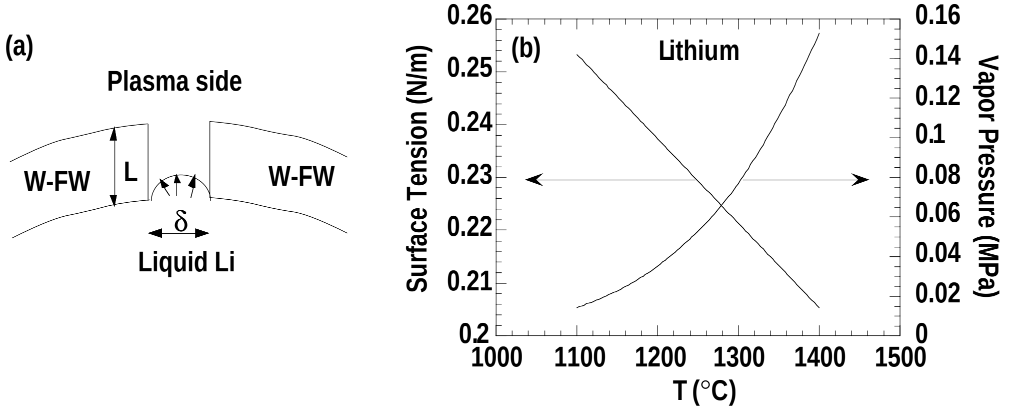

Figure 5.3-1. (a) Surface tension in lithium film in equilibrium with lithium vapor pressure for the non-wetting case and (b) variations of saturation vapor pressure and surface tension of liquid lithium with temperature.

5.3.1. Crack Opening Area

A critical parameter for calculating leakage rates is the crack opening area (A), which is the pressure-dependent opened area of the crack. The crack opening area of an axial throughwall crack in a thin-walled tube was calculated by the Zahoor model [1] which is given by

$$A = 2\pi c_e^2 V_o \sigma_h / E \qquad (5.3\text{-}1)$$

where σ_h = hoop stress = pR/h, p is the differential pressure across the tube wall, E is the Young's modulus, and R and h are the mean radius and thickness of tube, respectively,

$$V_o = 1 + 0.64935\lambda_e^2 - 8.9683\text{x}10^{-3}\lambda_e^4 + 1.33873\text{x}10^{-4}\lambda_e^6,$$

$\lambda_e^2 = c_e^2 / Rh$,

$c_e = c\left[1 + \frac{F}{2}\left(\frac{\sigma_h}{S_y}\right)^2\right]$,

$F = 1 + 1.2987\lambda^2 - 2.6905x10^{-2}\lambda^4 + 5.3549x10^{-4}\lambda^6$,

$\lambda^2 = c^2 / Rh$, and

S_y is the yield strength and c is the crack half-length.

The crack opening displacement δ, which is defined as the pressure-dependent maximum gap between the top and bottom faces of the crack can be obtained from the crack length and crack opening area by assuming the opened crack to be elliptical in shape.

5.3.2. Surface Tension Effect – No Wetting of Crack Flanks

If lithium does not wet the flanks of the crack [Figue 5.3-1(a)], the capillary pressure head (Δp_C) will for a crack with opening displacement (COD) δ is given by

$$\Delta p_c = \frac{2\sigma}{\delta}, \qquad (5.3\text{-}2)$$

where σ = surface tension of liquid lithium. The lithium vapor pressure in the tube has to overcome Δp_{cap} before the lithium film at the crack entrance is ruptured and any leakage can occur.

The variations of vapor pressure and surface tension of liquid lithium with temperature are given in Figure 5.3-1(b). For typical values of surface tension (0.24 N/m) and saturated vapor pressure (0.04 MPa) of lithium at 1200°C, the minimum crack opening displacement necessary before any leakage of liquid lithium can occur is 0.012 mm. For comparison, the minimum pinhole diameter for any leakage of liquid lithium to occur at 0.04 MPa is 0.024 mm. On the assumption that a crack of zero initial opening is opened by the pressure of lithium vapor acting alone on the tube wall (tube diam. = 6 cm, wall thickness = 3 mm), Figure 5.3-2(a) shows the variation of the COD of a 25, 51, and 76 mm long throughwall axial crack with temperature. Figure 5.3-2(a) also includes the minimum COD needed for leakage to occur. For typical values of temperature expected for EVOLVE, no leakage will occur at time t=0 for crack lengths <51 mm. For a 76 mm long crack, immediate leakage can occur only if the temperature of liquid lithium is >1330°C. For comparison, the minimum pinhole diameter for any leakage of liquid lithium to occur is shown in Figure 5.3-2(b).

The crack opening analysis reported here does not include the time-dependent effect of thermal creep on deformation. However, primary stresses are so low that the effect of creep on the COD may be very small. Thermal stresses are assumed to be relaxed out quickly by creep. The effect of irradiation-induced creep on the COD has also been ignored.

Currently, the consensus is that liquid lithium does wet tungsten at these temperatures. Consequently, there will be no beneficial capillary effect and liquid lithium may, in fact, ooze out into the plasma chamber by capillary pumping even in the absence of a pressure difference across the first wall. In the next section, leakage rates through the fatigue crack will be estimated on the assumption that lithium does wet tungsten.

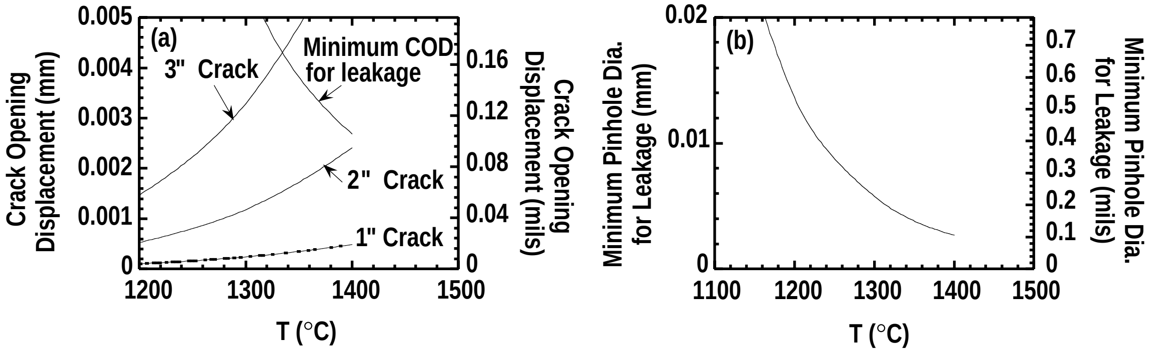

Figure 5.3-2. (a) Variations of CODs for 25 mm (1 in.), 51 mm (2 in.) and 76 mm (3 in.) long cracks and the minimum COD needed for leakage to occur with temperature and (b) minimum pinhole diameter needed for leakage to occur in the first wall.

5.3.3. Liquid Lithium Leakage Analysis – Wetting Case

In keeping with current consensus, it is assumed that liquid lithium wets the flanks of the fatigue crack and a meniscus of liquid lithium rises through the crack in the first wall will acting as a capillary pump (Figure 5.3-3), it is also assumed here that the liquid does not flash to vapor inside the fatigue crack. The total driving pressure for leakage is $p_0+\Delta p_c$, where p_0 = lithium pressure in the first wall tube and Δp_c is the capillary head defined in Eq. (5.3-2). The liquid lithium is assumed to vaporize at the crack exit plane.

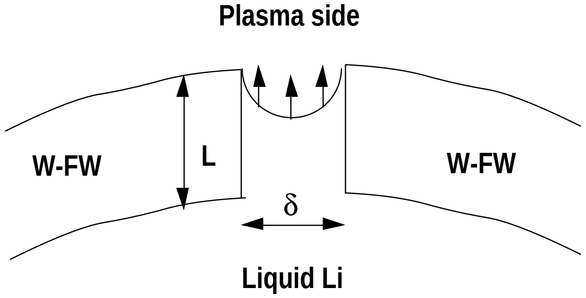

Figure 5.3-3. Liquid lithium meniscus rising through the fatigue crack acts as a capillary pump if liquid lithium wets the fatigue crack flanks. Lithium evaporates into the plasma chamber at the exit plane.

5.3.3.1. Inertia Dominated Flow

If inertia forces dominate viscous forces and capillary forces, and it is assumed that lithium flows through the crack as a single-phase incompressible liquid, the pressure ($p_{exit}=0$) at the crack exit plane is related to the pressure at the crack entrance plane (p_o) by the following equation:

$$P_{exit} = p_o - \Delta p_e - \Delta p_f - \Delta p_k - \Delta p_{MHD} = 0, \qquad (5.3\text{-}3)$$

where

Δp_e = entrance pressure loss,

Δp_f = friction pressure loss,

Δp_k = pressure loss due to bends and protrusions in the crack flow path, and
Δp_{MHD} = pressure drop due to MHD forces.

The entrance pressure loss is given by

$$\Delta p_e = \frac{\left(\frac{dm}{dt}\right)^2}{2\rho C_D^2}, \tag{5.3-4}$$

where $\frac{dm}{dt}$ = mass flow rate, ρ = mass density of lithium, and C_D = coefficient of discharge.

The friction pressure loss is given by

$$\Delta p_f = f\frac{L}{D}\frac{\left(\frac{dm}{dt}\right)^2}{2\rho}, \tag{5.3-5a}$$

where L = flow path length (can be approximated by tube wall thickness), D = crack hydraulic diameter, and f = friction factor. The hydraulic diameter is given by

$$D = \frac{4A}{P}, \tag{5.3-5b}$$

where A = crack opening area and P = wetted perimeter of crack at the external surface. The hydraulic diameter $D \approx 2\delta$ for a crack with high aspect ratio.

The friction factor f for laminar flow ($N_R < 2000$) is given by

$$f = \frac{64}{N_R}, \tag{5.3-5c}$$

where N_R is the Reynold’s number

$$N_R = \frac{\rho v D}{\mu}, \tag{5.3-5d}$$

μ = coefficient of viscosity, and v is flow velocity.

The friction factor f for turbulent flow (N_R>2000) is given by

$$f = \left[C_1 \log\left(\frac{D}{\varepsilon}\right) + C_2\right]^{-2}, \tag{5.3-5e}$$

where ε = surface roughness of crack flank,

$$C_1 = \begin{cases} 2.00 \text{ for } D/\varepsilon > 100 \\ 3.39 \text{ for } D/\varepsilon < 100 \end{cases}, \tag{5.3-5f}$$

and

$$C_2 = \begin{cases} 1.14 \text{ for } D/\varepsilon > 100 \\ 0.866 \text{ for } D/\varepsilon < 100 \end{cases}. \tag{5.3-5g}$$

The pressure loss due to bends and protrusions in the crack flow path is given by

$$\Delta p_k = e_v \frac{\dot{M}^2}{2\rho}, \tag{5.3-6a}$$

where e_v = total loss coefficient over the crack flow path length which can be determined from experiments as

$$e_v = eL, \tag{5.3-6b}$$

where e is the number of velocity heads (one velocity head = $1/2\rho v^2$) lost per unit flow length of a fatigue crack. Typically, a 45° turn results in a loss of 0.4 velocity head (without MHD loss). A best-fit to experimental data on fatigue crack in a girth weld suggests a value of e equal to 6 velocity heads per mm of crack flow path.

In addition, there is an MHD pressure drop for which the following correlation has been developed by L. Bühler [2] for flows with Hartmann number >1.

$$\Delta p_{MHD} = \sigma_{liq} B^2 LKv \tag{5.3-7a}$$

where σ_{liq} = electrical conductivity of liquid (A/V-m), B = magnetic field (Tesla), and K is given by

$$K = \frac{1}{1+\frac{\alpha}{\beta}} \tag{5.3-7b}$$

$$\beta = \sigma_{wall}/\sigma_{liq} \tag{5.3-7c}$$

$$\alpha \approx 1 \text{ for circular tubes and thin gaps,} \tag{5.3-7d}$$

σ_{wall} = electrical conductivity of tube wall,

$$\text{Hartmann number } H = \sqrt{\frac{\text{Magnetic Forces}}{\text{Viscous Forces}}} = BD\sqrt{\frac{\sigma}{\mu}}, \text{ and} \tag{5.3-7e}$$

$$\text{Interaction parameter } N = \frac{\text{Magnetic Forces}}{\text{Inertia Forces}} = \frac{H^2}{N_R}. \tag{5.3-7f}$$

Equation (5.3-3) is generally applicable for cases where the crack is relatively open. In contrast, fatigue cracks are non-planar and usually very tight, particularly at low pressures. In such cases, it is more realistic to assume that viscous forces dominate inertia forces.

5.3.3.2. Flow with negligible-inertia

Below some critical Reynold's number, inertia effects can be neglected in comparison to viscous effects, and pressure drops due to entrance and flow bends can be ignored. In such cases, the following pressure conditions apply

$$P_{exit} = p_o + \Delta p_c - \Delta p_f - \Delta p_{MHD} = 0, \tag{5.3-8}$$

where Δp_f = pressure drop due to viscous effect. The capillary pressure head Δp_c is defined in Eq. (5.3-2) and the MHD pressure drop Δp_{MHD} is defined in Eq. (5.3-7a).

The pressure drop due to incompressible viscous effects (Poiseuille flow) is related to the fully developed flow velocity by (in the absence of magnetic field)

$$\Delta p_f = \frac{32\mu L}{D^2} v. \tag{5.3-9}$$

where μ = coefficient of viscosity, L = flow path length (can be approximated by tube wall thickness), A = crack opening area, v = flow velocity, and D = crack hydraulic diameter defined in Eq. (5.3-5b).

Combining Eqs. (5.3-7a), (5.3-8), and (5.3-9), and solving for v,

$$v = \frac{p_o + \Delta p_c}{\sigma_{liq} B^2 LK + \frac{32\mu L}{D^2}} \tag{5.3-10}$$

Results for Liquid Lithium Mass Flow Rate. Calculated variations of mass flow rate with lithium vapor pressure in the first wall tube are shown for initial crack openings of 1 and 10 μm in Figsures 5.3-4(a) and 5.3-4(b), respectively. As expected, capillary effects are important at low pressures that are of interest to EVOLVE (0.015 to 0.15 MPa) and at lower initial crack openings. On the other hand, MHD effects are negligible for a planar crack of small opening. Whether the same conclusion holds for an irregular-shaped fatigue crack remains open. For larger crack openings, MHD pressure drops are important. The maximum leak rates for a 25 mm long crack at 0.15 MPa are 3×10^{-3} and 0.15 gm/s for initial crack opening of 1 and 10 μm, respectively. These values should be taken as upper bounds to the mass flow rate because evaporation of lithium within the fatigue crack (possibly close to the inlet) will probably reduce the mass flow rate significantly.

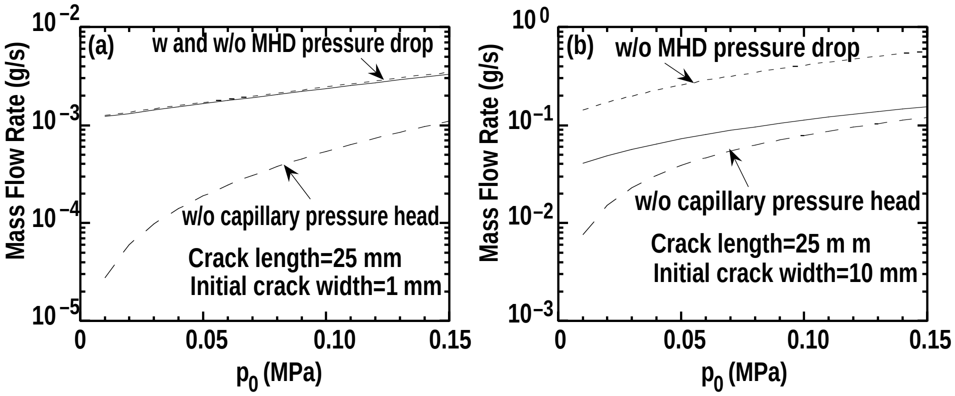

Figure 5.3-4. Variation of mass flow rate with liquid lithium pressure for a 25 mm long throughwall crack with initial opening (a) 1 μm and (b) 10 μm. Magnetic field B=6 T.

To check whether the assumptions that Hartmann number >1 and Reynold's number is low are satisfied, they are plotted against lithium pressure in Figures 5.3-5(a-b). Note that in the pressure regime of interest to EVOLVE, the Hartmann number is >1 for initial crack opening of 1 µm and >12 for initial crack opening of 10 µm. Although the Reynold's number is >10 at an initial crack opening of 10 µm, the interaction parameter is also ≥10 (Figure 5.3-6) for pressures ≤0.05 MPa, indicating that magnetic forces dominate inertia forces. It is evident that the assumption of low Reynold's number is increasingly violated at higher pressures and larger initial crack opening, and consequently inertia forces cannot be ignored.

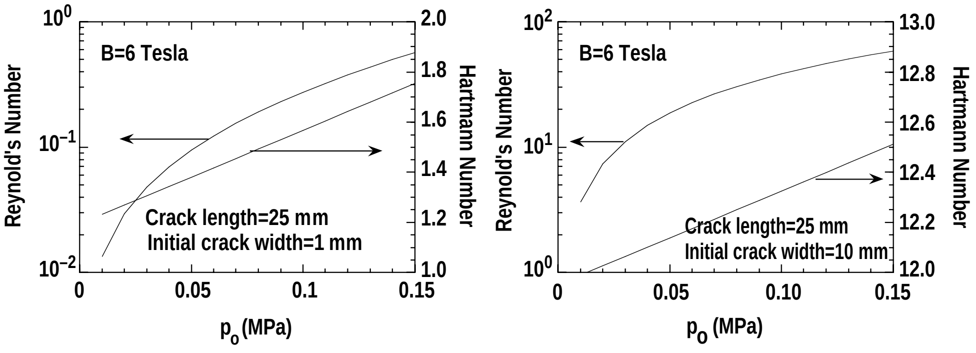

Figure 5.3-5. Variation of Reynold's number and Hartmann number with liquid lithium pressure for a 25 mm long throughwall crack with initial opening (a) 1 µm and (b) 10 µm.

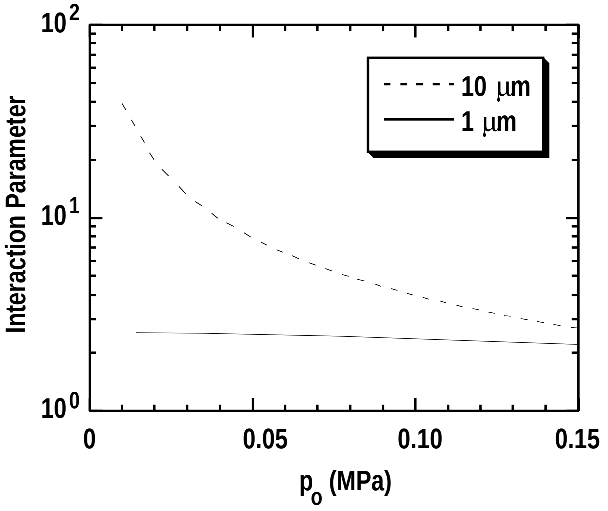

Figure 5.3-6. Variation of Interaction parameter with liquid lithium pressure for a 25 mm long throughwall crack with initial openings 1 and 10 µm.

5.3.4. Lithium Vapor Leakage

Keeping in mind that the inlet pressure is close to saturation vapor pressure of lithium, as the liquid lithium enters the crack, viscous pressure drop will cause the liquid to flash to vapor (Figure 5.3-7). The heat of vaporization will be supplied by the surface heat flux as well as the surrounding liquid (in fact, flashing will occur even without a surface heat flux). The local velocity of the vapor immediately after flashing will be high, but it will be quickly damped by high viscous dissipation owing to the tight and meandering nature of fatigue cracks. Also, because of the large flow path length to width ratio (L/δ) of fatigue cracks, equilibrium will be

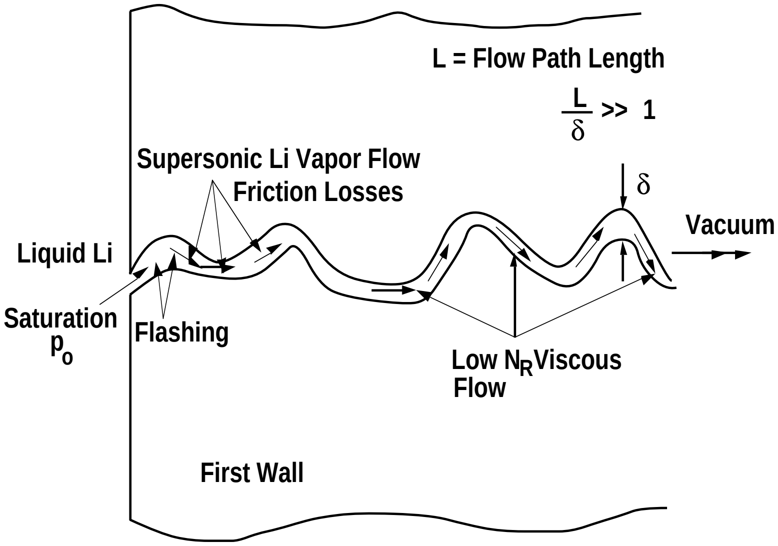

Figure 5.3-7. Schematic of liquid lithium entering a tight and meandering fatigue crack, flashing to high velocity vapor phase close to the inlet, and quickly slowing down to low Reynold's number flow due to dissipations.

restored within some multiples of the crack width close to the entrance. In this section the complex non-equilibrium phenomena related to flashing of liquid lithium to vapor phase inside the fatigue crack and subsequent viscous dissipation including possible two-phase flow are not considered. Instead the lithium vapor leakage rate is estimated by assuming that lithium enters the fatigue crack in a vapor phase. This is equivalent to assuming that the pressure drop within the non-equilibrium transition zone inside the fatigue crack is small compared to the overall pressure drop and the mass flow rate of lithium vapor is determined by equilibrium of pressure and viscous forces.

5.3.4.1. Gas flow characteristics in vacuum systems

The description of gas flow in vacuum systems is generally separated into three regimes, depending on the values of a nondimensional parameter called the Knudsen number defined as the ratio between the mean free path (L) of a molecule and the characteristic dimension of the flow channel [3]. For our case, the characteristic channel dimension is the crack opening displacement δ. In the high pressure range, where the mean free path of a gas molecule is small compared to δ (Knudsen number <0.01), collision between molecules occur more frequently than collision between molecules and the channel wall. Conventional flow in this range is called viscous flow, which can be analyzed by theory of hydrodynamics. At low pressures, the mean free path is large compared to δ and the gas flow is limited by molecular collision with the wall of the flow channel. Flow at large Knudsen numbers (Knudsen number > 1) is called molecular flow. Transition from viscous to molecular flow occurs at intermediate values of Knudsen number (0.01 < Knudsen number < 1) where both types of collision are important. The mean free path length (L in m) of any gas molecule is related to its temperature (T in K), molecular weight (M gram), pressure (p in MPa) and viscosity (μ in Pa-s) by the following equation [3]

$$L = 1.1451\text{x}10^{-2} \frac{\mu}{p}\left(\frac{T}{M}\right)^{1/2} \tag{5.3-11}$$

Since the mean free path of air at 25°C is related to pressure, the flow regimes for air at 25°C can be expressed as follows [3]:

Viscous flow occurs when $p\delta > 6.79\times10^{-7}$
molecular flow occurs when $p\delta < 6.79\times10^{-9}$, and
transition flow occurs when $6.79\times10^{-9} < p\delta < 6.79\times10^{-7}$,

where p is in MPa and δ is in m. The above criterion was used by Jones et al. [4] for analyzing leakage rate of lithium vapor into the plasma chamber. However, if we use the properties of lithium vapor at 1200°C, the flow regimes can be expressed as follows:

Viscous flow occurs when $p\delta > 2.5\times10^{-6}$,
molecular flow occurs when $p\delta < 2.5\times10^{-8}$, and
transition flow occurs when $2.5\times10^{-8} < p\delta < 2.5\times10^{-6}$,

Since the temperature of lithium in the Jones et al. [4] study was 500°C ($p\delta = 4\times10^{-12}$ MPa-m), the lithium vapor flow was primarily molecular. In the case of EVOLVE, $p\delta = 3.5\times10^{-7}$ at 1200°C, 7.8×10^{-7} at 1300°C, and 1.6×10^{-6} MPa-m at 1400°C. Consequently, the flow is likely to be in the transition range at the temperatures of interest to EVOLVE. Since there is no reliable model for predicting gas leakage rate in the transition regime, the lithium vapor leakage rate was calculated by both the incompressible viscous flow theory and the molecular flow theory.

Calculation of leakage rate for gas is more complicated than that for liquid because the density of gas is a strong function of pressure. A flow rate Q_g can be defined relating it to the volumetric flow rate and the pressure (p) at which it is measured as follows [3]:

$$Q_g = p\frac{dV}{dt} \tag{5.3-12a}$$

Note that the unit for Q_g is MPa-m^3/s. The ideal gas law can be used to show that

$$Q_g = p\frac{dV}{dt} = kT\frac{dN}{dt} \tag{5.3-12b}$$

where T is absolute temperature, N is the number of molecules of gas, and k is Boltzmann constant. The molar leakage rate can be calculated by Eq. (5.3-12b) from a knowledge of Q_g. We assume that the gas flow occurs under isothermal condition. The flow rate Q_g for fully developed incompressible viscous (Poiseuille) flow is then given by [3]

$$Q_g = \frac{AD^2\Delta p}{32\mu L}\frac{p_o + p_{exit}}{2} \approx \frac{AD^2 p_o{}^2}{64x10^{-6}\mu L} \text{ in MPa-m}^3\text{/s} \tag{5.3-13}$$

where the lengths are in m, p_o is the inlet pressure (MPa) and p_{exit} is the exit pressure (MPa) taken as ≈ 0, and Δp (MPa) is the pressure drop through the first wall and μ is in Pa-s. The other symbols are defined after Eq. (5.3-9).

For pure molecular flow, the molecules have a Maxwellian distribution of velocity and the arithmetic mean flow velocity is given by [3]

$$v_m = \left(\frac{8RT}{\pi M}\right)^{1/2} = 145.51\left(\frac{T}{M}\right)^{1/2} \text{ in m/s} \tag{5.3-14}$$

where R = N_Ak is the molar universal gas constant, N_A is Avogadro's number, M is molecular weight (g/mole). The molecular flow rate Q_g through an elliptically opened crack of length 2c (in m) is given by [3]

$$Q_g = \frac{2\sqrt{2}}{3\pi L}\frac{A^2}{\left[c^2 + \left(\frac{\delta}{2}\right)^2\right]^{1/2}} v_m(p_o - p_{exit}) \approx \frac{43.67 p_o A^2}{Lc}\left(\frac{T}{M}\right)^{1/2} \text{ in MPa-m}^3\text{/s} \tag{5.3-15}$$

Mass flow rate (in g/s) corresponding to Q_g is given by

$$\frac{dm}{dt} = 120272\frac{Q_g M}{T} \tag{5.3-16}$$

where Q_g is in MPa-m^3/s, M is in g/mole, and T is in K.

Calculated lithium vapor leakage rate – Figures 5.3-8(a) and 5.3-8(b) show the variation of lithium vapor leakage rate through a 25 mm long crack with temperature under saturation pressure by molecular flow and by viscous flow for initial crack opening of 10 and 1 μm, respectively. Note that molecular flow controls the mass flow rate for small crack opening and viscous flow controls the mass flow rate for large crack opening and high temperature (i.e., high pressure). At a lithium temperature of 1400°C (saturation pressure = 0.15 MPa) and for initial crack width of 10 μm, the mass flow rate is 4×10^{-4} g/s. Calculated variation of lithium vapor velocity with lithium temperature is plotted in Figure 5.3-9(a) for various values of initial crack opening. Note that the maximum vapor velocity at 1400 °C (saturation pressure = 0.15 MPa) is 40 m/s for a crack that is initially open by 10 μm. Thus, the assumption of incompressibility is justified up to an initial crack width of 10 μm. Compressibility and inertia effects may become important if initial crack width is significantly greater than 10 μm. For a first wall area = 500 m^2, a mass flow rate of 4×10^{-4} g/s distributed uniformly on the first wall corresponds to 10^{17} Li atoms/m^2/s per crack. Figure 5.3-9(b) shows the variation of the mean molecular flow velocity, which is independent of pressure and crack opening, as a function of temperature. As expected, these velocities are much higher than the viscous flow velocities and follow the sonic velocities in lithium vapor closely.

5.3.5. Permissible Lithium Leakage Rate

Leakage of lithium through the first wall may adversely impact the performance of EVOLVE in two ways. First, by draining the coolant locally from the cracked region, the first wall near the crack may be heated to unacceptably high temperature. Second, lithium atoms evaporating into the plasma chamber will diffuse into the core of the plasma and may lead to unacceptable level of impurity ions in the plasma.

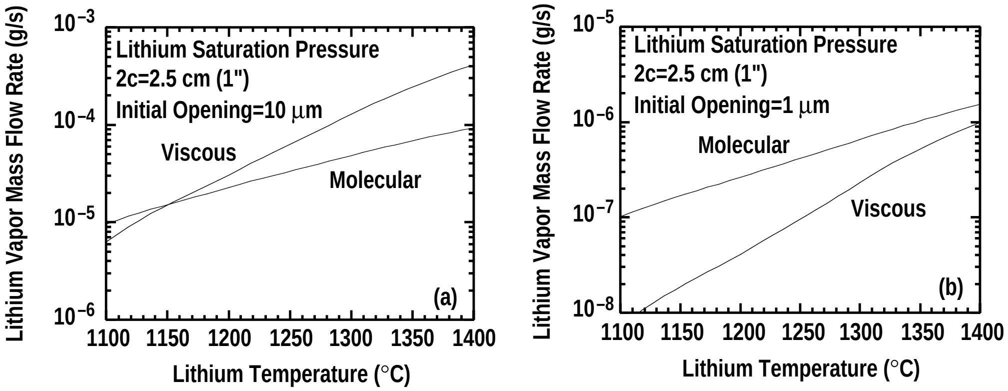

Figure 5.3-8. Variation of viscous and molecular leakage rates with lithium temperature for a 25 mm long crack in the EVOLVE first wall for initial crack opening of (a) 10 μm and (b) 1 μm.

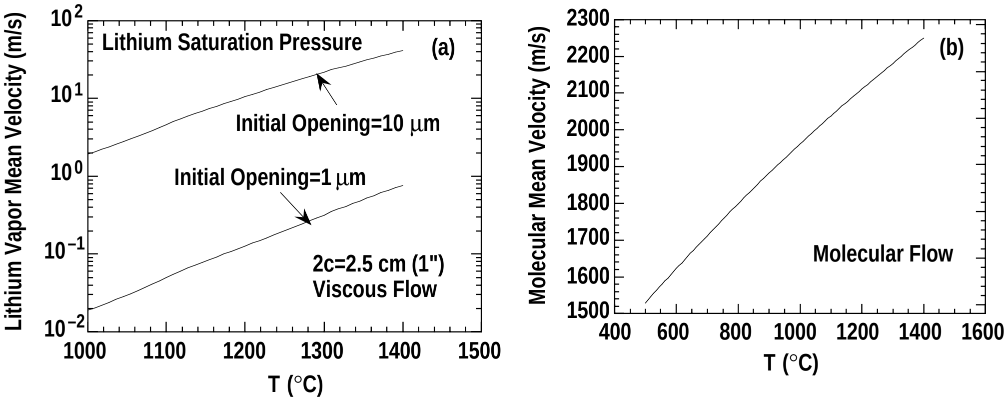

Figure 5.3-9. Variation of calculated lithium vapor velocity with temperature (a) by incompressible viscous flow theory and (b) molecular flow theory for various initial crack widths of a 25 mm long crack in the EVOLVE first wall.

5.3.5.1. <u>Impact on first wall cooling</u>

Coolant mass flow rate (M) required for cooling the first wall length containing a crack may be estimated as follows

$$M = \frac{2qdc}{h} \tag{5.3-17}$$

where q = surface heat flux, d = tube diameter, 2c = crack length, and h = heat of vaporization of lithium. At a surface heat flux of 2 MW/m^2, the minimum coolant mass flow required to cool a 2.5 cm long segment of the tube is 0.15 g/s, which is large compared to the estimated leakage rate of 5×10^{-4} g/s. Thus, 30 such cracks can be tolerated without impacting the cooling of the first wall locally.

5.3.5.2. <u>Impact on plasma contamination</u>

Acceptable core impurity level is determined by fuel dilution and radiation; for impurities with low Z, fuel dilution is the dominant constraint [5,6]. Taking a 20% power reduction to define the limit and assuming an average core hydrogen density of 1×10^{20} m^{-3}, Rognlien and

Rensink [5] have estimated an allowable Li edge density of 3×10^{18} m^{-3}. Using numerical 2-D transport simulations, they have calculated the corresponding allowable impurity Li vapor flux to be 2×10^{20} atoms $m^{-2}\,s^{-1}$ for a low-recycling hydrogen case and 3×10^{18} atoms $m^{-2}\,s^{-1}$ for a high-recycling hydrogen case. Both impurity fluxes are large compared to the 10^{17} Li $m^{-2}\,s^{-1}$ calculated for a single 2.5 cm long crack. Thus, 30 to 2000 such cracks, depending on hydrogen recycling, can be tolerated without impacting plasma performance.

5.3.6. Conclusions from Leakage Analysis

Of all the cases analyzed, lithium vaporizing at entrance to crack is probably closest to reality, which is, of course, much more complex. Heat of vaporization of lithium should not limit the leakage rate because it does not have to be supplied by the surface heat flux alone and can be supplied by the coolant and the first wall in the immediate vicinity of the crack.

The lithium vapor flow through a 2.5 cm long crack should be viscous at temperatures >1300°C. Between 1200 and 1300°C, combined viscous and molecular flow (transition flow) may occur.

Based on this model the maximum Li mass flow rate through a 2.5 cm long crack at the expected maximum pressure of 0.15 MPa is 5×10^{-4} g/s. Leakage rate will be even smaller if tortuosity of a real fatigue crack is included in the analysis. Total leakage rate from 30 such cracks represents 10% of the 0.15 g/s coolant flow needed for first wall cooling for a tube segment of 2.5 cm long. For a first wall area = 500 m^2, 5×10^{-4} g/s corresponds to 10^{17} Li atoms $m^{-2}\,s^{-1}$. Since the allowable leakage rate from a plasma contamination viewpoint varies between 3×10^{18} and 2×10^{20} Li atoms $m^{-2}\,s^{-1}$, 30 to 2000 such cracks (i.e., 0.06 to 4 cracks m^{-2} of first wall area) can be tolerated, depending on the behavior of hydrogen recycling.

References

[1] A. Zahoor, *Ductile Fracture Handbook*, E.P.R.I., Palo Alto, 1989.
[2] L. Bühler, "MHD Flows in Thick-walled Ducts", FZKA 6066, (I don't have the year, Malang might know since he sent me the reference)
[3] Saul Dushman, *Scientific Foundations of Vacuum Technique*, Second Edition, J.M. Lafferty, Editor, John Wiley & Sons, Inc., New York (1962).
[4] R.H. Jones, R.W. Conn, and R.F Schafer, "Effect of First Wall Flaws on Reactor Performance," Nuclear Engineering and Design/Fusion, Vol. 2, pp. 175-188 (1985).
[5] T.D. Rognlien and M.E. Rensink, "Interactions between Liquid-wall Vapor and Edge Plasmas," Presented at the 14th International Conference on Plasma Surface Interactions in Controlled Fusion Devices, Rosenheim, Germany, May 22-26, 2000.
[6] R.W. Moir, M. Rensink, and T.D. Rognlien, "Edge Plasma Analysis for Liquid-Wall MFE Concepts," Presented at the 18th IAEA Fusion Energy Conference, Sorrento, Italy, October 4-10, 2000.

Acknowledgment

Helpful discussions with S. Malang, L. Barleone, T.D. Rognlien, and R. Moir are gratefully acknowledged. Thanks are also due to S. Zinkle for providing the material properties data.

Appendix 5.A

Thermal Analysis. Consider a section of the EVOLVE first wall tube of inner radius r_i and outer radius r_o, as shown in Figure 5.2-1(a), subjected to a cosinusoidally varying surface heat flux Q Cos θ. It is cooled internally by evaporation of lithium at a temperature T_c. It is assumed that there is a constant heat transfer coefficient h_f between the coolant and the first wall ID surface. If temperature-dependence of thermal conductivity of the first wall is ignored, the steady-state temperature field in the first wall satisfies Laplace's equation, and a solution for the temperature field can be taken as follows:

$$T(r,\theta) = \begin{cases} T_c + \sum_{n=1}^{\infty} a_n \left(\frac{r}{r_i}\right)^n \mathrm{Cos}\, n\theta + \sum_{n=1}^{\infty} b_n \left(\frac{r_i}{r}\right)^n \mathrm{Cos}\, n\theta \text{ for } |\theta| \le \frac{\pi}{2} \\ T_c \text{ for } \pi > |\theta| > \frac{\pi}{2} \end{cases}. \tag{5A-1}$$

After satisfying the following boundary conditions,

$$\kappa \left.\frac{\partial T}{\partial r}\right|_{r=r_o} = Q\,\mathrm{Cos}\,\theta \tag{5A-2a}$$

and

$$\kappa \left.\frac{\partial T}{\partial r}\right|_{r=r_i} = h_f \left(T|_{r=r_i} - T_c \right) \tag{5A-2b}$$

where κ is thermal conductivity, the solution for temperature T is as follows:

$$T(r,\theta) = \begin{cases} T_c + \frac{Q\, r\, \mathrm{Cos}\,\theta}{\kappa} + \left\{ \frac{r}{r_i}\left(\frac{r_i}{r_o}\right)^2 + \frac{r_i}{r} \right\} b_1\, \mathrm{Cos}\,\theta \text{ for } |\theta| \le \frac{\pi}{2} \\ T_c \text{ for } \pi > |\theta| > \frac{\pi}{2} \end{cases} \tag{5A-3a}$$

where

$$b_1 = -\frac{Q r_i}{\kappa} \frac{1 - \frac{\kappa}{h_f r_i}}{1 + \left(\frac{r_i}{r_o}\right)^2 + \frac{\kappa}{h_f r_i}\left\{1 - \left(\frac{r_i}{r_o}\right)^2\right\}}. \tag{5A-3b}$$

The maximum first wall temperature T_{max}, which occurs at $r = r_o$ and $\theta = 0$, is given by

$$T_{max} = T_c + \frac{Q r_o}{\kappa} + \frac{2 b_1 r_i}{r_o}, \tag{5A-4a}$$

and the section-averaged temperature T_{avg} is given by

$$T_{avg} = T_c + \frac{\frac{Qr_o}{3\kappa}\left[1-\left(\frac{r_i}{r_o}\right)^3\right] + \frac{b_1 r_i}{3r_o}\left[1-\left(\frac{r_i}{r_o}\right)^3 + 3\left(1-\frac{r_i}{r_o}\right)\right]}{\frac{\pi}{2}\left[1-\left(\frac{r_i}{r_o}\right)^2\right]} \quad \text{(5A-4b)}$$

Fracture Mechanics Analysis. Consider an elliptical axial surface flaw of axial length (2c) and depth (a) at the plasma edge ($\theta = 0$) of the o.d. surface [Figure 5.2-1(b)]. The crack is subjected to remote membrane (σ_m) and bending (σ_b) stresses whose magnitudes are given in Eqs (6a) and (6b), respectively. The axial crack driving force (stress intensity factor range) is given by J.C. Newman, Jr. and I. S. Raju [1].

$$\Delta K_c = \left(\sigma_m + H_1\sigma_b\right)\sqrt{\frac{\pi a}{D}}F_1\sqrt{\frac{a}{c}}\sqrt[4]{\frac{a}{h}}g_1 \quad \text{(5A-5a)}$$

and the through-thickness crack driving force (stress intensity factor range) is given by

$$\Delta K_a = \left(\sigma_m + H_2\sigma_b\right)\sqrt{\frac{\pi a}{D}}F_1\sqrt[4]{\frac{a}{h}} \quad \text{(5A-5b)}$$

where

$$H_1 = 1 - 0.34\frac{a}{h} - 0.11\frac{a}{c}\frac{a}{h} \quad \text{(5A-5c)}$$

$$H_2 = 1 + G_1\frac{a}{h} + G_2\left(\frac{a}{h}\right)^2 \quad \text{(5A-5d)}$$

$$G_1 = -1.22 - 0.12\frac{a}{c} \quad \text{(5A-5e)}$$

$$G_2 = 0.55 - 1.05\left(\frac{a}{c}\right)^{0.75} + 0.47\left(\frac{a}{c}\right)^{1.5} \quad \text{(5A-5f)}$$

$$D = 1 + 1.464\left(\frac{a}{c}\right)^{1.65} \quad \text{for} \quad \frac{a}{c} \le 1 \quad \text{(5A-5g)}$$

$$F_1 = M_1 + M_2\left(\frac{a}{h}\right)^2 + M_3\left(\frac{a}{h}\right)^4 \quad \text{(5A-5h)}$$

$$M_1 = 1.13 - 0.09\frac{a}{c} \quad \text{(5A-5I)}$$

$$M_2 = -0.54 + \frac{0.89}{0.2 + \frac{a}{c}} \quad \text{(5A-5j)}$$

$$M_3 = 0.5 - \frac{1.0}{0.65 + \frac{a}{c}} + 14\left(1.0 - \frac{a}{c}\right)^{24} \tag{5A-5k}$$

$$g_1 = 1.1 + 0.35\left(\frac{a}{h}\right)^{2} \tag{5A-5l}$$

Reference

[1] J.C. Newman, Jr. and I.S. Raju, Eng. Fract. Mech. Vol.15 (1981).

6. Nuclear Performance Characteristics

6.1. Introduction

The blanket consists of a number of trays, stacked poloidally, containing liquid lithium. Each tray contains a lithium pool with a height ranging from 19 cm at the front to 16 cm at the back, which is maintained by a system of overflow tubes. The radial thickness of the trays in the outboard (OB) region is 50 cm while the thickness in the inboard (IB) region is 40 cm. The lithium in the trays is allowed to boil and the vapor is routed through the space between trays to a vertical vapor manifold. An alternate blanket design approach is an extension of the first wall (FW) transpiration-cooling concept. There is no lithium boiling or bubble formation with this approach. The lithium is confined to thin slab zones surrounded by 0.5 mm thick walls with capillary openings. Lithium vapor flows in channels between the liquid lithium slabs.

Since the lithium density in the FW and primary breeding blanket is low and the trays do not fully cover the FW area, a 40 cm thick secondary breeding blanket is utilized in the OB region to enhance tritium breeding and to improve neutron shielding. The neutron flux in the secondary breeding zone is considerably lower than at the front blanket, allowing the use of a variety of blanket concepts. However, a self-cooled lithium/tungsten blanket (90% Li, 10% W-5Re) concept has been selected in order to limit the number of materials used and to also allow high temperature operation in this zone. Both the IB and OB high temperature shields required for additional shielding of the vacuum vessel (VV) and magnets are also made of W-5Re as structural material and cooled by flowing lithium. Tungsten carbide is used as a shielding material. The composition of shield is 20% Li, 10% W-5Re, and 70% WC. The OB and IB shield thicknesses are 50 and 60 cm, respectively. The VV thickness is 30 cm. It consists of two steel sheets each 5 cm thick sandwiching a 20 cm thick shielding zone made of 80% WC with 20% He coolant.

The neutronics performance of the EVOLVE concept was analyzed using two-dimensional calculations. Lithium tray boiling analysis is underway for the EVOLVE boiling blanket design to determine the vapor fraction distribution. This is expected to impact the nuclear performance parameters. In a previous work, the nuclear performance parameters were determined assuming a uniform vapor fraction of 17% in the trays [1]. Initial results obtained using a standard drift-flux model and considering the churn-turbulent boiling regime that does not include MHD effects show a large vapor fraction of up to 65%. On the other hand, a flow pattern with triggered vapor channels has been analyzed. Results obtained by applying balances for forces, mass, and energy including static, dynamic, friction, and MHD pressure terms indicate that the void fraction could be in the range of 6%–12%, as presented in Chapter 4. We assessed the impact of the lithium vapor fraction in the trays on the nuclear performance parameters of the EVOLVE concept. The design analysis for the transpiration blanket is presented in Chapter 3. The estimated radial build and material composition for that blanket option were used to compare the expected nuclear parameters with those for the boiling blanket design.

An update of the activation analysis was also performed for the EVOLVE concept using the two-dimensional model. The analysis used the W-La_2O_3 alloy as a structure material in the first wall and blanket. In order to enhance the safety characteristics of the design, the W-La_2O_3 alloy was selected to replace the W-5Re alloy, which was used in the previous analysis. The idea is that removing the 5% Re included in the W-5Re alloy might improve the overall EVOLVE safety features. Activation results obtained for the two tungsten alloys were compared.

Reference

[1] M.A. Abdou et al., “On the Exploration of Innovative Concepts for Fusion Chamber Technology- APEX Interim Report,” UCLA-ENG-99-206, November (1999).

6.2. Neutronics Calculational Model

Two-dimensional (2-D) modeling of the front evaporation-cooled blanket of EVOLVE is needed to properly account for the poloidal heterogeneity and gaps between the trays. In addition, 2-D modeling is required to determine the detailed distribution of nuclear heat deposition in the boiling blanket which is an important input for the lithium boiling analysis. The R-Z geometrical 2-D model used in the calculation is shown in Figure 6.2-1. It includes the FW, trays with lithium vapor manifold, secondary breeding blanket, shield, VV, and magnet in both the IB and OB regions. Both the IB and OB regions are modeled simultaneously to account for the toroidal effects. Due to the limitations of 2-D modeling, the trays are assumed to have a uniform height of 17.5 cm. In addition, the detailed FW tube configuration is not modeled and the FW is represented by a single 0.6 cm thick plate. These design details require 3-D modeling and are not expected to affect the neutronics results. The TWODANT module of the DANTSYS 3.0 discrete ordinates particle transport code system was utilized in the calculations [1]. An inherent problem associated with multi-dimensional discrete ordinates calculations is referred to as the “ray effect”. It is related to the fact that the angular flux is given only in certain discrete directions which could lead to underestimating neutron streaming. This effect is mitigated by using the ray tracing first collision source option in TWODANT.

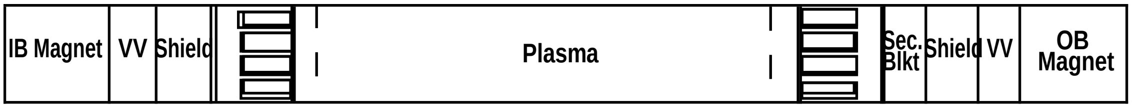

Figure 6.2-1. R-Z two-dimensional model for EVOLVE.

Reference

[1] R.E. Alcouffe et al., “DANTSYS 3.0, One-, Two-, and Three-Dimensional Multigroup Discrete Ordinates Transport Code System,” RSICC Computer Code Collection CCC-547, Contributed by Los Alamos National Lab, August 1995.

6.3. Nuclear Heating in Boiling Blanket

The nuclear heating calculation was iterated with the lithium tray boiling analysis to determine a nuclear heating distribution that is consistent with the vapor fraction distribution. The lithium pool was divided into 25 zones (5 radial × 5 vertical). The tray bottom and back W plates are 0.5 cm thick. The results were normalized to an OB peak neutron wall loading of 10 MW/m^2. The distribution of nuclear heating in the OB tray was generated using an initial uniform vapor fraction of 17%. The results given in Figure 6.3-1 were used as input to the lithium boiling calculations with a drift-flux model, which neglects the impact of magnetic field, to produce a new vapor fraction distribution. Subsequently this vapor fraction distribution was used to modify the lithium density distribution in the 2-D model. A new set of nuclear heating values was obtained from the neutronics calculations. The iteration process continued with results converging after three iterations yielding a consistent set of vapor fraction and nuclear heating distributions given in Figures 6.3-2 and 6.3-3. Starting from 17% uniform vapor fraction, the average vapor fraction values after the first, second, and third iterations are 52.4%, 55.6%, and 55.5%, respectively. Comparing the results in Figsures 6.3-1 and 6.3-3, one notices that the higher vapor fractions result in higher heating in the tray structure, less heating in the Li pool, and more uniform radial variation of heating. Figures 6.3-4 and 6.3-5 give the vertical and radial distributions of nuclear heating in the Li pool obtained from the subsequent iterations.

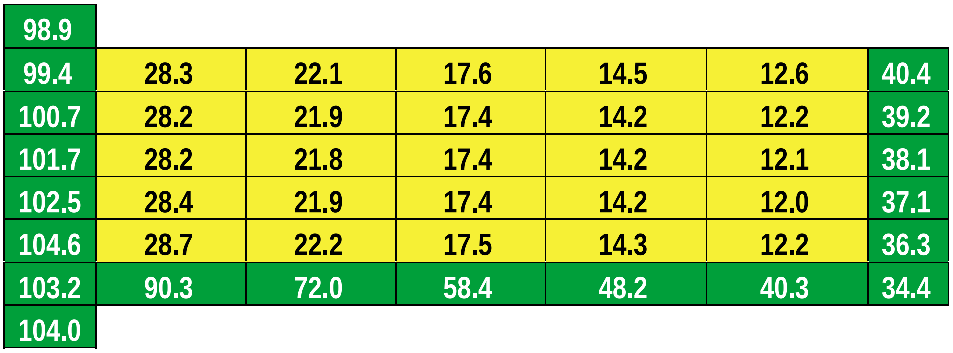

98.9						
99.4	28.3	22.1	17.6	14.5	12.6	40.4
100.7	28.2	21.9	17.4	14.2	12.2	39.2
101.7	28.2	21.8	17.4	14.2	12.1	38.1
102.5	28.4	21.9	17.4	14.2	12.0	37.1
104.6	28.7	22.2	17.5	14.3	12.2	36.3
103.2	90.3	72.0	58.4	48.2	40.3	34.4
104.0						

Figure 6.3-1. Initial nuclear heating (W/cm^3) distribution based on uniform 17%.vapor fraction.

	65.2	64.2	63.6	63.1	63.4	
	64.6	63.4	62.8	62.1	62.5	
	63.6	62.4	61.6	60.8	61.0	
	62.1	60.6	59.5	58.5	58.5	
	30.5	29.7	29.1	28.5	28.4	

Figure 6.3-2. Vapor fraction (%) distribution in OB tray.

104.4						
104.5	13.5	11.9	10.4	9.3	8.4	56.7
105.5	13.7	12.1	10.6	9.5	8.5	55.8
106.4	14.1	12.3	10.9	9.8	8.8	54.8
107.2	14.6	12.6	11.5	10.3	9.3	53.8
109.0	27.0	23.1	20.0	17.7	16.0	52.7
109.0	98.0	84.2	72.9	64.1	56.8	50.5
110.0						

Figure 6.3-3. Nuclear heating (W/cm^3) distribution in OB tray.

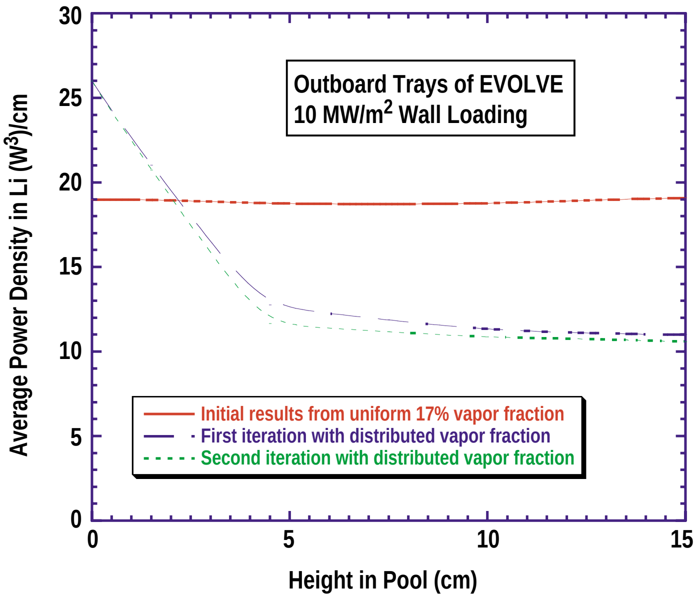

Figure 6.3-4. Vertical variation of nuclear heating in the Li pool obtained from the subsequent iterations.

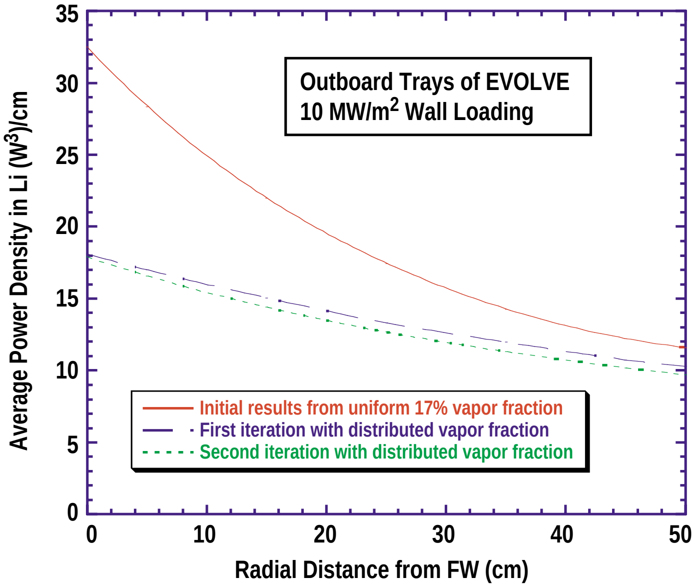

Figure 6.3-5. Radial variation of nuclear heating in the Li pool obtained from the subsequent iterations.

6.4. Impact of Vapor Fraction in Boiling Blanket on Nuclear Parameters

The lithium tray boiling analysis using the drift-flux model without MHD effects indicates that high vapor fractions up to 65% might exist in the lithium pool. This is much higher than the 17% average value assumed in previous neutronics calculations. In these calculations, the overall tritium breeding ratio (TBR) was determined to be 1.37 at a lithium enrichment of 40% ^{6}Li with no breeding assumed in the divertor region [1]. Higher vapor fractions lead to lower densities in the tray resulting in lower TBR and reduced shielding effectiveness. In addition, the lithium pools with higher vapor fractions are more transparent for neutrons, resulting in a smaller fraction of nuclear heating carried as high-grade heat by the lithium vapor generated in the trays.

Several one-dimensional (1-D) scoping calculations were performed for poloidal sections going through the trays to assess the impact of the vapor fraction on the nuclear performance parameters. Figure 6.4-1 shows the impact of varying the vapor fraction in the lithium pool on the TBR. The drop in local TBR at poloidal locations where the trays are located is only ~4% when the vapor fraction is increased from 17% to 60%. More neutrons go through the front of the tray producing more breeding at the back of the tray, secondary blanket, and shield resulting in a relatively small drop in TBR. In other words, while the vapor fraction affects the radial distribution of tritium breeding, it has minimal effect on total TBR. Notice that if a vapor fraction <8% can be achieved with triggered vapor channels, the TBR will increase by <1% compared to the 17% vapor fraction case.

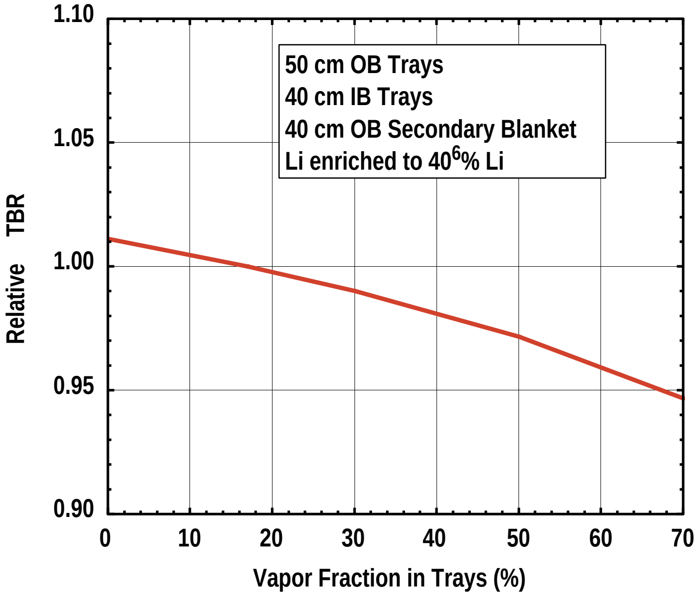

Figure 6.4-1. Impact of void fraction on tritium breeding.

The results for sections through and between trays were combined to determine the fraction of energy carried by the vapor. With 60% vapor fraction in the lithium pool, ~54% of the total energy is carried by the Li vapor compared to 66% obtained using the same analysis with 17% vapor fraction. The impact on the power conversion efficiency remains to be determined. The peak damage (dpa and He production) in the structural material behind the trays is increased by a factor of 1.78. This is not a concern since enough margins existed for these parameters (peak dpa rate in back manifold plate was 7 dpa/FPY and peak end-of-life He in VV was 0.3 appm with 17% vapor fraction) [1]. The peak fast neutron fluence and insulator dose in the magnet increase by a factor of 1.77. To keep magnet radiation effects at the same level we need to increase the radial build of the shield by about 4 cm. However, this is not needed since magnet radiation effects are still much lower than the design limits. It is concluded that the higher vapor fraction in the lithium trays predicted with the conservative boiling analysis will have minimal impact on the nuclear performance parameters.

Reference

[1] M.E. Sawan and S. Malang, "Neutronics Features of a High Power Density First Wall/Blanket with Lithium Evaporation Cooling," Proc. 5th Symposium on Fusion Nuclear Technology, Rome, 1999 (to be published in Fusion Engineering & Design).

6.5. Two-Dimensional Neutronics Results with Detailed Vapor Fraction Distribution

The analysis given in the previous section is based on 1-D calculations at poloidal locations through the trays with uniform vapor fractions. The iterated process between the 2-D neutronics calculations and the lithium tray boiling analysis with the drift-flux model resulted in a detailed vapor fraction profile in the boiling lithium blanket. 2-D calculations have been performed using this vapor fraction profile to determine the nuclear performance parameters and compare them to those obtained from the previous 2-D calculations with uniform 17% vapor fraction.

The overall TBR is 1.33 based on the conservative assumption of no breeding in the divertor region. The contribution from each component is illustrated in Figure 6.5-1. 61.5% of tritium breeding occurs in the FW and primary breeding blanket (54.9% OB and 15.6% IB). The OB secondary blanket contributes 35.2% of the total overall TBR. The contribution of the shield is only 3.3% (1.2% OB and 2.1% IB). It is clear that tritium breeding has a comfortable margin that allows for design flexibility. Comparing these results to the results of the previous 2-D calculations with 17% vapor fraction, one notices that while the overall TBR is lower by only 3%, more breeding is contributed by the secondary blanket and shield due to the lower attenuation of neutrons in the lithium pool.

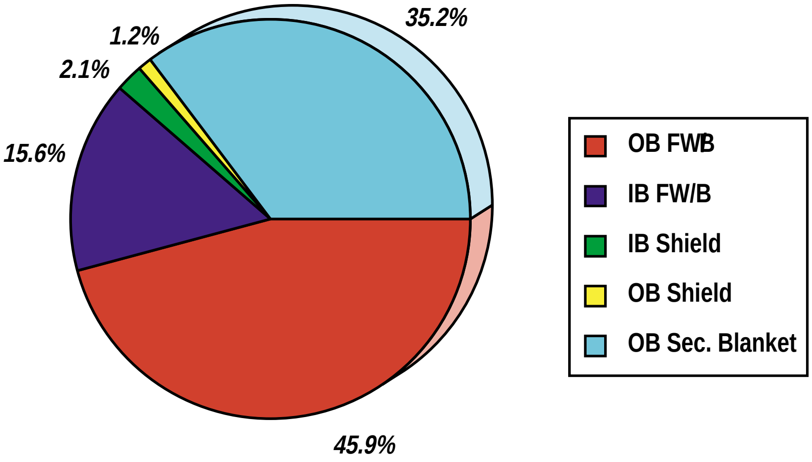

Figure 6.5-1. Overall TBR with contributions from different components.

Nuclear heating in the blanket and shield components was calculated using the 2-D model. The nuclear energy multiplication, M_n, defined as the amount of nuclear heating per unit neutron energy incident on the FW, is 1.195. This is only 0.3% lower than that with 17% vapor fraction. Nuclear heating partitioning is shown in Figure 6.5-2. The results indicate that 65.3% of the nuclear heating is deposited in the evaporation cooled primary blanket. Adding the surface heat deposited in the FW implies that ~70% of the total IB and OB energy is deposited as high-grade heat in the front evaporation cooled zone and is carried by the lithium vapor to the heat exchanger. This is slightly lower than the 76% fraction calculated for the 17% vapor fraction case.

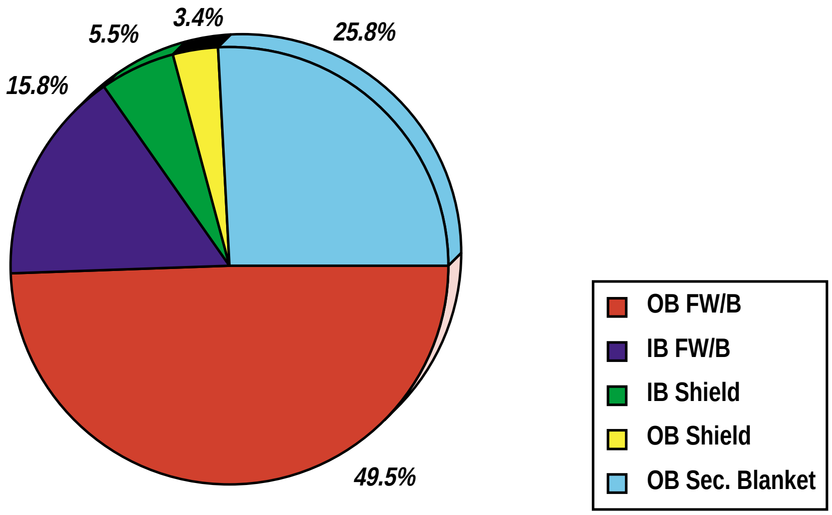

Figure 6.5-2. Nuclear heating partitioning in different components.

The peak dpa and helium production rates have been determined in the W-5Re structure using the 2-D model. Table 6.5-1 gives the results. Figure 6.5-3 shows the poloidal variation of the dpa rate in the W structure around an OB tray. The results are given for the FW, front of secondary blanket, and front of shield. No significant poloidal peaking is observed. Since the source is volumetrically distributed and the poloidal gap between trays is only 1 cm (5% of FW area), the FW and trays intercept most of the source neutrons. The secondary neutrons which give large contributions to radiation damage tend to give nearly poloidally uniform profiles. The peak damage rate in the OB secondary blanket and IB shield is about a factor of ~5 lower than in the FW and, hence, they are expected to have a factor of 5 longer lifetime than the FW and trays. The lifetime of the OB shield is about an order of magnitude longer than for the OB secondary blanket and the IB shield, making it a lifetime component.

Table 6.5-1. Peak dpa and He Production Rates in the W Structure

	dpa/FPY		He appm/FPY	
	IB	OB	IB	OB
FW	25.7	34.2	13.8	19.7
Manifold Backplate	8.6	8.9	2.6	2.7
Secondary Blanket	NA	7.7	NA	2.4
Shield	5.3	0.94	1.55	0.15

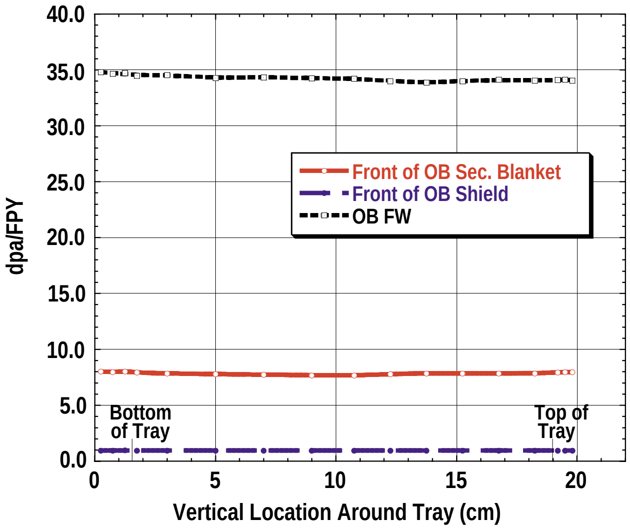

Figure 6.5-3. Poloidal variation of structure damage around tray.

Table 6.5-2 gives the peak neutronics parameters for the VV. The peak end-of-life He production values in the VV after 30 FPY of plant operation are 0.44 and 0.27 appm on the IB and OB sides, respectively. These values are less than the 1 appm required for reweldability [1]. Table 6.5-3 gives the peak nuclear parameters in the magnet. In this study we adopted the magnet radiation limits used in ARIES-RS [2]. It is clear that all magnet radiation limits are satisfied with a large margin.

Table 6.5-2. Peak VV Neutronics Parameters

	IB	OB
Peak Nuclear Heating (mW/cm^3)	3.5	2.5
Peak end-of-life dpa	0.10	0.07
Peak end-of-life He appm	0.44	0.27

Table 6.5-3. Peak Magnet Neutronics Parameters

	IB	OB	Design Limit
Peak Nuclear Heating (mW/cm^3)	0.15	0.10	2
Peak end-of-life Fast Neutron Fluence (n/cm^2)	4×10^{18}	2.7×10^{18}	10^{19}
Peak end-of-life Dose to Insulator (Rads)	4.3×10^{9}	2.7×10^{9}	10^{11}
Peak end-of-life dpa to Cu Stabilizer	1.9×10^{-3}	1.2×10^{-3}	6×10^{-3}

Figure 6.5-4 shows the nuclear parameters relative to the values obtained using 17% vapor fraction. It is clear that the impact of the high void fraction is small. Notice that even though the 2-D neutronics calculations presented here are for the worst case conditions, all nuclear performance parameters are acceptable with a comfortable margin. Therefore, the EVOLVE boiling blanket is expected to perform adequately from the neutronics point of view for any of the boiling regimes considered.

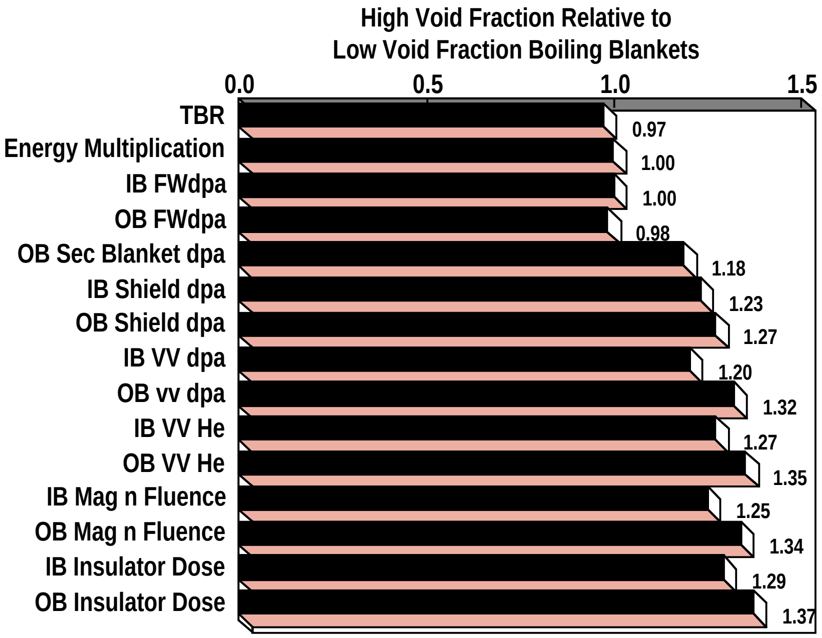

Figure 6.5-4. Nuclear parameters compared to the 17% vapor fraction case.

References

[1] Technical Basis for the ITER Final Design Report, Cost Review and Safety Analysis, ITER EDA Documentation Series, International Atomic Energy Agency, Vienna, December 1997.

[2] L.A. El-Guebaly, "Nuclear Issues and Analysis for ARIES Spherical and Advanced Tokamaks," Fusion Engineering & Design **51-52**, 325 (2000).

6.6. Comparison between Nuclear Parameters for Transpiration and Boiling Blankets

The preliminary radial build and material composition for the transpiration blanket was used to compare the nuclear parameters for the EVOLVE boiling and transpiration design options. One should keep in mind that the relative results depend on the assumptions made for material composition. The overall material fractions used in the FW/primary blanket are given in Table 6.6-1. It is clear that with these assumptions, the boiling blanket is more transparent for neutrons and gamma photons.

Figure 6.6-1 shows the nuclear parameters for the transpiration blanket relative to those obtained with the boiling blanket. Slightly higher TBR and energy multiplication result from using the transpiration blanket due to the lower vapor fraction and larger content of Li and W. Neutron multiplication in the larger amount of W contributes also to the larger TBR. A larger fraction of thermal power of ~80% is removed as high-grade heat by the Li vapor in the transpiration design. More neutrons and gamma photons penetrating the more transparent boiling blanket result in generating more nuclear heating in the liquid Li-cooled secondary blanket and shield.

Table 6.6-1. Overall Material Fractions in FW and Primary Blanket

	Inboard		Outboard	
	Boiling	Transpiration	Boiling	Transpiration
Thickness (cm)	42.6	42.85	52.6	60.3
% Li	43.4	80.5	43.6	83
% W	2.6	6.7	2.1	6.7
% Void	54	12.8	54.3	10.3

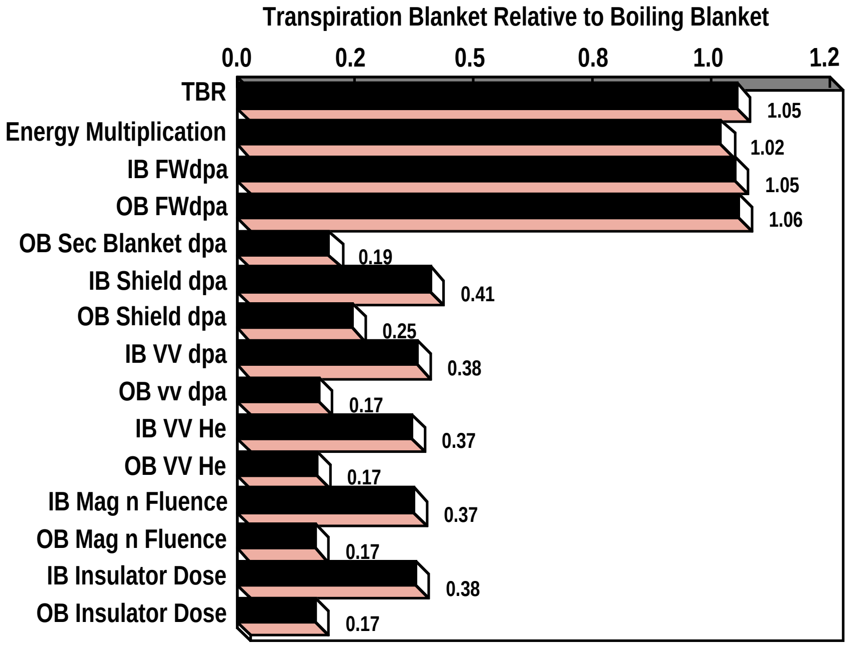

Figure 6.6-1. Nuclear parameters with transpiration blanket relative to boiling blanket.

Higher nuclear heating and damage occur in the FW of the transpiration design due to the larger reflection from the more dense transpiration blanket. On the other hand, the nuclear heating and damage values in the OB components behind the transpiration blanket are a factor of 4-6 lower than for the boiling design due to the thicker and more dense transpiration blanket. Nuclear heating and damage values in the IB components behind the transpiration blanket are a factor of 2-3 lower than for the boiling design due to the more dense transpiration blanket. Neutronics results for the boiling blanket with widely varying vapor fractions (Figure 6.5-4) imply that the shielding impact of void fraction is much smaller than the differences between the transpiration and boiling blankets given in Figure 6.6-1. It is therefore concluded that the larger difference in shielding effectiveness between the transpiration and boiling blankets is attributed primarily to the larger structure content used in the transpiration blanket. Based on these results, the shield radial build in the transpiration design can be reduced by ~10 cm in the OB side and ~5 cm in the IB region compared to the boiling blanket design.

We recognize that the volume fractions of these two approaches could vary with more design details. However, the results show that the nuclear performance parameters for both designs are acceptable with a large margin implying that the choice between these two options should not be driven by differences in the nuclear performance.

6.7. Activation Calculations

An update of the activation analysis was performed. Calculations were performed assuming neutron wall loadings of 7 and 10 MW/m^2 at the IB and OB first walls, respectively. The analysis used the W-La$_2$O$_3$ alloy as a structure material in the first wall and blanket. In order to enhance the safety characteristics of the design, the W-La$_2$O$_3$ alloy was selected to replace the W-5Re alloy, which was used in the previous analysis. The idea is that removing the 5% Re includes in the W-5Re alloy may improve the overall EVOLVE safety features.

The elemental compositions of the W-Re and W-La$_2$O$_3$ alloys are shown in Table 6.7-1. These compositions are based on those used in ITER for W and W-La$_2$O$_3$ [1]. In this section the term “first wall” refers to the first wall and tray as a single unit. The WC was used as a shielding material. Based on dpa limits for tungsten, the IB and OB first walls were assumed to be replaced every 5 FPY. On the other hand, the OB blanket, shield and VV are assumed to stay in place for 30 FPY. Two-dimensional calculations are needed to take in to account the neutron streaming through the gaps between the trays. The 2-D model used in the neutronics calculations was used.

The neutron flux obtained from the neutron transport calculations was used in the activation calculations. The activation analysis was performed using the activation code DKR-PULSAR2.0 [2]. The code combined the neutron flux with the FENDL/A-2.0 data library [3] to calculate the activity and decay heat as a function of time following shutdown. The calculated specific activities were used to determine the waste disposal ratings (WDR) of the different components at the end of their lifetime. The results of the decay heat analysis represent an important input used to evaluate the temperature variation exhibited by the structure during a loss of coolant accident (LOCA).

Table 6.7-1. Elemental Compositions of the W-5Re and W-La_2O_3 Alloys

Nuclide	W-5Re	W-La_2O_3
H	5 wppm	20 wppm
C	30 wppm	30 wppm
N	10 wppm	50 wppm
O	30 wppm	See La_2O_3
Na	10 wppm	20 wppm
Mg	5 wppm	10 wppm
Al	15 wppm	20 wppm
Si	20 wppm	20 wppm
P	50 wppm	---
S	5 wppm	10 wppm
K	10 wppm	10 wppm
Ca	10 wppm	20 wppm
Ti	10 wppm	20 wppm
Cr	10 wppm	30 wppm
Mn	5 wppm	5 wppm
Fe	30 wppm	50 wppm
Co	10 wppm	10 wppm
Ni	20 wppm	20 wppm
Cu	10 wppm	20 wppm
Zn	5 wppm	10 wppm
As	5 wppm	5 wppm
Zr	10 wppm	20 wppm
Nb	10 wppm	20 wppm
Mo	100 wppm	100 wppm
Ag	5 wppm	5 wppm
Cd	10 wppm	10 wppm
Ba	10 wppm	10 wppm
Ta	10 wppm	20 wppm
W	94.96%	98.84%
Re	5 %	---
Pb	10 wppm	10 wppm
La_2O_3	----	1.1%

References

[1] V. Barabash, Materials Group, ITER JCT, Private Communications, March (1997).

[2] J. Sisolak, et al., “DKR-PULSAR2.0: A Radioactivity Calculation Code that Includes Pulsed/Intermittent Operation,” to be published.

[3] A.Pashchenko et al., “FENDL/2.0:Neutron Activation Cross-Section Data Library for Fusion Applications,” Report INDC(NDS)-173, IAEA Nuclear Data Section, March (1997).

6.8. Activity and Decay Heat

In the case of the W-5Re alloy, the specific activity and decay heat values induced in the different components as a function of time following shutdown are shown in Figures 6.8-1 and 6.8-2, respectively. As shown in both figures, the W-5Re alloy produces high level of radioactivity after shutdown. The first wall and blanket dominate the overall activity and decay heat induced in the structure. Table 6.8-1 shows a list of nuclides that dominate the induced radioactivity in the different components for both alloys. As shown in the table, the tungsten isotopes ^{181}W($T_{1/2}$ = 121 day), ^{185}W($T_{1/2}$ = 75.1 day), and ^{184}Re($T_{1/2}$ = 38 day) are the main contributors to the induced radioactivity during the first few weeks following shutdown. Neutron interactions and subsequent decays of both tungsten and rhenium produce these isotopes. The long-term radioactivity is generated by the ^{179}Ta($T_{1/2}$ = 665 day), ^{182}Ta($T_{1/2}$ = 115 day), and ^{186m}Re($T_{1/2}$ = 2x10^5 yr) isotopes. Out of these three isotopes, ^{186m}Re is the most troublesome because it is considered as a major contributor to the waste disposal ratings at the end of the plant life-time. In addition, ^{186m}Re is also one of the main contributors to the off-site doses during an accident.

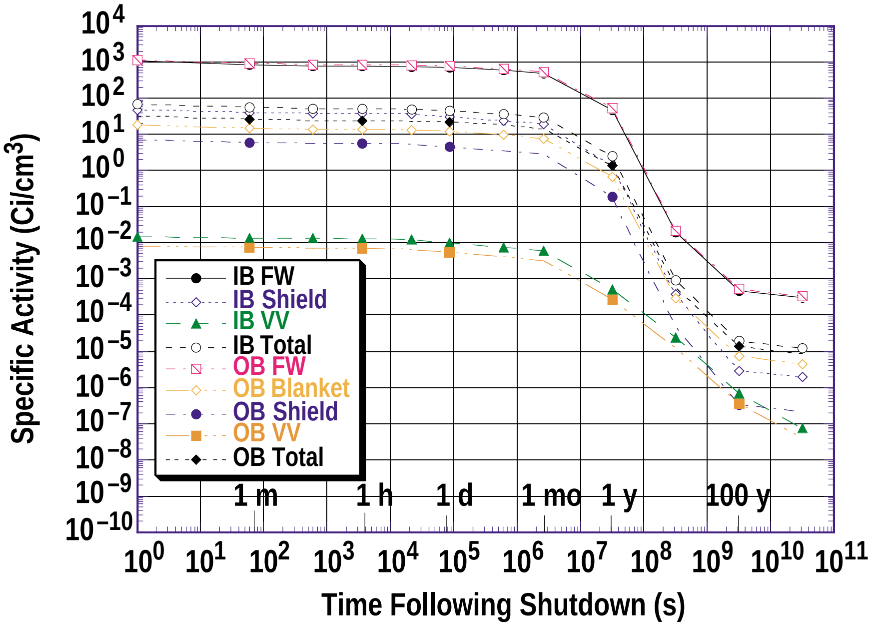

Figure 6.8-1. Activity induced in the different components of EVOLVE as a function of time following shutdown for the W-5Re alloy case.

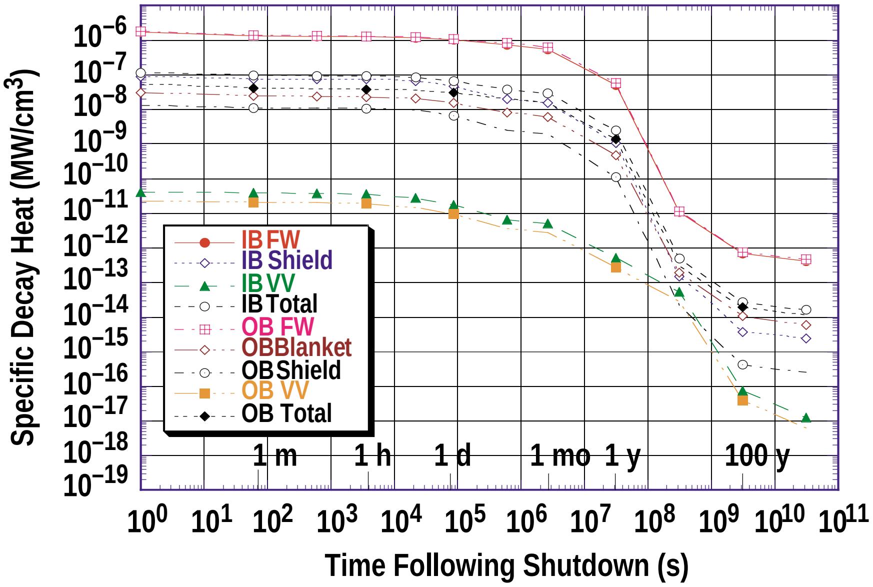

Figure 6.8-2. Decay heat induced in the different components of EVOLVE as a function of time following shutdown for the W-5Re alloy case.

Table 6.8-1. List of Dominant Nuclides

	Activity	Decay Heat
Short-term < 1 day	^{185}W, ^{181}W	^{184}Re, ^{185}W
Intermediate-term < 1 month	^{181}W, ^{185}W	^{184}Re, ^{185}W
Long-term > 1 year	^{179}Ta, ^{186m}Re	^{182}Ta, ^{186m}Re

Replacing the W-5Re alloy with the W-La$_2$O$_3$ alloy results in a small reduction in the level of radioactivity generated in the first wall. Figures 6.8-3 and 6.8-4 show a comparison between the specific activity and decay heat induced in the first wall of EVOLVE for the W-5Re and W-La$_2$O$_3$ alloys, respectively.

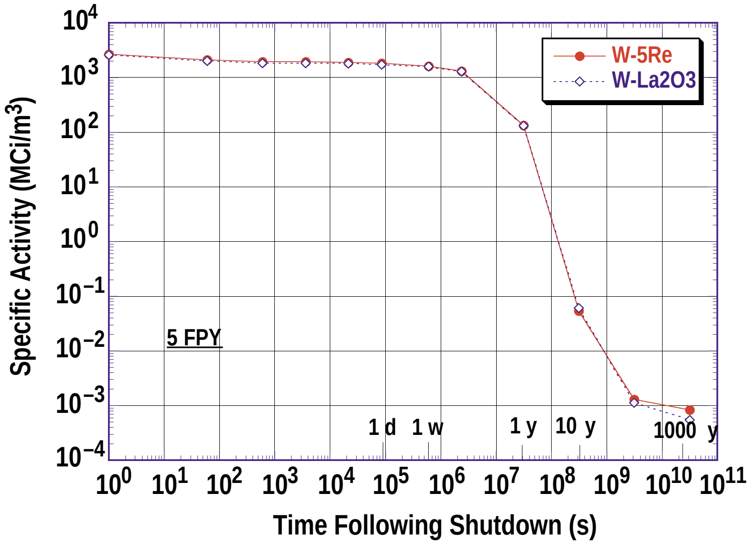

Figure 6.8-3. Comparison between the levels of specific activities induced in first wall.

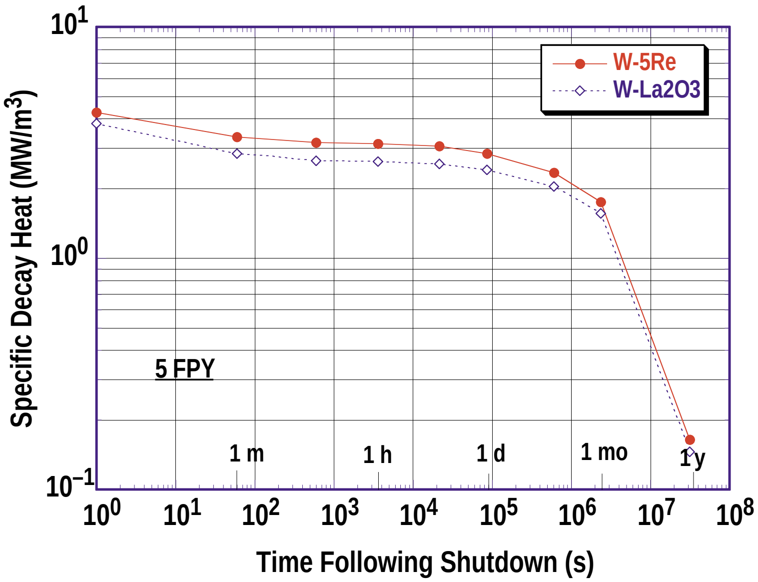

Figure 6.8-4. Comparison between the levels of specific decay heat induced in the first wall.

6.9. Waste Disposal Ratings

The radwaste of the different components of EVOLVE were evaluated according to both the NRC 10CFR61 [1] and Fetter [2] waste disposal concentration limits (WDL). The 10CFR61 regulations assume that the waste disposal site will be under administrative control for 100 years. The dose at the site to an inadvertent intruder after the 100 years is limited to less than 500 mrem/year. The waste disposal rating (WDR) is defined as the sum of the ratio of the concentration of a particular isotope to the maximum allowed concentration of that isotope taken over all isotopes and for a particular class.

If the calculated WDR ≤1 when Class A limits are used, the radwaste should qualify for Class A segregated waste. The major hazard of this class of waste is to individuals who are responsible for handling it. Such waste is not considered to be a hazard following the loss of institutional control of the disposal site. If the WDR is >1 when Class A WDL are used but ≤1 when Class C limits are used, the waste is termed Class C intruder waste. It must be packaged and buried such that it will not pose a hazard to an inadvertent intruder after the 100 years institutional period is over. Class C waste is assumed to be stable for 500 years. Using Class C limits, a WDR > 1 implies that the radwaste does not qualify for shallow land burial.

Fetter [2] developed a modified version of the NRC's intruder model to calculate waste disposal limits for a wider range of long-lived radionuclides which are of interest for fusion researchers than the few that currently exist in the current 10CFR61 regulations. Fetter's model included more accurate transfer coefficients and dose conversion factors. However, while the NRC model limits the whole body dose to 500 mrem or the dose to any single organ (one of seven body organs) to 1.5 rem, Fetter limits are based on the maximum dose to the whole body only.

Specific activities calculated by the DKR-PULSAR2.0 code were used to calculate the waste disposal ratings (WDR). The waste disposal ratings for the Fetter and 10CFR61 limits are shown in Tables 6.9-1 and 6.9-2, respectively. Results in the tables are given for compacted wastes. Compacted waste corresponds to crushing the solid waste before disposal (to eliminate voids in the structure) and thus disallowing artificial dilution of activity.

Table 6.9-1. Class C Waste Disposal Ratings Using Fetter Limits

Zone	FPY	W-5Re	W-La_2O_3
IB FW	5	19.9	19.3
IB Shield	30	1.5	2.37
IB VV	30	0.015	0.035
OB FW	5	20.8	19
OB Blanket	30	17.6	24.78
OB Shield	30	0.226	0.377
OB VV	30	7.86e-3	0.022

Table 6.9-2. Class C Waste Disposal Ratings Using 10CFR61 Limits

Zone	FPY	W-5Re	W-La_2O_3
IB FW	5	4.24	8.22
IB Shield	30	0.896	1.645
IB VV	30	0.014	0.014
OB FW	5	3.54	6.77
OB Blanket	30	6.96	15.24
OB Shield	30	0.165	0.332
OB VV	30	8.46e-3	8.46e-3

As shown in Table 6.9-1, according to Fetter limits, the first wall, blanket, and inboard shield would not qualify for disposal as Class C waste. As a matter of fact the W-5Re alloy produces such a high activity that the first wall would have a WDR which is more than an order of magnitude higher than the Class C WDR limit. The high WDR is due to the ^{186m}Re, ^{108m}Ag, and ^{94}Nb isotopes. Only ^{186m}Re is a product of nuclear interactions with base elements in the W-5Re and W-La_2O_3 alloys. On the other hand, ^{108m}Ag($T_{1/2}$ = 130 yr), and ^{94}Nb($T_{1/2}$ = 20,000 yr) are produced by nuclear interactions with the niobium and silver impurities present in the tungsten alloys used in the analysis. All of the other components would qualify for disposal as Class C waste. The composition used for W-La_2O_3 has twice the amount of Nb impurities resulting in higher WDR than the W-5Re alloy. This result will change if the impurity level in the alloy can be controlled to a lower level. The results in Table 6.9-2 show that according to the 10CFR61 limits, the first wall and blanket would not qualify for disposal as Class C waste for either of the two tungsten alloys. In addition, the inboard shield will not qualify as Class C waste if the W-La_2O_3 alloy is used. The waste disposal ratings of all components are dominated by contribution from the ^{94}Nb isotope.

Reducing the niobium impurity in the tungsten alloys to about 1 wppm could allow for disposal of all components as Class C low level waste, if 10CFR61 limits are used. If Fetter limits are used, reducing the impurity levels of niobium and silver to 1 wppm could allow for disposal of the inboard and outboard shields as low level waste. On the other hand, the first wall and blanket could only be disposed as Class C waste if the niobium and silver impurities present in the *W-La2O3* alloy are reduced to levels less than 0.1 wppm. In addition, barium and molybdenum impurities need to be reduced to less than 1 and 10 wppm, respectively. Due to the presence of 5% rhenium in the W-5Re alloy, the first wall and blanket would not qualify for disposal as low level waste regardless of the level of impurities present in the alloy.

Since the first wall and secondary blanket will not meet the limits for Class C disposal, we examined the impact of producing non-low level waste on the total volume of waste generated. The first wall has a life-time of 5 FPY and the secondary blanket is a life-time component. The first wall represents less than 3% of the total volume of the waste (excluding magnets). Replacing the first wall every 5 years means that about 15% of the total volume of the waste (excluding magnets) would not qualify for shallow land burial as low-level waste. On the other hand, with the secondary blanket we have a choice of either replacing it every ~2 FPY and hence allowing for its disposal as Class C LLW, or keeping it for 30 FPY and disposing it as non-low level waste. Since the secondary blanket represents less than 3% of the total volume of the waste (excluding magnets), replacing it every 2 FPY would increase the total volume of the LLW by about 40%. In conclusion, in EVOLVE we have the choice between generating less than 20% of the waste volume (excluding magnets) as non-low level waste or limiting the non-low level waste to about 10% while increasing the total waste volume (excluding magnets) by about 40%.

References

[1] Nuclear Regulatory Commission, 10CFR Part 61, "Licensing Requirements for Land Disposal of Radioactive Waste," Federal Register, FR 47, 57446 (1982).

[2] S. Fetter, E. Cheng and F. Mann, "Long Term Radioactive Waste from Fusion Reactors," Fusion Engineering and Design **13,** 239 (1990).

6.10. Summary

The neutronics performance of the EVOLVE concept was analyzed using 2-D calculations. Scoping lithium tray boiling analysis were performed for the EVOLVE boiling blanket design to determine the vapor fraction distribution. Vapor fractions as high as 65% were obtained when magnetic field effects were not included. Inclusion of magnetic field effects could reduce the vapor fraction significantly to 6%–12%. Based on the 2-D neutronics calculations for the worst case conditions with the highest predicted Li vapor fraction distribution, all nuclear performance parameters are acceptable with a comfortable margin. Therefore, the EVOLVE boiling blanket is expected to perform adequately from the neutronics point of view for any of the boiling regimes considered. The neutronics parameters for the preliminary design of the transpiration blanket option were compared to those obtained for the boiling blanket with the largest predicted vapor fractions. The results indicate that with these assumptions, the transpiration blanket has larger Li and structure content resulting in slightly higher TBR and a factor of 2-5 better shielding performance. The nuclear performance parameters for both designs are acceptable with large margin implying that the choice between these two options should not be driven by differences in nuclear performance.

An update of the activation analysis was performed for the EVOLVE using the W-La_2O_3 alloy as a structure material. The results were compared to those obtained previously with the W-5Re alloy. The W-La_2O_3 alloy generates slightly smaller level of decay heat than W-5Re during LOCA. However, the selected W-La_2O_3 alloy has twice the amount of Nb impurities resulting in higher WDR than the W-5Re alloy. The W-TiC alloy is expected to generate similar WDR results unless it contains much smaller level of Nb impurities. The results indicate that reducing the Nb, Ag, Ba, and Mo impurity levels to 0.1–1 wppm results in all components qualifying as Class C low level waste. The only exception is in the case when Fetter limits adopted and the W-5Re alloy is used. In this case, the first wall, trays, and secondary blanket would not qualify for disposal as low level waste regardless of the level of impurities present in the alloy. The main advantage of using the W-La_2O_3 alloy could be the production of lower level of off-site dose during an accident because of the lower decay heat and reduced amount of ^{186m}Re.

7. EVOLVE Safety Evaluation

In this chapter we evaluate the safety potential of the EVOLVE design. EVOLVE is an innovative FW/blanket design concept cooled by vaporized lithium, resulting in low system pressures and a relatively slow circulation of liquid lithium. However, the decay heat of structural W-alloy of EVOLVE is relatively high. Therefore, it becomes necessary to evaluate the possibility of safely removing this decay heat during accident conditions. The reference point we use to assess the safety of EVOLVE is the DOE Fusion Safety Standard [1]. This standard was developed to enumerate the safety requirements associated with D-T magnetic fusion facilities. One requirement called out in this standard is that: "the need for an off-site evacuation plan shall be avoided." This requirement translates into a dose limit of 10 mSv at the site boundary during a worst-case accident scenario. To demonstrate that this requirement has been met, a broad range of accidents that could challenge the radiological confinement boundaries of EVOLVE (e.g., primary vacuum boundary (PVB), cryostat, or confinement building) must be examined. These accidents fall into three major categories [2]:

- Accidents that directly breach a confinement boundary (e.g., failure of the PVB by over-pressurization by an in-vessel loss-of-coolant accident),
- Accidents related to decay heat removal (e.g., a complete loss-of-active-cooling-accident), and
- Accidents associated with chemical reactivity of materials (e.g., an ex-vessel spill of lithium coolant).

An accident that qualifies as a worst case scenario for the EVOLVE facility is a complete-loss-of-offsite-power accident (CLOPA). This scenario could result in a complete loss of active cooling for the EVOLVE in-vessel components and an induced plasma disruption that could simultaneously fail the windows of a PVB port, allowing air from an adjoining room to enter the plasma chamber. The consequences would be the heat up of in-vessel components by decay heat, release of plasma facing component (PFC) tritium inventories, and mobilization of PFC activation products by surface oxidation. In this chapter, we examine the response of the EVOLVE design to this event. The following sub-sections describe the model developed to analyze the effectiveness of natural convection decay heat removal systems being proposed for EVOLVE, present predicted EVOLVE temperatures, detail radiological releases, and investigate the additional impact of a lithium fire during a CLOPA.

References

[1] DOE STD 6002-96, The Safety of Magnetic Fusion Facilities, May 1996.

[2] D.A. Petti, et al., "Safety and Environmental Assessment of ARIES-AT," 14th Topical Meeting on the Technology of Fusion Energy, Park City, Utah, October 15-19, 2000, to be published in Fusion Technology.

7.1. EVOLVE MELCOR Model Description

The CLOPA scenario has been analyzed with a version of the MELCOR code [1] that has been modified to treat lithium as a coolant [2]. A one-dimensional model of the EVOLVE design was developed that accounts for radial thermal conduction and gap radiation heat transport from the PVB inner wall to the outboard PVB outer wall. A schematic of this model appears in Figure 7.1-1, which illustrates the three EVOLVE cooling systems simulated by fluid flow volumes of this MELCOR model. The first cooling system is that for the internal components of the EVOLVE design, which are the: high temperature shield (HTS), first wall (FW) and primary

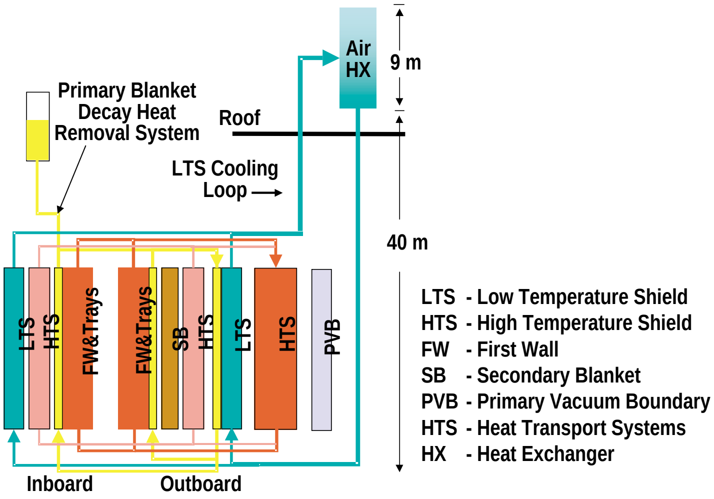

Figure 7.1-1. Schematic of MELCOR model of EVOLVE.

blanket (PB), secondary blanket (SB), and the flow paths from these components to a single volume representing the primary heat transport system (PHTS). The lithium within these components is modeled as a single fluid volume per component, in which volume the lithium is simulated as a pool and vapor above this pool.

The second cooling system is a FW or primary blanket decay heat removal system (PBDHRS) that operates by natural convection. This system is similar to the one employed by the ARIES-RS design [3], and is used here to transport heat in the radial direction from the FW and primary blanket trays to the LTS. As illustrated in Figure 7.1-2, the PBDHRS contains depleted lithium (Li-7) and consists of rectangular channels (40 mm x 80 mm) that are attached to the lithium tray back-plate and blanket stiffening ribs of the inboard and outboard primary blankets. These channels connect to similar channels attached to the wall of the outboard LTS. The pressure losses associated with four 90° bends were included in the flow modeling of these channels. During normal operation, MHD forces will minimize lithium circulation in this system, but under accident conditions these loops will self-initiate once the toroidal field coils have been discharged.

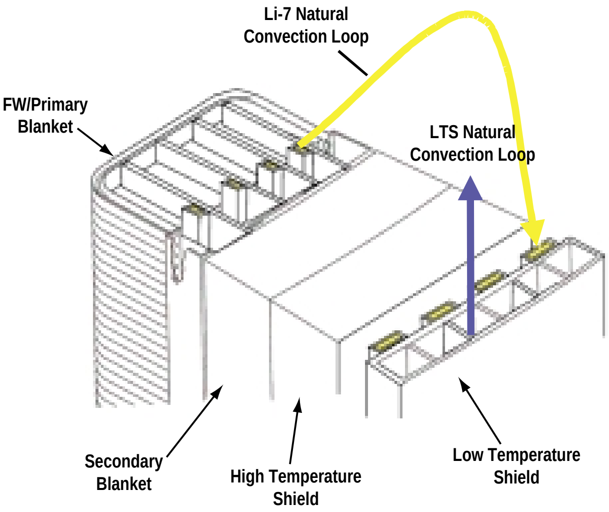

Figure 7.1-2. Schematic of MELCOR model of EVOLVE.

The third system is also a natural convection system designed to cool the LTS by exchanging the heat burden of the LTS to the ambient by way of a air heat exchanger located on the roof of the EVOLVE confinement building. The separate cooling loops of this system contain pipes between the reactor and roof heat exchanger (HX) that are modeled as: 80 m long, 40 m high, and containing ten 90° bends and four abrupt contraction/expansions. The LTS cooling channel width is assumed to be 40 mm, a width required for LTS heat transfer. The roof air HX has a footprint of 7 m x 2 m, a height of 9 m, and contains 24.5 mm diameter tubes (total surface area of 4690 m^2) with an overall heat transfer coefficient of 50 W/m^2-K. These HX design parameters are similar to those of the ITER design [4]. Three different coolants have been examined for the LTS cooling system, as will be discussed in detail in Section 7.2.2.

Figure 7.1-3 contains a schematic of the MELCOR conduction model for the internal components of the EVOLVE design. Radial one-dimensional heat conduction is modeled based on the material volume fractions called out in this figure. At gaps between components thermal radiation is treated. An effective emissivity of 0.2 was assumed between the surfaces of these gaps (a value that simulates roughened surfaces). Lithium convection internal to these components is also considered by the MELCOR code, for example lithium liquid and vapor convection with the FW and trays of the primary blanket module were included in this model. The inboard thermal boundary condition is adiabatic and the outboard thermal boundary condition is thermal convection and radiation to ambient temperatures. The height of these MELCOR heat conduction slabs is 6 m, with surface areas of 158 m^2 and 265 m^2 for the inboard and outboard structures, respectively. The specific decay heat (W/m^3) used for this mode is that presented in Chapter 6. Based on these decay heats, and the material volumes of the conduction model, the total decay heat burden for the EVOLVE design at plasma termination is 65 MW, dropping to 45 MW within three hours. Eighty percent of this decay heat is from the FW tubes and primary blanket trays. Figure 7.1-4 shows the change in this total decay heat burden with time. The model described in this section was used to obtain the results presented in the following section.

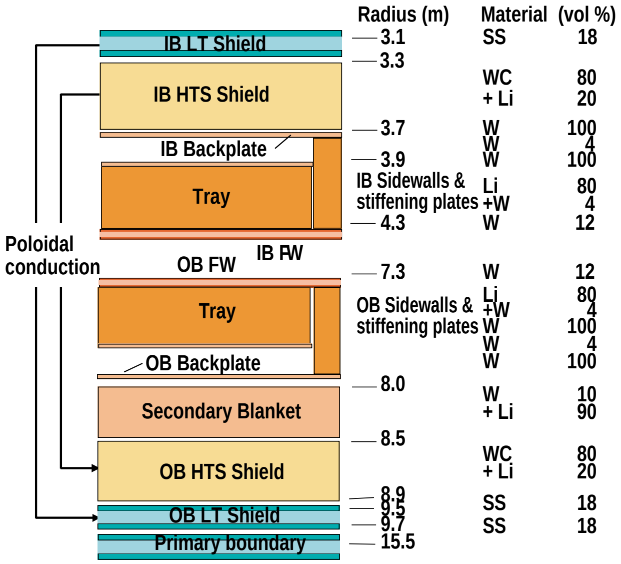

Figure 7.1-3. Schematic of EVOLVE component material composition for MELCOR conduction model.

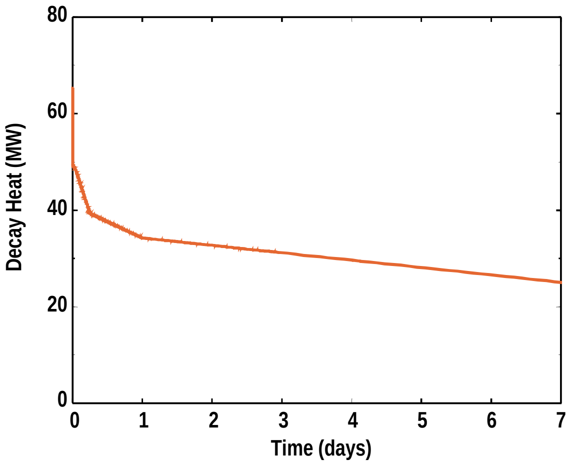

Figure 7.1-4. Predicted EVOLVE decay heat burden.

References

[1] R.M. Summers, et al., "MELCOR 1.8.0: A Computer Code for Severe Nuclear Reactor Accident Source Term and Risk Assessment Analyses," NUREG/CR-5531, Sandia National Laboratories report SAND-90-0364, January (1991).

[2] B.J. Merrill, "A Lithium-Air Reaction Model for the MELCOR Code for Analyzing Lithium Fires in Fusion Reactors," Paper presented at the IAEA Technical Committee Meeting on Fusion Safety, F1-TC-1165, Cannes, France, 2000, to be published in Fusion Engineering and Design.

[3] D. Steiner et al., "ARIES-RS Safety Design and Analysis," Fusion Engineering and Design **38**, 189-218 (1997).

[4] H.-W. Bartels, editor, "Accident Analysis Specifications for NSSR-2 (AAS)," version 2, S 81 RI 19 97-05-04 W1.1, SEHD 8.1.C-1, May (1997).

7.2. MELCOR Thermal Predictions

In this section we present the thermal results for the EVOLVE design during a CLOPA, explore the impact of excluding the PBDHRS during this accident, and conclude by presenting the possible coolant options for the LTS natural convection system.

7.2.1. EVOLVE Thermal Response during a Complete-Loss-of-Power Accident

Figure 7.2-1 shows temperatures predicted for the EVOLVE design during this accident scenario. From an initial operating temperature of 1400°C, the FW temperatures drop below 900°C in two hours, below 800°C in 13 hours, and below 700°C in 68 hours. The lithium velocity in the PBDHRS is initially 0.6 m/s, but gradually drops to 0.33 m/s by seven days. The LTS cooling system has been modeled as an active system capable of removing a maximum of 110 MW for this analysis. As can be seen, the PBDHRS effectively removes the decay heat from the FW during this accident by bringing the entire reactor to below 750°C within five days.

A parameter study was performed for this accident scenario that examined the impact of draining the lithium from the trays of the primary blanket. This has been discussed as a safety option for EVOLVE, whereby the lithium is drained into holding tanks to reduce the possibilities of incurring lithium-air fires. The consequences of this action are illustrated in Figure 7.2-2,

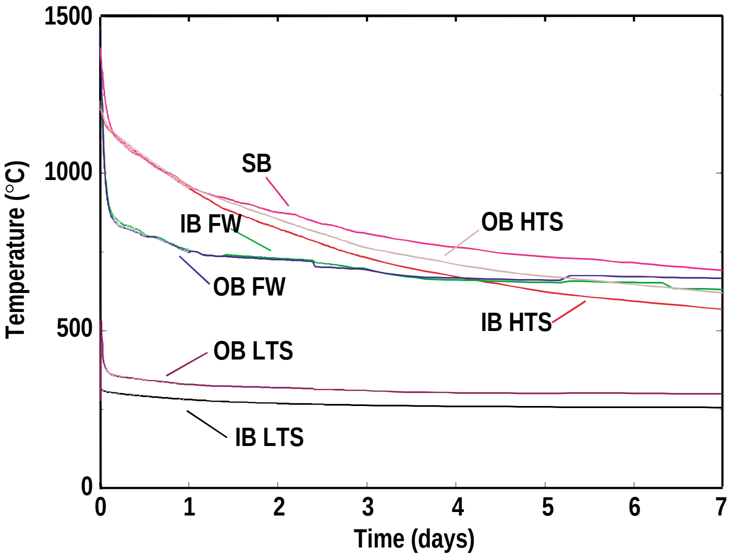

Figure 7.2-1. EVOLVE component surface temperatures during a complete loss of power accident scenario.

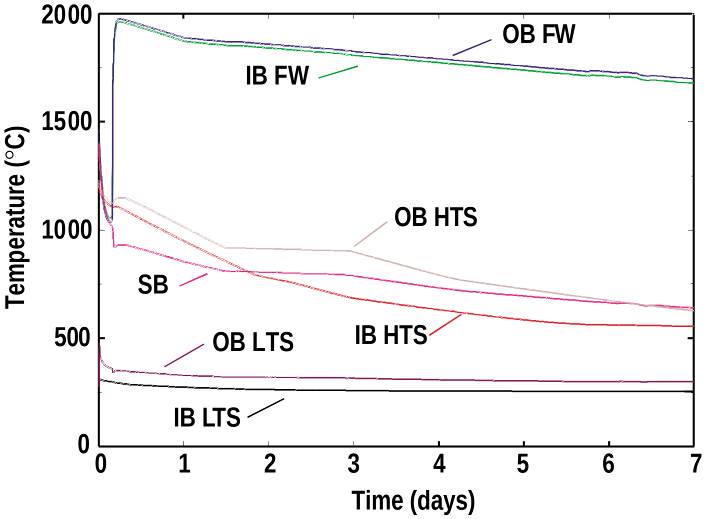

Figure 7.2-2. EVOLVE component surface temperatures during a complete-loss-of-power accident scenario when the lithium is drained from the primary blanket within five hours.

which presents the same temperatures as Figure 7.2-1, with the lithium drained from the primary blanket trays within five hours of the onset of this accident scenario. As can be seen, the FW temperatures jump from about 1050°C to 1950°C once the lithium is drained from the trays, posing a potential tungsten oxidation concern. This temperature remains high even after seven days. Therefore, because the lithium is an important convection medium for radial heat flow from the FW to the PBDHRS, it will not be a good safety practice to drain the lithium from the primary blanket without providing additional FW cooling. In contrast, the SB and HTS temperatures are slightly lower for this case because this study assumes that the lithium is being drained from the bottom of the primary blanket. As a consequence, the only way lithium leaves the SB and HTS is by evaporation and subsequent condensation of the vapor on the PBDHRS. This leads to some evaporative cooling of these components.

7.2.2. EVOLVE Thermal Response without the Primary Blanket Decay Heat Removal System

Figure 7.2-3 contains predicted EVOLVE temperatures during the same accident scenario analyzed in Section 7.2.1, except with the PBDHRS excluded from the calculation. As can be seen, the FW temperatures during this scenario climb to 2250°C in 2.5 days, after the in-vessel component lithium boils off. Even at the end of one month, the in-vessel temperatures remain above 1000°C. At a FW temperature 1200°C, the introduction of air would produce complete oxidation of tungsten within 80 hours. The reasons for these high FW temperatures are that 80% of the decay heat is produced in the FW/primary blanket module and the gaps between components of the EVOLVE design restrict radial heat flow. To illustrate this problem further, two additional cases were examined. One case assumed that the HTS cooling system is maintained through emergency power generators. The second case assumed no active cooling, only radial conduction/radiation to the ambient. Results for the first case appear in Figure 7.2-4. As can be seen, the maximum FW temperature drops from 1850°C to 1700°C for this case. However, this is still too high based on tungsten oxidation concerns. The second case, with only passive heat rejection to ambient by radial conduction and radiation, produces FW temperatures in excess of 3000°C. In addition, the in-board LTS temperature rises above the stainless steel melting temperature within one day. This would suggest the possibility of loss of structural integrity for the EVOLVE design if no LTS cooling is available during this event, illustrating the need for the passive LTS cooling system described in the following section.

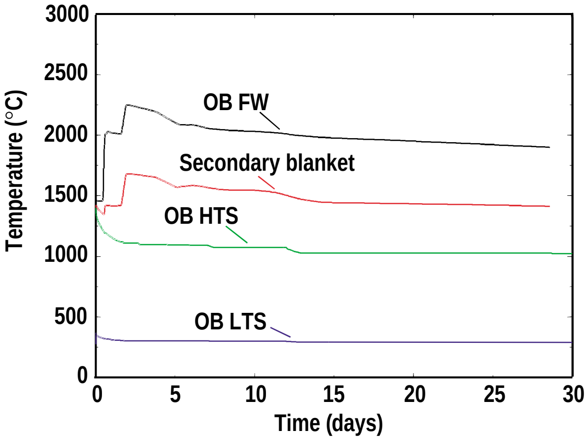

Figure 7.2-3.EVOLVE component surface temperatures during a complete-loss-of-power accident scenario without the proposed decay heat removal system, but with an active LTS cooling system operating on emergency power.

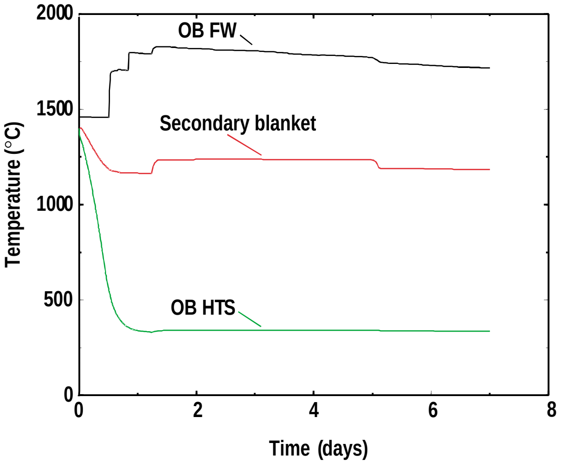

Figure 7.2-4.EVOLVE component surface temperatures during a complete-loss-of-power accident scenario without the proposed decay heat removal system, but with an active HTS cooling system operating on emergency power.

7.2.3. LTS Cooling System Coolant Options

Ideally we would like the LTS cooling system to be driven by natural convection that exhausts the LTS heat directly to ambient by way of an air HX located on the roof of the EVOLVE confinement building. As such this system would be a passive system, thereby affording a higher level of safety assurance than an active system. Desirable characteristics that the coolant of this system should have are: a good heat transfer medium, low or no induced radioactivity, low or no chemical reactivity with lithium or air, low vapor pressure, and high density change. Three coolant options have been examined for this coolant system, which are: organic coolant, gas, and molten salt.

The organic coolant examined is Diphenyl ($C_{12}H_{10}$). This coolant is a component of the organic coolant used by the Canadian WR-1 fission reactor [7]. Diphenyl does not have a strong chemical reaction with lithium, and has a low level of induced radioactivity. It is a wax that melts a 70°C, and has a saturation pressure of three atmospheres at 300°C. The density and heat transport properties of Diphenyl are similar to those of water. Steady-state energy and momentum calculations for the LTS cooling system design parameters called out in Section 7.1 show that a 25 MW natural convection system (0.23 m pipe diameter) is feasible if the phase change of Diphenyl at these conditions is taken advantage of by using an ebullient tube (1.0 m in diameter and 10 m in height). An ebullient tube is an expansion region in the system piping that is located at an elevation in the hot leg of the loop where the coolant will flash to a vapor, resulting in a density reduction of more than a factor of 20. Because a natural convection system operates on the basis of the density difference between the hot and cold legs of this system, an ebullient tube would enhance the loop flow provided that the cross-sectional flow area of the ebullient tube is large enough to accommodate the acceleration forces associated with the flashing process. Eight of these loops would be required, each cooling two sectors of the EVOLVE LTS. The disadvantages of using Diphenyl are that this coolant undergoes radiolytic and pyrolitic decomposition and is flammable.

A LTS cooling system containing gaseous helium as a coolant is also feasible. The advantages of helium are: no induced radioactivity, no chemical reaction with lithium, and high thermal conductivity. A LTS cooling system would be composed of sixteen separate loops (one per reactor sector), having coolant pipe cross-sectional areas of 1.0 m^2, and contain helium at a pressure of 50 atm. Figure 7.2-5 contains the predicted LTS thermal response during a CLOPA for different coolant pipe diameters and system pressures for the first 1500 s of this event. The desired maximum LTS temperature during this accident is about 600°C. These results illustrate the reason for the selecting the pipe diameter and helium pressure design parameters of 1.0 m^2 and 50 atm. The larger the pipe diameter the lower the flow resistance, and consequently the higher the natural convection flow rate. The higher the pressure the higher the helium density, and consequently the larger the system's capacity for heat removal. Figure 7.2-6 contains the predicted thermal response of EVOLVE to a CLOPA using this helium LTS cooling system. As can be seen, these FW temperature results are comparable to those obtained in Section 7.2.2. The major disadvantage of the helium option is the possibility of over-pressurization of EVOLVE confinement barriers. This safety issue is illustrated by the results in Fig. 7.2-7, where a loss-of-coolant accident from the LTS cooling system into the plasma chamber volume is shown. The size of the break in the LTS is set at a value that could be considered as the smallest break expected for the LTS, defined by the leak-before-break criterion [6]. This criterion has evolved in the fission industry when coolant pipes are seen to leak before the pipe actually ruptures, with the area of the leak equal to the pipe diameter times the pipe thickness divided by four (e.g., Dt/4). For this case the effective break diameter is 2.5 cm. As can be seen in Fig. 7.2-7, the plasma chamber pressure exceeds 2 atm within 60 s of the start of this accident, after which point it is assumed that windows in a duct that penetrates the PVB also fail. This would create a confinement boundary bypass where the radioactive inventories within the PVB can be vented into a room adjacent to the EVOLVE cryostat. As a consequence, if high-pressure helium is used for the LTS cooling system a pressure suppression system would have to be added to the EVOLVE design to ensure the integrity of the EVOLVE confinement barriers.

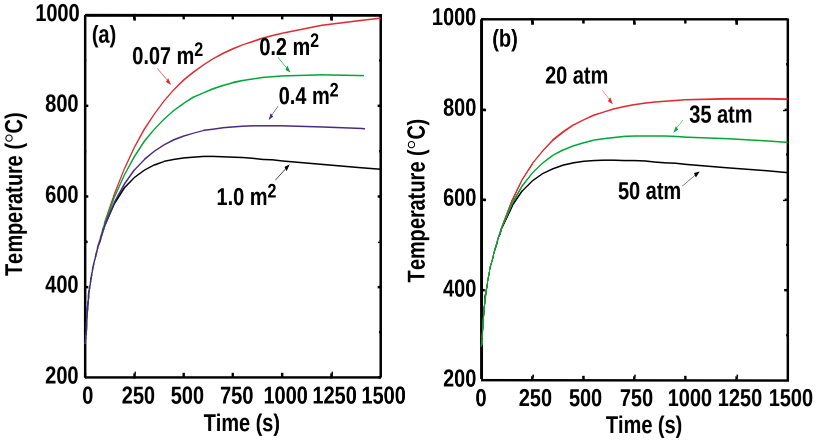

Figure 7.2-5. EVOLVE LTS surface temperatures during a complete-loss-of-power accident scenario as a function of LTS helium cooling system (a) pipe cross-sectional area at a pressure of 50 atm, or (b) pressure with a constant pipe area of 1.0 m^2.

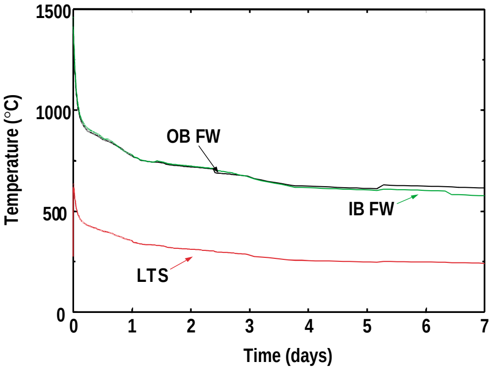

Figure 7.2-6. EVOLVE LTS surface temperatures during a complete-loss-of-power accident scenario with a LTS cooling system containing a helium coolant.

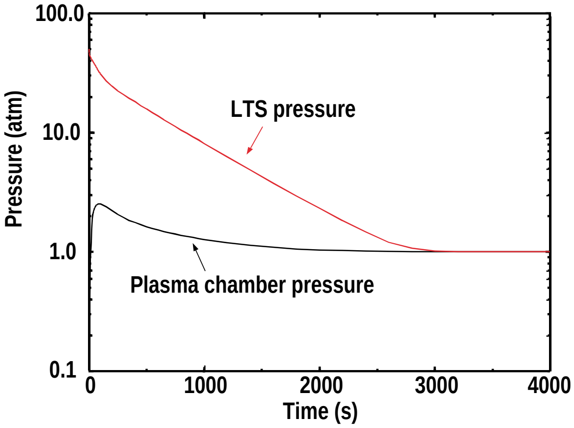

Figure 7.2-7. EVOLVE plasma chamber and LTS cooling system pressure during an in-vessel loss-of-cooling accident.

The third coolant option examined was the molten salt $NaCl-AlCl_3$. This molten salt has the advantage of a low melting temperature (105°C), a low vapor pressure (0.95 atm at 300°C [7]), and not expected to be chemically reactive with lithium. A LTS molten salt cooling system composed of 16 loops (one loop per reactor sector) was added to our MELCOR model. The response of this cooling system to a CLOPA is given in Figure 7.2-8. As can be seen, these FW temperature results are comparable to those obtained in Section 7.2.2. The disadvantages of this molten salt would be induced radioactivity (e.g., that of the aluminum component of this molten salt) and slight electrical conductivity (ten times seawater). The first problem would be a radioactivity release issue, the second would be induced MHD forces that were not included in this analysis.

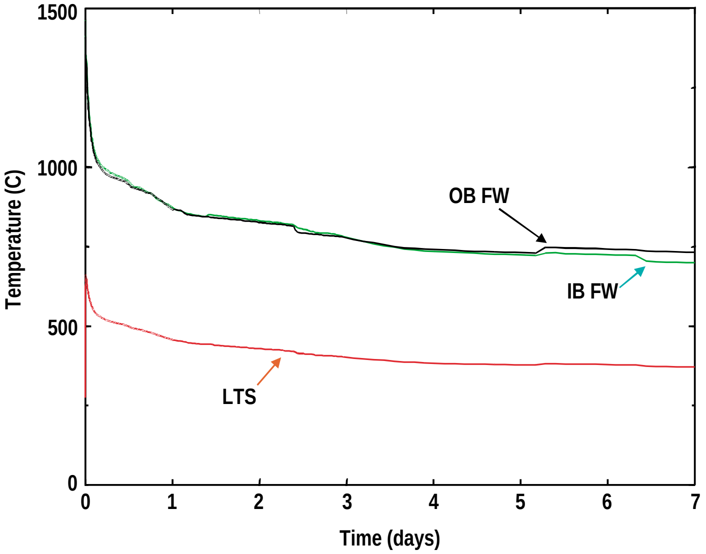

Figure 7.2-8. EVOLVE LTS surface temperatures during a complete-loss-of-power accident scenario with a LTS cooling system containing a molten salt.

All three of the coolants examined are feasible as a coolant for the LTS natural convection cooling system, each with certain safety advantages and disadvantages. Routing of the organic and molten salt coolants could be considered to minimize radiation damage and a pressure relief valve that vents the high-pressure helium to a less essential volume or room could minimize the pressurization impact of the helium. However, the adequacy of transmitting the after-heat to the PBDHRS under loss-of-pressure accidents in the midst of other accidental events needs to be assured.

7.3. Accidental Releases

As mentioned in the introduction, for the release of radioactive material to occur during a CLOPA a mechanism must exist that would result in the ingress of air into the EVOLVE plasma chamber. The postulated mechanism is an induced plasma disruption that fails the windows of a PVB port, allowing air from an adjoining room to enter the plasma chamber. To evaluate the release of in-vessel radioactive inventories during this accident scenario, the free volume of the plasma chamber, a non-nuclear room, a bypass duct that connects the plasma chamber and the non-nuclear room, and the heating-ventilation-air-conditioning (HVAC) system duct that connects the non-nuclear room to the environment were modeled. The modeling assumptions for these items are based on default parameters from the ITER EDA safety study [1]. The HVAC system was assumed to stop at the beginning of the event due to the power outage.

The rate of mobilization of activation products by oxidation of the FW tungsten alloy was based on temperature dependent data from Smolik [2]. In addition, the plasma disruption at the beginning of this event produces an additional 10 kg of dust. Both of these aerosol sources were given an initial mass mean diameter of 0.1 μm [1,2]. The initial specific activity of this aerosol mass was calculated from EVOLVE activation calculations of Section 6 to be about 3.3×10^5 Ci/kg. In addition to this aerosol source, the release of the tritium from the PFCs must also be accounted for. Because implanted tritium inventories for EVOLVE are not available, the predicted ARIES-AT tungsten divertor inventory of 0.4 g/m^2 was adopted for this study [3]. When this inventory is adjusted for temperature differences between the ARIES divertor and the EVOLVE FW based on experimental data [4], the estimate for the EVOLVE FW is 0.18 g/m^2. The resulting total FW tritium inventory would be 76 g, all of which would be immediately released during this accident. Radiological dose calculations [5] for ground level releases of various radionuclides (1 km site boundary assuming average weather conditions) give a specific dose for the tungsten alloy aerosol of 130 mSv/kg, and for the tritium (HTO) of 67 mSv/kg. More than 90% of the tungsten alloy aerosol dose is due to Re 184 and Re 184 m.

Figure 7.3-1 contains the predicted tungsten alloy mass mobilized during the first week of this accident and the amount of this mass that is released to the environment by way of the HVAC duct if filtration is neglected. The total amount of tungsten alloy aerosol mobilized in the first seven days of the accident is 357 kg (95% of which is released during the first 2.3 days), and the amount vented to the environment without filtration is 7.8 kg. Given the additional dose of about 5 mSv associated with the HTO release, the non-nuclear bypass room would have to be isolated within 2.4 hours in order to meet the no-evacuation dose goal of 10 mSv if no filtration of the HVAC duct flow occurs. This time period could be extended to 1.6 days with filtration (99% filtration efficiency [6]). Both of these response times are reasonable. Therefore, EVOLVE can easily meet the no-evacuation goal for this accident.

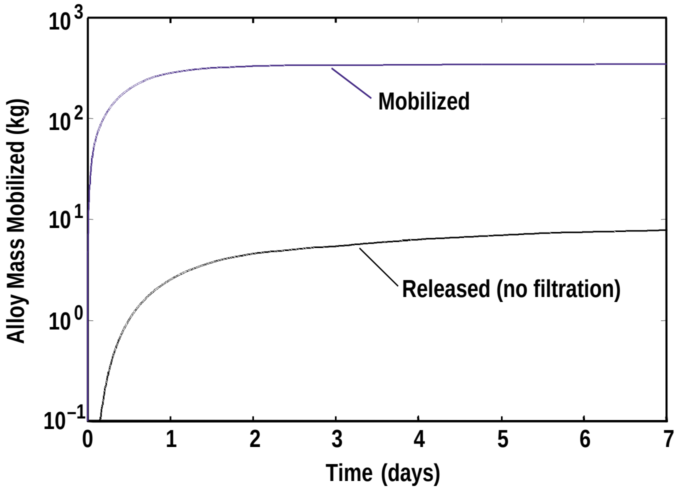

Figure 7.3-1. Tungsten alloy mass mobilized during a complete-loss-of-power accident scenario.

References

[1] H.-W. Bartels, editor, “Accident Analysis Specifications for NSSR-2 (AAS),” version 2, S 81 RI 19 97-05-04 W1.1, SEHD 8.1.C-1, May (1997).

[2] G.R. Smolik, and K. Coates, “Mobilization from Oxidation of a Tungsten Alloy in Air,” ITER Engineering File, ITER/US/96/TE/SA-2, September (1996).

[3] D.A. Petti, et al., “Safety and Environmental Assessment of ARIES-AT,” 14th Topical Meeting on the Technology of Fusion Energy, Park City, Utah, 2000, to be published in Fusion Technology.

[4] V.Kh. Alimov and B.M.U. Scherzer, “Deuterium Retention and Reemission from Tungsten Materials,” J. Nucl. Mater. **240**, 75-80 (1996).

[5] M. Abbott, “Revised Results – MACCS2 Doses for Fusion Isotopes Release to the Atmosphere using P-G Dispersion Parameters,” an INEEL letter to D.A. Petti, MLA-11-99, April 14, 1999.

[6] L.C. Cadwallader, “Ventilation System Operating Experience Review for Fusion Applications,” INEEL Report, INEEL/EXT-99-001318, December (1999) p. 10.

7.4. Lithium Chemical Reactivity

Because the reaction of high temperature lithium with air is highly exothermic, the EVOLVE design has significantly reduced the possibility of lithium-air fires by placing all lithium bearing systems within a vacuum boundary (e.g., the PVB). Therefore, a credible accident scenario must be postulated that results in the mixing of air and lithium as a worst-case accident scenario. We have looked to the CLOPA as that accident during which the postulated plasma disruption that fails the windows of a PVB port also produces runaway electrons that when lost from the plasma fails the FW of an outboard primary blanket module. The FW failure occurs by material melting due to the energy deposition associated with these electrons. In ITER it was estimated that the area of the hole generated by these electrons would be about 1.6×10^{-3} m^2 [1]. This failure, coupled with the air ingress from the PVB window failure, would result in the mixing of lithium and air within the EVOLVE plasma chamber during this CLOPA. Because the liquid lithium of the EVOLVE design resides in trays, the maximum amount of liquid lithium that would be spilt is only that associated with a single tray. Because this inventory is small, liquid lithium/air fires are not considered to be a significant safety issue for EVOLVE. However, because the lithium vapor pressure is above atmospheric conditions at 1400°C, flashing of liquid lithium in the EVOLVE blankets would result in lithium vapor mixing with air in the EVOLVE plasma chamber. While no experimental information exists for the rate at which lithium vapor reacts with air, it is assumed here, based on experiments investigating liquid lithium-air reactions, that a vigorous lithium-air flame will immediately form near the FW break.

To analyze this phenomena for EVOLVE, the lithium pool-air fire model of Ref. [2] was modified to include lithium vapor burning in the atmosphere of a MELCOR fluid volume. The approach taken was to model the lithium vapor-air reaction in a similar fashion to that of the MELCOR model for hydrogen gas-air deflagrations. This model assumes that a flame front will propagate through a mixing zone at the speed of sound for that mixture. This constitutes the fastest possible burn rate, excluding burn rates that result in mixture detonation. For this model, the lithium burn rate (kg/s) for a lithium-air mixture is defined as $\dot{m}_B = M_v^{Li} / \tau_B$, where M_v^{Li} is the mass of lithium in the mixture volume, and is the time constant for the mixture to burn. The burn time constant is defined as $\tau_B = r/c_s$, where r is the radius (m) of the mixture volume (assumed here to be a sphere equal in volume to the atmosphere of the MELCOR volume) and c_s is the speed of sound in the mixture (m/s). This burn rate was added to the lithium vapor conservation of mass equation as a sink term for all MELCOR fluid volumes where lithium vapor and air coexist. Similar terms for the oxygen and nitrogen conservation of mass equations were developed based on the stoichiometric formulas given in Ref. [2]. These mass sink terms were limited to the amount of lithium, oxygen, or nitrogen gas that exists in any given MELCOR volume per computational interval. The lithium burn rate times the heat of reaction for forming Li_2O and Li_3N were also added as source terms to the atmosphere conservation of energy equation for all MELCOR volumes where lithium vapor and air coexist. The partitioning between the rate of oxygen and nitrogen burn is based on the mass ratio of oxygen and nitrogen in a particular MELOCR fluid volume.

The MELCOR model described in the previous sub-section was modified to analyze the occurrence of a lithium air fire during a CLOPA, by subdividing the plasma chamber into two volumes. One volume equals one sixteenth of the total volume (e.g. the volume associated with a single sector) representing the mixing zone and the second volume representing the rest of the plasma chamber. In addition, the fluid volumes and heat structures representing the internal components and cooling systems of EVOLVE where scaled by one sixteenth, and two additional heat structures representing the rest of the inboard and outboard FW were added to the model.

Figures 7.4-1 to 7.4-4 present some results from this preliminary model for this accident scenario. Figure 7.4-1 contains the predicted pressures in the outboard primary blanket, mixing zone (plasma chamber), and the non-nuclear room. Of interest in this figure is that the plasma chamber rapidly pressurizes to an atmosphere in slightly more than one second, and comes into equilibrium with the primary blanket pressure in slightly over six seconds. A gradual pressure rise occurs in the non-nuclear room to about 1.1 atm by 60 s, but drops back to about 1.0 atm by 200 s. By 1000 s there is very little pressure difference among these EVOLVE components.

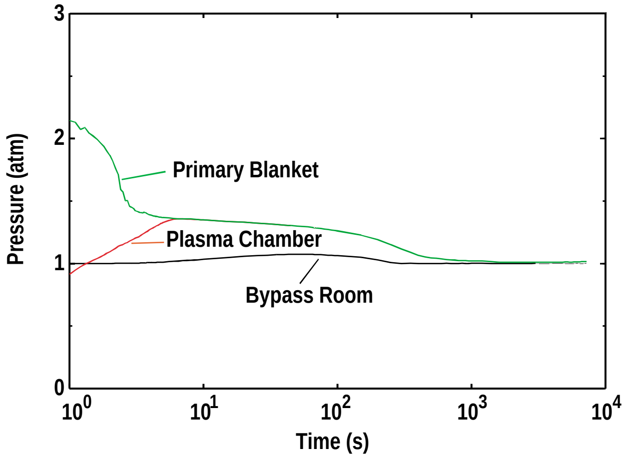

Figure 7.4-1. EVOLVE pressures during a lithium fire.

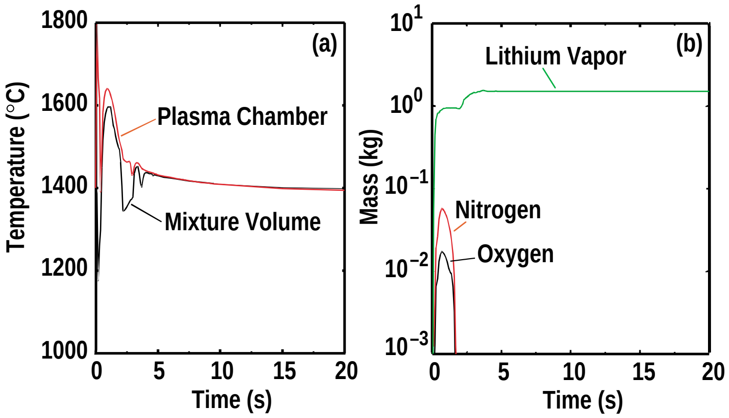

Figure 7.4-2. EVOLVE vapor (a) temperatures and (b) masses during a lithium fire.

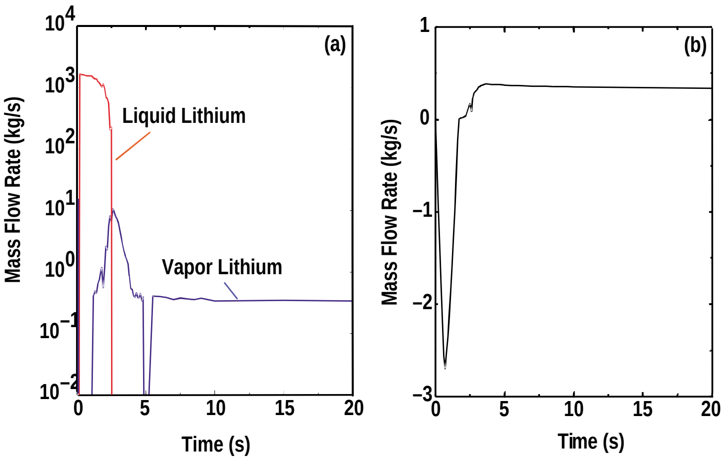

Figure 7.4-3. EVOLVE (a) break and (b) bypass duct mass flow during a lithium fire.

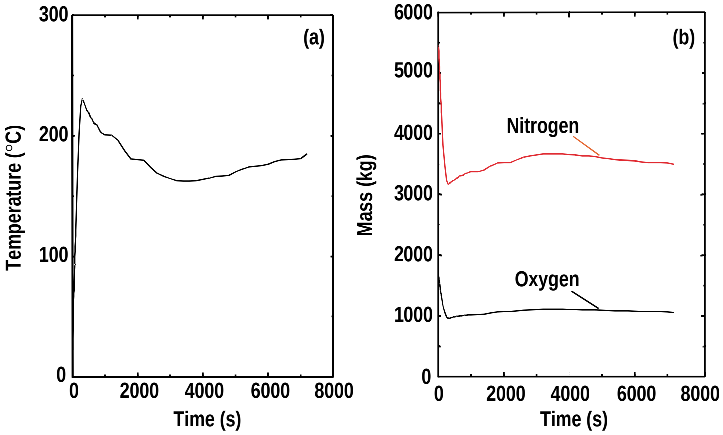

Figure 7.4-4. EVOLVE bypass room atmosphere (a) temperature and (b) masses during a lithium fire.

Figure 7.4-2 presents the plasma chamber and mixing zone temperatures and the mixing zone vapor masses during the first 20 s of this event. The mixing zone temperature initially drops to 1200°C due to expansion cooling of the lithium vapor and the cooler air coming from the non-nuclear room by way of the bypass duct. As the deflagration continues, the temperature of the mixing zone reaches a peak of 1600°C by one second, the time at which the pressure in the plasma chamber exceeds one atmosphere pressure. The temperature in the remainder of the plasma chamber reaches a peak of 1800°C. This temperature is slightly higher because of continued deflagration and compression heating of the gases exiting the mixing zone. The mass of lithium vapor, oxygen and nitrogen in the mixing zone is given in Figure 7.4-2(b). The mass of oxygen and nitrogen reach maximums of approximately 0.012 and 0.05 kg, respectively, by one second, and rapidly drop to near zero by two seconds. Beyond two seconds, the flame front moves from the plasma chamber, through the bypass duct, and into the non-nuclear room, which can be seen from the results of the next two figures.

Figure 7.4-3 contains the break and bypass duct mass flows for the first 20 s of this accident. Liquid lithium exits the FW break until two seconds. By 2.5 s, flow of liquid lithium stops and only vapor exits the break. The vapor flow rate peaks at near 10 kg/s and drops to about 0.4 kg/s by five seconds. The bypass duct flow is initially into the mixing zone, but by five seconds this flow has reversed directions and comes into equilibrium with the break flow. Figure 7.4-4 contains the air temperature and masses in the bypass room for this accident. This temperature reaches a maximum of 225°C, drops to 170°C by one hour, and rises again to about 190°C by two hours. The mass of oxygen and nitrogen in the non-nuclear room drops to 60% of the initial values after the flame front reaches the end of the bypass duct, and then plateau as the rate of air consumption in the non-nuclear room equals the rate of air being replenished from the ambient by way of the ventilation duct. This calculation was arbitrarily terminated after two hours, because by this time the non-nuclear room would have been isolated (note previous subsection). From this point on, the flame at the end of the bypass duct would consume the available air in the bypass room, extinguish the flame due to oxygen starvation, and the atmosphere of the bypass room would become lithium vapor.

Based on these preliminary results, there appears to be no additional safety issues produced by a lithium fire in EVOLVE during a CLOPA for two reasons. First, the maximum flame temperature is considerably below the melting temperature of tungsten. And second, even though the FW temperatures will be slightly higher than those for a CLOPA-only scenario, there is little if any oxygen available for oxidizing the FW. As a consequence, the only release for this event is the tritium from the in-vessel components, which results in only a 5 mSv dose at the site boundary. There will, of course, be additional remediation issues associated with this accident scenario that deal with lithium fire suppression, lithium cleanup, and ensuring that enough lithium remains in the trays to avoid the temperatures of Figure 7.2-2.

It may be of interest to speculate as to the impact that FW break size has on the outcome of this accident scenario. Based on the pressure results in Figure 7.4-1, a larger break size would not have a significant impact on the present results because at the adopted break size the plasma chamber pressure already rapidly equilibrates with the primary blanket pressure (within 10 s). A larger break would mean a more rapid plasma chamber pressure rise, and a smaller transition time for the flame front to move into the non-nuclear room. After this point, the major resistance to flow is the bypass duct. So from the standpoint of the non-nuclear room there would be very little difference in lithium vapor exiting this duct. At most this flow could increase by a factor of two before choked flow conditions occur in the bypass duct, but this flow would rapidly return to 0.4 kg/s as the blanket pressure drops to 1.2 atm by 10 s. However, a smaller break size could be a different matter because this case would be lithium vapor limited. As a consequence, the flame front would not move out of the plasma chamber and down the bypass duct into the bypass room, but remain in front of the FW break. While this flame would result in additional FW heating at the location of the break, this heating may not enhance the mobilization of FW material by oxidation because the existence of the flame would reduce the oxygen level near this FW region. However, future analyses should be performed to investigate this possibility in more detail.

References

[1] H.-W. Bartels, editor, “Accident Analysis Specifications for NSSR-2 (AAS),” version 2, S 81 RI 19 97-05-04 W1.1, SEHD 8.1.C-1, May (1997).

[2] B.J. Merrill, “A Lithium-Air Reaction Model for the MELCOR Code for Analyzing Lithium Fires in Fusion Reactors,” Paper presented at the IAEA Technical Committee Meeting on Fusion Safety, F1-TC-1165, Cannes, France, 2000, to be published in Fusion Engineering and Design.

7.5. Summary of EVOLVE Safety Results

We have developed a MELCOR model of the EVOLVE design to investigate the response of this design to a CLOPA. This model included the internal components of the EVOLVE design as well as the heat removal systems of this reactor. Three candidate coolants were identified for the LTS natural convection cooling system, each with different safety advantages as well as safety disadvantages. It was demonstrated that all three coolants could work in the context of a CLOPA scenario. Based on FW oxidation and aerosol transport calculations during a CLOPA, the dose goal of 10 mSv set by the DOE Fusion Safety Standard can be met if the EVOLVE confinement building ventilation system is manually closed within two hours, thereby isolating EVOLVE from the environment. In addition, it was demonstrated that even in the event of the most probable lithium fire scenario during a CLOPA that the risk to the public of this accident scenario would not increase because FW oxidation during a lithium fire is less likely to occur than without a lithium fire. Finally, a crucial finding of this study is that a high decay heat design like EVOLVE will require sustained cooling during a CLOPA in order to cool internal components and to meet required public dose goals. This cooling could be supplied by an active safety system, but the preferred approach is the passive system proposed by this study for the EVOLVE design.

8. W-Alloy Fabrications and Testing

Our experience with fabrication of tungsten structures and materials development for this purpose comes from two directions. The first direction deals primarily with bulk tungsten metallurgy. Sandia National Laboratories has expertise in this area and maintains collaborations with Russian researchers on tungsten metallurgy. Also, through our collaborations with Japanese researchers, we are aware of materials development of tungsten alloys and molybdenum alloys with the aim of increasing the ductile-brittle transition temperature [1-3]. To date small lots of material have been produced with some impressive results. However, definitive testing of these materials with notched specimens has not yet been done. Also, there has been significant work in developing tungsten armor for ITER and in joining of this armor to copper heat sinks.

The second direction, which has more direct applicability to the fabrication issues for EVOLVE, is the significant advances in the development of helium-cooled plasma facing components (PFCs) for fusion [4-6]. In the past several years, advancements in the technology of extended surface such as micro-channels and porous metal media have brought dramatic improvements in the heat removal capabilities of helium-cooled heat sinks [7-9]. This work and the related testing and performance of tungsten heat sinks is the primary subject reported here.

While the helium-cooled configurations do not correspond directly to the lithium-cooled tungsten first wall concept currently being pursued in APEX, the work reported here did derive from an earlier effort on helium-cooled tungsten concepts [10]. Interest in tungsten as a plasma-facing material lead to the development by Thermacore, Inc. of helium-cooled tungsten mockups that withstood uniform steady state heat fluxes in excess of 5 MW/m^2 using 50°C helium at 4 MPa. The excellent performance of this helium-cooled tungsten heat sink is a very promising result that is to some degree independent of the coolant.

Over the last decade, there has been a continuing effort at Sandia National Laboratories in the testing of helium-cooled mockups for fusion applications. The mockups have been designed and fabricated by General Atomics and by several small businesses in the U.S. that received grants for this purpose from the U.S. Dept. of Energy. This work has built in part upon development activities by two small businesses that manufactured helium-cooled refractory modules for high heat flux testing at Sandia National Laboratories. Some information on fabrication is given first and then a summary of the high heat flux tests is reported.

During the 1990s, Thermacore, Inc. of Lancaster, PA, through grants from DOE's Small Business Innovative Research (SBIR) Program, developed water-cooled and helium-cooled modules that utilized brazed copper balls as a porous heat transfer medium in copper, Glidcop™ or molybdenum coolant channels. They designed and built a series of helium-cooled modules that were tested at Sandia and elsewhere.

Figure 8-1 shows the refractory module built by Thermacore in 1999-2000 [4]. The heat exchanger(s) were constructed almost entirely of pure tungsten using high temperature Ni-based brazes. Each module consisted of a tungsten cylindrical end cap containing a hemispherical shell of brazed tungsten porous metal. This end cap was brazed onto a tungsten cylindrical tube bottomed by a flat tungsten plate that facilitates the brazed attachment of 316 stainless steel supply tubes. Both modules are 3.2 cm in diameter and approximately 7.7 cm long. The tungsten cylinder acts as the pressure boundary. Inside the cylindrical tube a stainless steel bellows supplies helium from the inlet tube to the center of the porous metal end cap. The helium flows from the center axis of the hemisphere through the porous layer and exits along the circumference of the hemisphere where it is collected in the tungsten cylinder and leaves via the stainless steel exit tube. The tungsten PMHX was fabricated in four separate assembly- brazing steps, all using BAu-4 (Nioro™) braze filler metal, either 0.010" or 0.020" diameter wire, in a dry hydrogen atmosphere.

Two modules of the type shown in Figure 8-1 were subjected to high heat flux testing. These results are summarized later.

Ultramet, Inc. of Pacoima, CA also participated in the SBIR Program. The company has designed and built commercial products made of refractory metals for rocket nozzles and other applications. Ultramet uses a process in which they build up refractory material with chemical vapor deposition (CVD) to create a metallized foam that is integrally bonded to fully dense material [9]. The flexibility of their process and the feature of the integrally bonded porous media are very attractive features that seem well suited to application in a refractory metal heat sink cooled using a porous metal region to enhance the heat extraction from an adjacent heated wall. Figure 8-2 shows an example of the integral bonding. This is a heat exchanger with an Inconel 718 outer shell, a Re liner and Re foam on a 0.75 inch ID Mo mandrel. The Re foam is 15% dense with 45 pores/inch. Ultramet indicated that the foam could initially be squeezed in two dimensions to give elongated pores as small as ~0.05 mm diameter. The cell shape is more evident in the previous figure. Irregular ligaments rather than 2-D walls make up the structure.

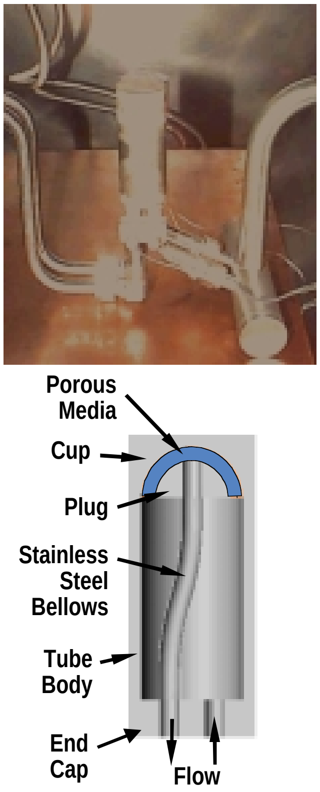

Figure 8-1. He-cooled tungsten heat sink made by Thermacore, Inc.

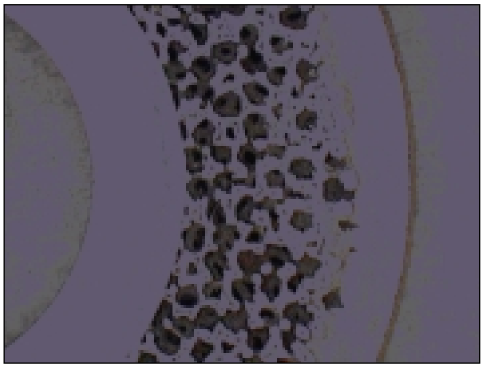

Figure 8-2. Re foam heat exchanger made by Ultramet, Inc.

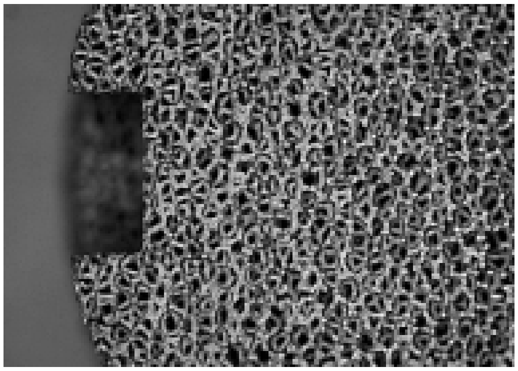

Figure 8-3. Porous Ta implant made by Ultramet, Inc., diam. is 0.75 inc.

Figure 8-3 shows a Ta foam with 80 pores/inch, 15% density, and an outer circumference with a machined thread. The item is used for bone implants to obtain metal foam with high open porosity, they begin with a plastic foam prescursor that is cut to the desired shape. The precursor is then pyrolized in place to give a rigid graphite structure that is then coated with metal or ceramic material in a CVD process.

The high amount of open porosity and the limited surface area both offer promise for significantly reducing the pressure drop along the flow path compared with the ball-aggregate concept. The initial hope in developing a refractory He-cooled first wall was that the open porosity of the metallized structure would have a low enough pressure drop for axial flow in a channel filled with metallized foam. In principle, a design that combined the metallized foam fabrication technology with the circumferential flow concept also seems possible and would have the advantage of reducing the axial pressure gradient along the first wall at the cost of a somewhat more complex internal configuration.

References

[1] H. Kurishita et al., “Effect of Neuton-Irradiation on Low temperature Toughness of TiC-dispersed Molybdenum Alloys,” J. Nucl. Mater. **239**, 253 (1996).
[2] H. Kurishita et al., “Development of Mo Alloys with Improved Reistance ot embrittlement by Recrystallization and Irradiation Molybdenum Alloys,” J. Nucl. Mater. **237,** 557 (1996).
[3] K. Tokunaga et al., “High Heat Load Properties of TiC-dispersed Mo Alloys,” J. Nucl. Mater. **241**, 1197 (1997).
[4] D.L. Youchison, M.T. North, “Thermal Performance of a Dual-Channel, Helium-Cooled, Tungsten Heat Exchanger,” Fusion Tech. **39**, 899 (2001).
[5] D.L. Youchison, M.T. North, J.E. Lindemuth, J.M. McDonald and T.J. Lutz, Fusion Eng. & Design **49-50**, 407 (2000).
[6] D.L. Youchison, M.G. Izenson, C.B. Baxi and J.H. Rosenfeld, Fusion Tech. **29**, 559 (1996).
[7] M.T. North and J.H. Rosenfeld, “Test Results from a Helium Gas-cooled Porous Metal Heat Exchanger,” High Heat Flux Engineering III, ed. Khonsary, Vol. 2855 (1996), ISBN 0-8194-2243-6.
[8] J.H. Rosenfeld and J.E. Lindemuth, Proc. 1993 IEEE/NPSS 15th Symp. Fusion Eng., Vol. 2, IEEE, Hyannis, Massachusetts, 1993, pp. 1210-1213.
[9] J. Sherman, R.H. Tuffias and R.B. Kaplan, “Refractory Ceramic Foams: A Novel, New high Temperature Structure,” Ceramic Bulletin **70**, 1025 (1991).
[10] C.P.C. Wong et al., “Helium-cooled Refractory Alloys First Wall and Blanket Evaluation,” Fusion Engineering and Design **49-50**, 709-717 (2000).

8.1. <u>High Heat Flux Testing of He-Cooled Modules</u>

In addition to design studies, hardware development of helium-cooled plasma facing components has continued in the fusion program. He-cooled test modules of several types have been tested in the Electron beam Test System (EBTS) at the Plasma Materials Test Facility operated by Sandia National Labs as shown in Table 8.1-1.

Table 8.1-1. Sandia High Heat Flux Tests in Helium-Cooled Test Articles

Year	Type of Test Article	Fabricator
1993	Micro-channel HX (~100μ channel size)	Creare, Inc.
	Divertor mockup A (0.46mm channels)	General Atomic
	Porous metal HX (40% porosity, 0.43 mm dia.)	Thermacore, Inc.
1994	Dual channel porous metal HX	Thermacore, Inc.
	Divertor mockup A retest at higher heat loads	General Atomic
1996	Phase-II porous metal HX	Creare, Inc.
	Vanadium HX	General Atomic
1997	Faraday shield A	Thermacore, Inc.
	Divertor mockup B	Thermacore, Inc.
1998	Faraday 2nd shield B	Thermacore, Inc.
	Divertor 2nd mockup C	Thermacore, Inc.
1999	Divertor mockup B retest, added diagnosics	Thermacore, Inc.
2000	Tungsten-rhenium tubes with porous media	Ultramet, Inc.
2000	Tungsten divertor mockups	Thermacore, Inc.

A divertor mockup made by Thermacore and tested in 1998 withstood steady-state heat fluxes above 35 MW/m^2 in tests in EBTS in which the heated spot was much smaller than surface of the module. However, the results are somewhat misleading in that they are not representative of the much lower values of maximum steady-state heat flux that are obtained when where the entire surface of a He-cooled heat sink is heated. The ultimate performance of this heat sink with a uniform heat flux over its entire surface could not be evaluated because the heat load would exceed the heat rejection capability of the helium loop.

In year 2000 Thermacore, Inc. fabricated a tungsten He-cooled module that withstood uniform steady state heat fluxes in excess of 5 MW/m^2 using 50°C helium at 4 MPa in high heat flux tests at Sandia. The purpose of these experiments was to test the robustness of the modules, characterize the thermal response and thermal fatigue resistance, and evaluate the effects of mass flow instabilities when a large difference was present in the helium temperatures of adjacent heat sinks with common inlet and exhaust manifolds.

Each module was heated over 90% of the faceplate encompassing a 4.9 cm^2 heated area. Pressurized helium provided the cooling at an absolute pressure of 4.0 MPa and inlet temperatures between 40 and 55°C. Pressure drops across each module as high as 55 kPa were recorded at maximum blower speed. Measured flow characteristics suggest that one module may have 30% lower porosity than the other.

The lower porosity module, achieving a flow of only 1.1 g/s of helium, survived a uniform heat flux of 5.5 MW/m^2 reaching a maximum surface temperature of 934°C with a 472°C gain in the helium temperature. The other module flowed 4.5 g/s of helium and absorbed 5.9 MW/m^2 producing a surface temperature in excess of 840°C with a 189°C gain in helium temperature. Using a 10 mm-dia bypass tube around one of the heated modules produced a 39% reduction in mass flow due to density decreases in the hot leg that increase the flow in the bypass. In this worst case configuration, the module surface temperature increased by roughly 110°C. However, no flow instabilities were detected when the modules were mounted in parallel, and only slight differences in thermal performance were observed compared to the single channel results at the highest heat fluxes.

9. Design Window for Tungsten Alloys

9.1. Introduction

The focus of this section is on the potential operating design window of tungsten alloys (W-alloys) for the APEX Evolve Study. Over the past decades, several studies have reviewed various W-alloys, such as, W-1%La_2O_3, W-5%Re, W-30Cu, W-Ni-Fe, and W-Ni-Cu [1–3]. Table 9.1-1 gives lists the pertinent physical and mechanical properties of W-alloys considered for ITER [4].

Sections 9.2, 9.3, and 9.4, give a summary of recrystallized W-Re alloy properties, the effects of radiation damage in refractory-alloys, and liquid coolant compatibility with refractory alloys, respectively. The high temperature creep strength limits are modeled using the Larson-Miller criteria and results are reported in Section 9.5. The lack of irradiation data at EVOLVE-Study relevant high operating temperatures (~1200°C) calls for the use of phenomenological models to estimate the DBTT of W-alloys at elevated temperatures. In Section 9.6 a phenomenological model to estimate changes in DBTT of W is presented.

Recently, new W-alloys based on the addition of carbides have been suggested. Recommendations regarding the philosophy of developing new W-alloys are briefly outlined in Sections 9.7 and 9.8.

References

[1] I. Smid, et al., J. Nucl. Mater. **258-263**, 160 (1998.

[2] V. Barabash, G. Federici, R. Matera, A.R. Raffray, “Armour Materials for the ITER Plasma Facing Components,” Physica Scripta **T81**, 74–83 (1999).

[3] V. Barabash, G. Federici, M. Rodig, L.L. Snead, C.H. Wu, “Neutron Irradiation Effects on Plasma Facing Materials,” J. Nucl. Mater. **283**, 138–146 (2000).

[4] M.A. Meyers, *Mechanical Behavior of Materials*, Prentice Hall, United Kingdom (1998) p. 550.

9.2. Summary of Recrystallized W-(5%–10%) re properties

9.2.1. Ultimate Tensile Strength (unirradiated)

$$\sigma_{UTS}(\mathrm{MPa})=377.9 + 0.03207*T - 1.955\times10^{-4}*T^2 + 5.13\times10^{-8}*T^3 \text{ (T in °C)}$$

– Pure W values.

9.2.2. Yield Strength (Unirradiated)

$$\sigma_Y(\mathrm{MPa}) = 94.2 - 0.0214*T - 2.12\times10^{-6}*T^2 - 7.48\times10^{-10}*T^3 \text{ (T in °C)}$$

– Pure W values.

Table 9.1-1 Physical and Mechanical Properties of Some W-Alloys (after Ref. [3])

	W	W–1%La$_2$O$_3$	W–5%Re	W–30Cu ~50 vol% W	W–Ni–Fe ~95 wt% W	W–Ni–Cu ~95 wt% W
Density at RT, g/cm^3	19.3	18.9	19.4	14.0	18.0	18.0
Thermal expans. coeff. at RT, 10^{-6}/K	4.5	4.7	4.5	11.5	5.5	5.2
Thermal cond. at RT/1000°C, W/mK	145/113	120/98	70/83	300/~220	83/-	108/-
Elastic modulus at RT, GPa	410	~410	400	218	380	350
Ultimate strength at RT, MPa	1000	900	1100	520	850	680
Poisson ratio	0.28	(0.3)	0.3	0.3	~0.3	~0.3
Tensile elongation at RT/1000°C, %	<0.4/25–30	<0.4/25–30	~1/13	~3/	16/	3/
Specific heat at RT, J/gK	0.14	0.14	0.14	0.24	0.19	0.18
DBTT, °C	100 ~ 400	~ as W	50 ~ 200	(<RT)	(<RT)	(<RT)
Recrystallization temperature, °C	1150–1350	1250–1700	>1500			
Melting point, °C	3410	~ as W	~3300	1080(Cu)	~1400	~1050
Max. temperature of application	$\leqslant$ 3410	~ as W	($\leqslant$ 3300)	$< T_{\mathrm{melt}}$	$\ll T_{\mathrm{melt}}$	$\ll T_{\mathrm{melt}}$
Vapor pressure at 2000°C, Pa	1.3×10^{-7}	> as W	$\geqslant$ as W	(Cu)	(Ni)	(Cu)
Atomic number	74	(74)	(74)	(49)	(67)	(68)
Atomic weight	183.8	(183.)	(184)	(117)	(166)	(167)
Cross section for thermal neutrons, *b*	18.5	(18.)	(21.8)	(10.4)	(16.3)	(16.5)
Estimated neutron leakage (W = 100%)	1.0	~1.0	~1.0	0.5	0.8	0.85
Estimated costs: (as of late 1997)						
Material, US$/kg	~150	W, +20%	~400			
Machining	High	Low	Medium	Low	Low	Low
Joining possible:						
Brazing	Yes	Yes	Yes	Yes	Yes	Yes
Welding	No (?)	No	No ?	No	No	No

9.2.3. Elongation

$e_{tot}(\%) = 20.8 + 0.053*T - 2.18\times10^{-5}*T^2$ (T > 500˚C)

– Pure W values.

9.2.4. Elastic Constants

E_Y (GPa) $=398 - 0.00231*T - 2.72\times10^{-5} T^2$ (T in ˚C)

– Pure W values; W-25Re E_Y at 20˚C = 410 GPa.

$\nu = 0.279 + 1.09\times10^{-5}$ T (T in ˚C); W-25Re ν at 20˚C = 0.30.

9.2.5. Thermophysical Properties

α_m (10^{-6}/˚C) $= 3.9 + 5.8\times10^{-5}*T + 5.7\times10^{-11}*T^2 - 2.0\times10^{-14}*T^3$ (T in ˚C)

– Pure W values.

C_P (J/kg-K) $= 128 + 0.033*T - 3.4\times10^{-6}*T^2$ (T in ˚C)

– Pure W values.

K_{th} (W/m-K) ~ 85 W/m-K (1000˚-2400˚C)

– Conductivity decreases with increasing Re content**.**

9.2.6. Recommended Operating Temperature Limits (Structural Applications)

T_{min} = 800˚C (due to radiation-induced increase in DBTT at low T_{irr}).
T_{max} = 1400˚C (Li, Pb-Li corrosion/chemical compatibility and thermal creep).

9.3. Summary of Radiation Effects in Refractory Metals

- Void swelling is not anticipated to be a lifetime-limiting issue due to the BCC structure of the high-temperature refractory alloys
  - Existing fission reactor data base indicate moderate swelling (<2%) for doses up to 10 dpa or higher.
  - Effects of fusion-relevant He generation on swelling is uncertain.
  - Swelling regimes are ~600˚C to 1000˚C for all 4 classes of refractory alloys.

- Radiation hardening can lead to a large increase in the ductile to brittle transition temperature. The radiation hardening in BCC alloys at low temperatures ($<0.3T_M$) is typically pronounced even for doses of ~1 dpa. The amount of radiation hardening typically decreases rapidly with irradiation temperature above $0.3T_M$, and radiation-induced increases in the DBTT may be anticipated to be acceptable at temperatures above ~0.3 T_M (although experimental verification is needed).

- The Group V alloys (V, Nb, Ta) exhibit better ductility before and after irradiation compared to Mo, W
  - Very limited mechanical properties data base on irradiated Nb, Ta alloys (qualitative trends can be inferred from the larger database on irradiated V alloys).
  - A moderate mechanical properties data base exists for irradiated Mo alloys (but at relatively low irradiation temperatures); the irradiated W database is very limited.
- Very limited or no fracture toughness/Charpy impact data exist on irradiated high temperature refractory alloys:
  - Tensile DBTT" of Mo, W alloys increases to very high values even for low dose irradiations at moderate temperatures (e.g., 600˚C after ~1 dpa irradiation at 300˚C for W, W-10Re)
- Radiation-enhanced recrystallization and/or radiation creep effects need to be investigated.

9.3.1. W and W Alloys: P/M or CVD W, W-1% La_2O_3, W-Mo-Y (Alloy W-13I)

- Tensile elongation ~0 for T_{irr} = 400˚C, 500˚C, 0.5-1.5×10^{26} n/m^2, $\leq$2 dpa irradiations at 700˚C are in progress.
- Un-notched bend bar DBTT > 900˚C for W, W-10%Re irradiated at 300˚C, 0.5×10^{26} n/m^2, (~1 dpa); most rapid embrittlement observed for W-10%Re.
  - ⇒ Estimated minimum operating temperature $\geq$800˚C, based on DBTT considerations (scaling from Mo alloy data base).

9.4. Coolant/Structure Chemical Compatibility

Chemical compatibility of high temperature refractory alloys with liquid metals and Flibe:

- In general, the refractory alloys have very good compatibility with the liquid metals and salts of interest for fusion applications
  - Impurity pickup is the key engineering issue.
- Li chemical compatibility data base:

  T-111 (Ta-8W-2Hf) data up to 1370˚C (good compatibility; static and circulating loops)

  Nb-1Zr data up to 1000˚C (good compatibility; static and circulating loops)

  W alloys up to 1370˚C (attack observed at $\geq$1540˚C)

  Mo alloys (TZM) up to 1370˚C (attack observed at $\geq$1540˚C).
- Chemical compatibility data base for Flibe (generally good compatibility with proposed structural metals)

The W/Li compatibility limit of ~1370°C used in Table 9.4-1, are based on an extensive series of tests by J.A. DeMastry (Battelle-Columbus labs) and other researchers performed in the mid-1960s (see refs. 6,7 for reviews). DeMastry observed good compatibility during 1000 h isothermal capsule tests at 1370°C, but corrosion/ dissolution during exposure at 1540 and 1650°C. Since dissolved tungsten was detected during post-exposure chemical analysis of the lithium, it seems unlikely that tungsten would be compatible with lithium for long-term (>>1000 h) operation at temperatures above 1400°C. On the other hand, some lithium heat pipe tests have found that W/Li was satisfactory for medium-term operation up to 1600°C. Mixed results on W/Li corrosion have been obtained in several other studies at temperatures >1400°C.

Table 9.4-1. Maximum Temperatures of Structural Alloys (bare walls) in Contact with High-Purity Liquid Coolants, Based on a 5 μm/yr Corrosion Limit

	Li	Pb-17 Li	Flibe
F/M steel	550°-600°C [1,2,3]	450°C [1,2,4]	700°C ? 304/316 st. steel [5]
V alloy	600°-700°C [1,6,7]	~650°C [1,8]	?
Nb alloy	>1300°C [9,10]	>600°C [8] (>1000°C in Pb) [11]	>800°C [12]
Ta alloy	>1370°C [9,10]	>600°C [8] (>1000°C in Pb) [11]	?
Mo	>1370°C [9,10]	>600°C [8]	>1100°C? [13,14]
W	>1370°C [9,10]	>600°C [8]	>900°C? [13]
SiC	~550°C ? [15]	>800°C ? [16,17]	?

The temperature limits for low-stress conditions such as EVOLVE can be considerably higher than the reference temperature limits summarized in Table 9.1-1.

References

[1] S. Malang and R. Mattas, Fusion Eng. and Design **27**, 399 (1995).
[2] O.K. Chopra and D.L. Smith, J. Nucl. Mater. **155-157**, 715 (1988).
[3] P.F. Tortorelli, J. Nucl. Mater. **155-157**, 722 (1988).
[4] M. Broc, et al., J. Nucl. Mater. **155-157**, 710 (1988).
[5] J.R. DiStefano, ORNL/TM-12925/R1 (1995).
[6] K. Natesan et al., Fusion Eng. Design **27**, 457 (1995).
[7] O.K. Chopra and D.L. Smith, J. Nucl. Mater. **155-157**, 683 (1988).
[8] H. Feuerstein et al., J. Nucl. Mater. **233-237**, 1383 (1996).
[9] J.H. Devan et al., Proc. Symp. on Refractory Alloy Technology for Space Nuclear Power Applications, CONF-8308130 (1984) p. 34.
[10] J.R. DiStefano, J. Mater. Eng. **11**, 215 (1989).
[11] H. Shimotake, et al., Trans. ANS **10**, 141 (1967).
[12] W.D. Manley, Prog. Nucl. Energy, Series IV, **2**, 164 (1960).
[13] Y. Desai, et al., J. Metals **40**, 7 (1988) A63.
[14] J.W. Koger and A.P. Litman, ORNL/TM-2724 (1969).
[15] D.R. Curran and M.F. Amateau, Am. Ceram. Soc. Bulletin **65**, 10 (1986) 1419.
[16] P. Hubberstey and T. Sample, J. Nucl. Mater. **248**, 140 (1997).
[17] J.S. Tulenko and G. Schoessow, Trans. ANS **75**, 72-73 (1996).

9.5. High Temperature Creep Strength Limits

The upper and lower temperature limits for W alloys are highly uncertain, due to a lack of relevant fracture toughness data (low temperature radiation hardening) and uncertainties in the design creep strength. The upper temperature limit of 1250°C that has been suggested for the APEX EVOLVE study is based on thermal creep of recrystallized W (1% creep in 1000 h at 150 MPa; this would correspond to similar amount of creep at ~100 MPa at 10,000 h). The temperature limit of 1250°C is clearly conservative, since stress-relieved tungsten has higher creep strength. If the design stress is less than 100 MPa then much higher temperatures can be allowed. Temperatures as high as 1400°C may be acceptable for W alloys in the EVOLVE Li-cooled design. Tungsten should be compatible with Li up to at least 1370°C based on experimental studies reviewed by DeVan and DiStefano (Refs. [9,10] after Table 9.4-1). Good compatibility was observed during 1000 h isothermal capsule tests at 1370°C, however, corrosion/dissolution during exposure at 1540° and 1650°C was also witnessed. Since dissolved tungsten was detected during post-exposure chemical analysis of the lithium, it seems unlikely that tungsten would be compatible with lithium for long-term (>>1000 h) operation at temperatures above 1400°C.

9.5.1. Larson-Miller Based High Temperature Creep Strength Limits of W-Alloys

The limited data base on the temperature creep strength limits of W-alloys calls for the use of Larson Miller parameters (m) , which correlate Temperature (T) with the time to failure (t_r) at constant engineering stress (σ) by:

$$T\,(\log t_r + C) = m \tag{9.5.1}$$

where C is a constant that depends on the alloy. Hence, if C is known for a particular alloy, one can find m in single test. From this result, one can then find the rupture times at any temperature, as long as the same engineering stress is applied. The table below shows some typical values of the constant C for different alloys of the Larson Miller equation.

Table 9.5-1. The Constant C of Various Alloys for the Larson-Miller Equation [1]

Material	Larson-Miller (C)
Various Steels	~20
S-590 Alloys	17
A-286 SS	20
Nimonic 81A	18
1-Cr-1Mo-0.25V Steel	22

A simplified tensile design stress can be defined as the minimum value of 1/3 of the ultimate or 2/3 of the yield strength, whichever is smaller.

As an initial approach to determining a design stress limit the lesser of the 10-year creep stress limit and the tensile design stress limit is used. The Larson Miller based creep rupture behavior of pure W, as well as numerous W-Re and W-Re-HfC alloy has been reported in are reproduced in Figures 9.5-1 through 9.5-9 along with the estimated tensile design stress (σ_{design}) limits [2-11].

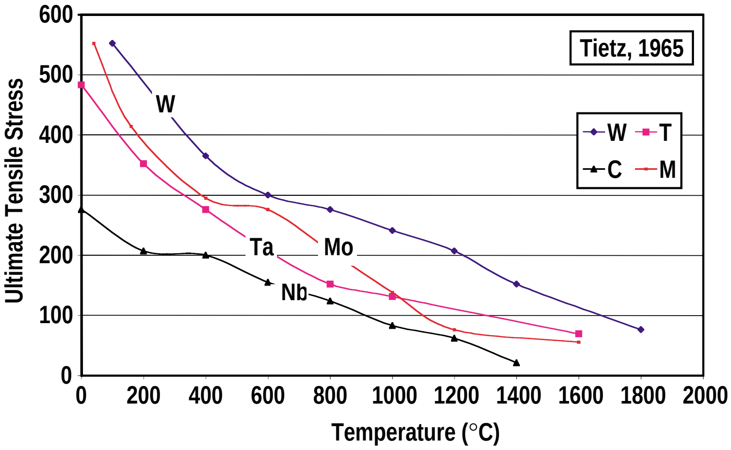

Figure 9.5-1. Comparison of tensile behavior of some refractory metals [2].

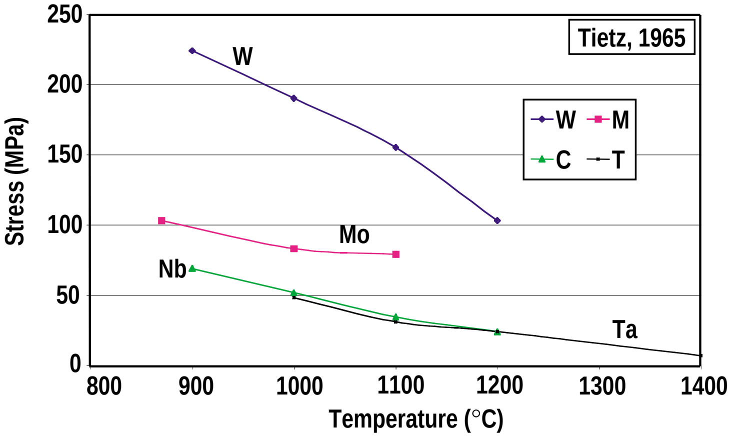

Figure 9.5-2. High-temperature creep strength of refractory metals (100 h test results) [2].

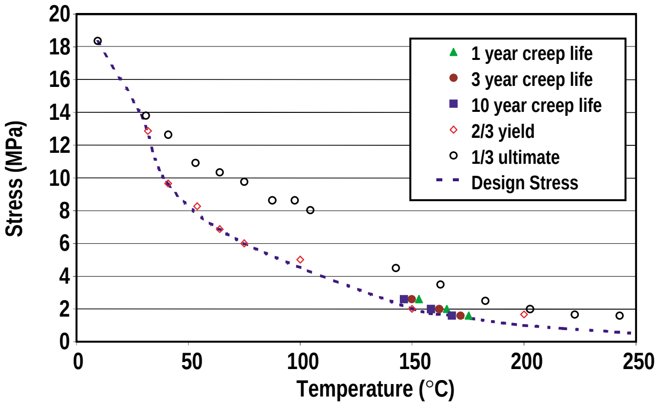

Figure 9.5-3. Larson-Miller based creep rupture of pure W (arc-melted, recrystallized) [3,4].

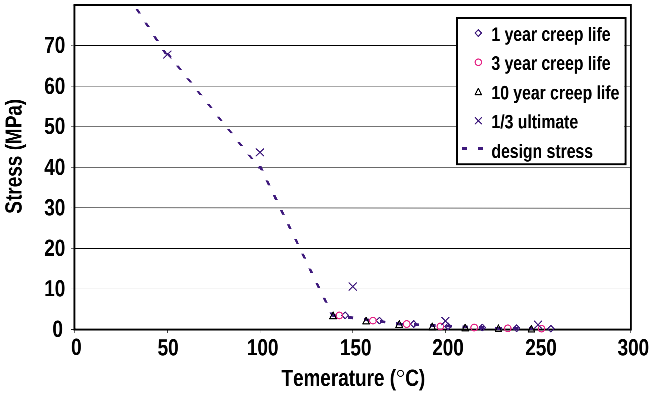

Figure 9.5-4. Larson-Miller based creep rupture of pure W (wrought, as-cast, tested in hydrogen) [5,6].

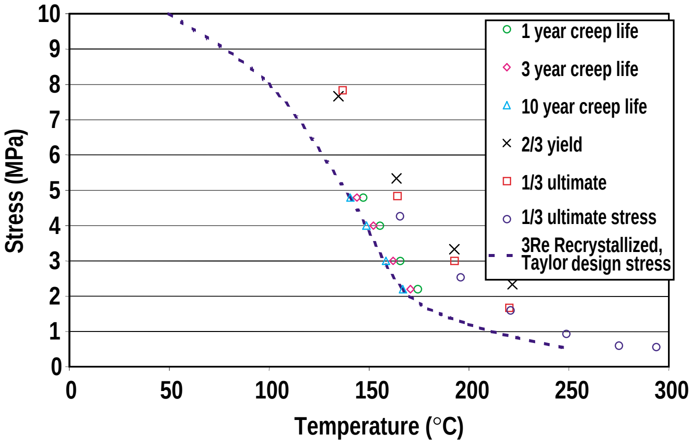

Figure 9.5-5. Larson-Miller based creep rupture of W-5Re (arc-melted, recrystalized) [4,7,8].

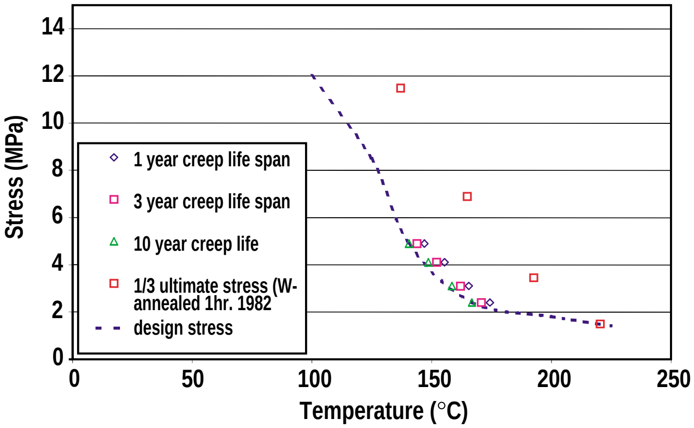

Figure 9.5-6. Larson-Miller based creep rupture of W-26Re and W-24Re (arc-melted, recrystalized and annealed) [4,9].

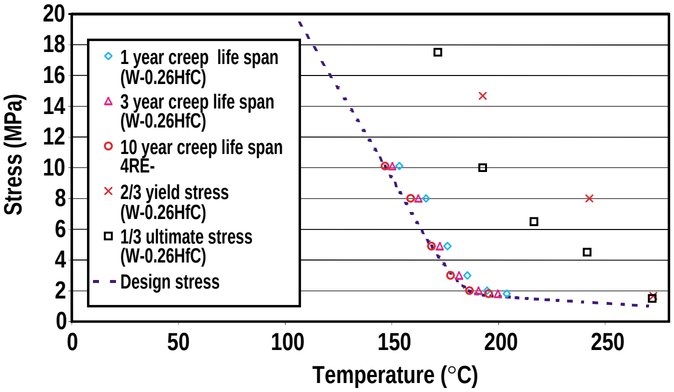

Figure 9.5-7. Larson-Miller based creep rupture of W-4Re0.26HfC and W-3.6Re-0.26HfC (arc-melted, recrystallized) [4].

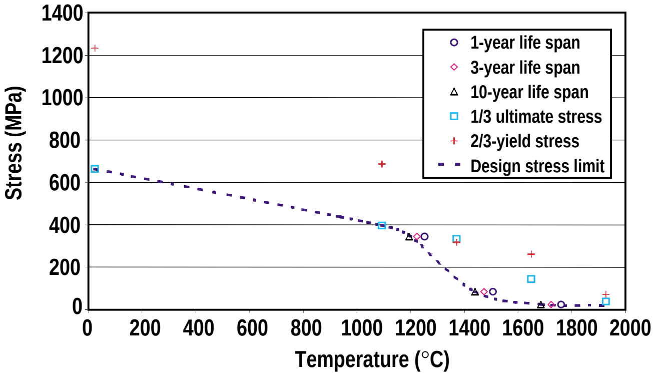

Figure 9.5-8. Larson-Miller based creep rupture of W-23.4Re-0.27HfC along with estimated design stress limit (arc-melted, swaged) [4,10].

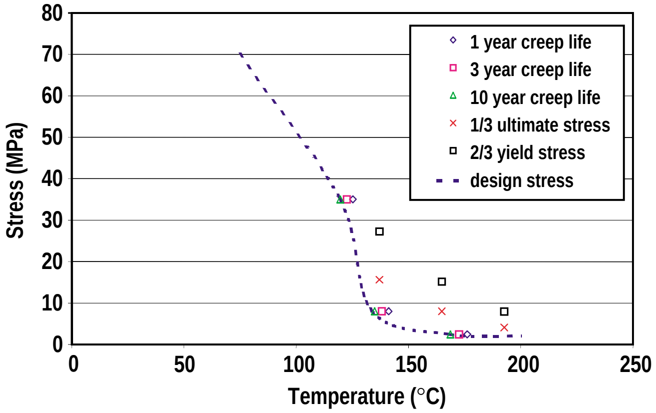

Figure 9.5-9. Larson-Miller based creep rupture of W-23.4Re-0.27HfC (arc-melted, recrystallized) [11].

Figure 9.5-10 shows the Larson-Miller master plot for pure W, W-4Re-0.26HfC, and W-23.4Re-0.27HfC. The Larson-Miller based design stress limits as a function of temperature of various W-alloys are compared and Figures 9.5-11 and 9.5-12 summarizes the design stress limit calculations for all of the considered W-alloys as a function of temperature. Almost all of the alloys experience a sharp drop in strength between 1000° and 1500°C.

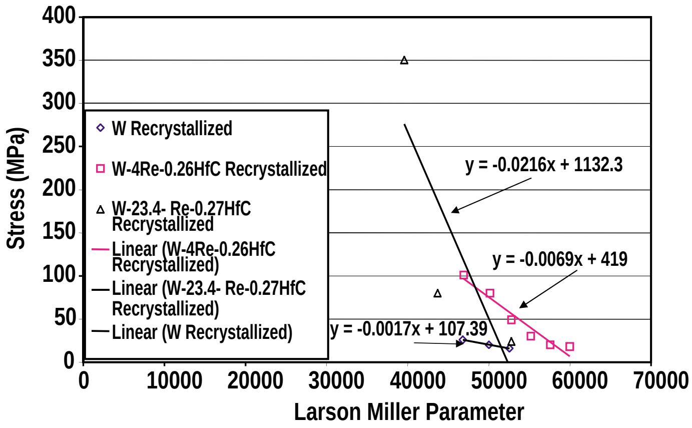

Figure 9.5-10. Larson-Miller master plot for pure W, W-4Re-0.26HfC, W-23.4Re-0.27HfC (all recrystallized).

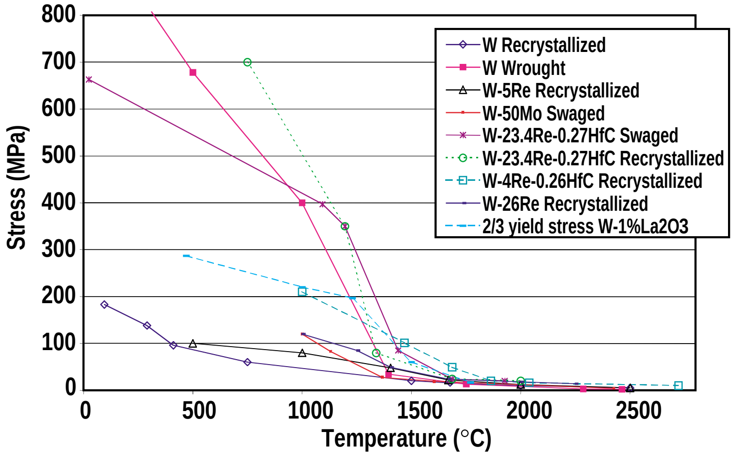

Figure 9.5-11. Comparison of design stress limits of W-alloys (all recrystallized) (30°C < T < 2500°C).

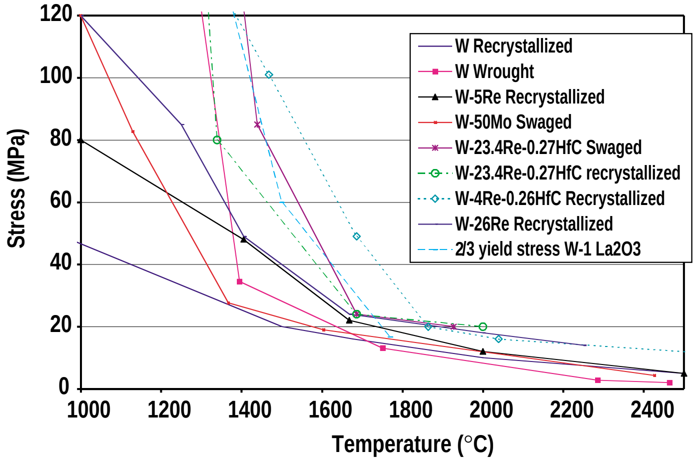

Figure 9.5-12. Comparison of high-temperature design stress limits of W-alloys (1000°C < T < °C).

Below 1400°C the W-23.4Re-0.27HfC swaged and recrystallized alloy are estimated to have the highest design stress capability relative to the other alloys including pure W (Figure 9.5-11). Above 1400°C (Figure 9.5-12) the W-4Re-0.26HfC shows the best design stress limit with

100 MPa at (~1400°C) down to 20 MPa at (~1850°C). Results of calculations for design stress limits at 1250°C are summarized in Table 9.5-2.

Table 9.5-2. Design Stress Limits of Various W-Alloys Based on Larson-Miller Calculations at 1250°C

Allloy	Design Stress* (MPa)
W-4Re-0.26HfC (re-crystallized)	150
W-wrought	160
W-1%La2O	190
W-23.4Re-0.27HfC (re-crystallized)	250
W-23.4Re-0.27HfC (swaged)	300

*The DESIGN STRESS is defined as the lesser of the 10-year creep stress limit and the tensile design stress limit (which is min or 1/3 ultimate or 2/3 yield).

The temperature limits for low-stress conditions such as EVOLVE can be considerably higher than the reference temperature limits summarized in previous APEX reports (interim APEX Report). Creep data for tungsten and W alloys are available at higher temperatures and lower stresses. A 150 MPa, 1000 h creep limit were cited in the APEX interim report as a typical structural material "example." As the EVOLVE design reaches further maturity, the design stresses and temperatures can be checked against the thermal creep database. For example, the 1% creep limit for W at 1400 C (10,000 h test) is ~25-30 MPa (Figure 9.5-13).

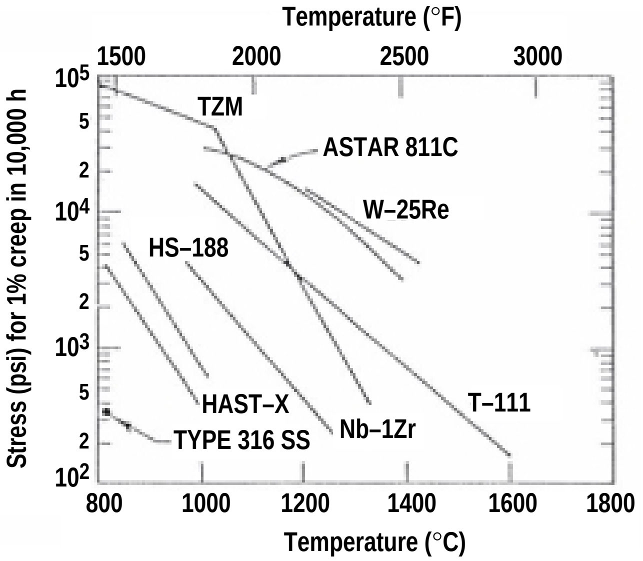

Figure 9.5-13. One-percent creep stress versus temperature of various high-temperature alloys.

References

[1] M.A. Meyers, *Mechanical Behavior of Materials*, Prentice Hall, United Kingdom (1998) p. 550.

[2] T.E. Tietz and J.W. Wilson, *Behavior and Properties of Refractory Metals*, Stanford, Calif., Stanford University Press (1965), p. 195.

[3] Sims, “Properties of Refractory Alloys Containing Rhenium,” Trans. ASM **52**, 929 (1960).

[4] Shin, “High Temperature Properties of Particle Strengthened W-5Re,” JOM, 12-15 (1960).

[5] Tajime, “The Tensile Strength of Tungsten Wires at High Temperatures,” Hantaro Nagaoka Anniversary Volume, Tokyo (1925).

[6] Flagella, “High Temperature Creep Rupture Behavior of Unalloyed Tungsten,” GE-NMPO, GEMP-543.

[7] Vandervoort, “Creep Behavior of W-5Re,” Met. Trans. **1**, 857-864 (1970).

[8] Taylor, “Tensile Properties of W-3%Re in a Vacuum,” J. of the Less Common Metals **7**, 27 (1964.

[9] Klopp, *Refractory Metals and Alloys IV-Research and Development*, Gordon-Breach, New York (1967) p. 557.

[10] Klopp, “Mechanical Properties of a Tungsten 23.4%Re-0.27%HfC Alloy,” J. of the Less Common Metals **24**. 427-442 (1971).

[11] Witzke, “Mechanical Properties of a Tungsten 23.4%Re-0.27%HfC Alloy,” J. of the Less Common Metals **24**, 427-442 (1971).

9.6. DBTT

The ductile-to-brittle transition temperature (DBTT) of unirradiated W-alloys depends primarily on the production history and the alloying elements. Figure 9.6-1 shows the range of DBTT for various W-alloys having been exposed to different thermomechanical treatments, with the as-rolled having the lowest DBTT, followed by recrystallized, and then the solution annealed alloys. However, the DBTT’s reported for advanced W-alloys, such ass W-Re-HfC are based on tensile tests. These data cannot be used to give a reliable estimate of the fracture toughness DBTT. Thus, even though the reported DBTT of W-Re-HfC are impressive, it is not clear what quantitative advantage is gained with W-Re-HfC alloys.

Reports on the effects of neutron irradiation on W-alloys are scarce, however, almost all W-alloys tested to-date experience a significant increases in DBTT anywhere from 200°C to >1000°C [1-5]. Figures 9.6-3 and 9.6-4 show the typical response of tungsten (BCC metals) to neutron irradiation at low temperatures: the yield strength increases with irradiation, while the ductility is reduced.

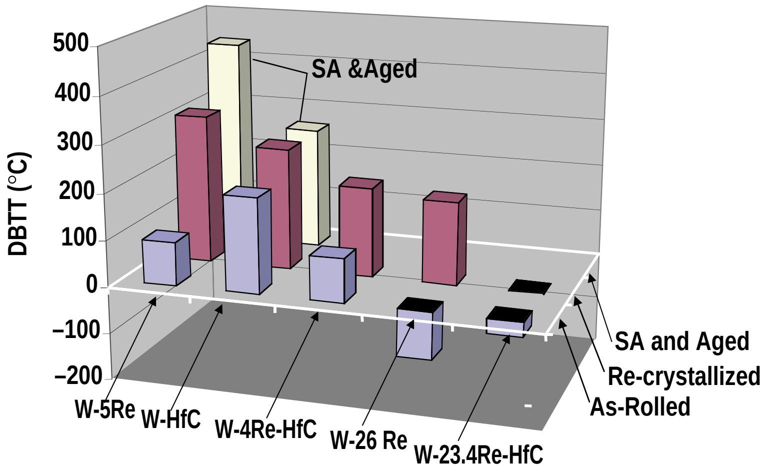

Figure 9.6-1. Approximate tensile ductile-to-brittle transition temperatures of unirradiated W-alloys having a thermal history based on solution annealed (SA), recrystallized, and as-rolled.

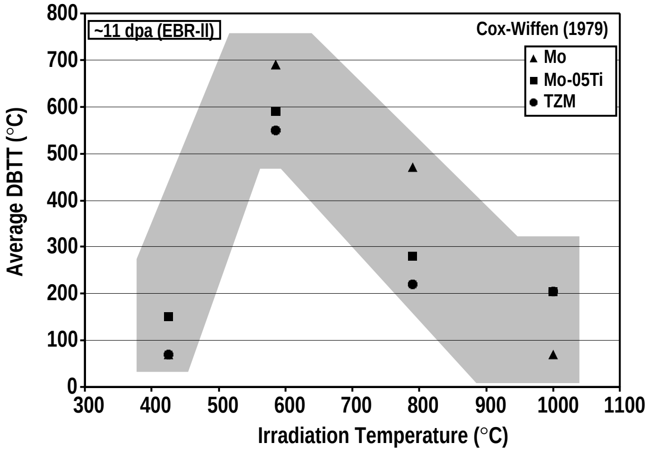

Figure 9.6-2. Effect of irradiation temperature on the tensile DBTT of Mo and TZM alloys after 11 dpa exposure in EBR-II [6].

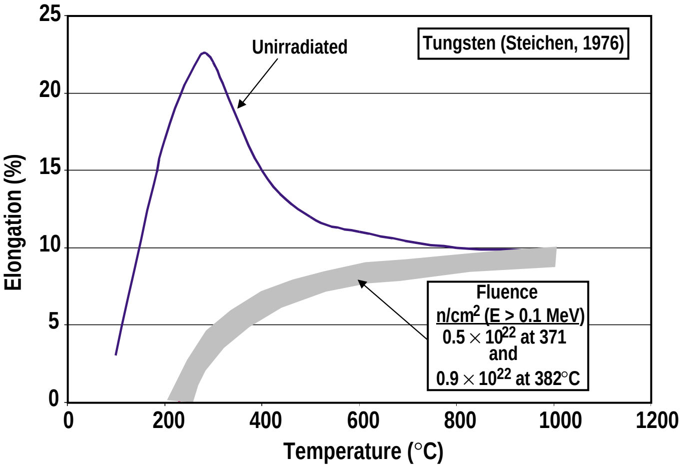

Figure 9.6-3. Effect of irradiation on the ductility of W as a function of test temperature for irradiated and unirradiated W [7].

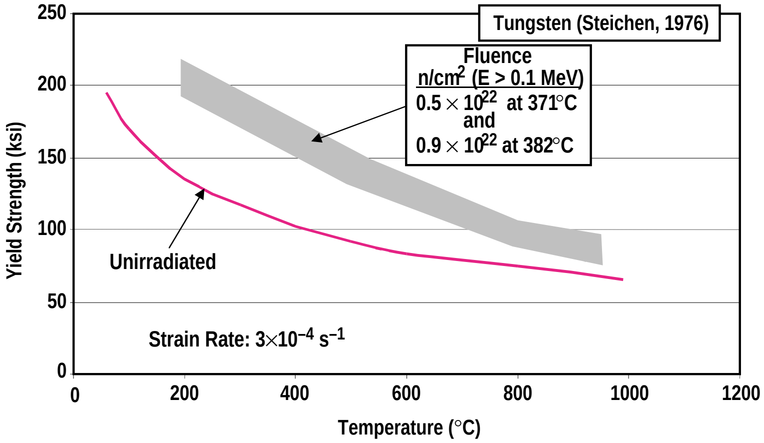

Figure 9.6-4. Effect of irradiation on the yield strength as a function of test temperature for irradiated and unirradiated W [6].

Radiation hardening in metals can be attributed to the production of a variety of defects, such as:

1. Point defects (vacancies and interstitials).
2. Impurity atoms (atomically dispersed transmutation products).
3. Small vacancy clusters (depleted zones).
4. Dislocation loops (faulted or unfaulted, vacancy or interstitial type).
5. Dislocation lines (unfaulted loops that have joined the dislocation network of the original microstructure).
6. Cavities (voids and helium bubbles).
7. Precipitates (sigma-phase and chi-phase precipitates in W-Re [8]).

Of these defects, the depleted zones are considered to be highly responsible for changes in DBTT of BCC metals, thus only depleted zones will be modeled to predict the possible response of W-alloys to neutron irradiation at elevated temperatures. The results of this model are therefore to be used with caution until they can be checked against experimental results.

Therefore, a phenomenological approach is chosen here in order to make an educated guess of the effects of neutron irradiation and of operating temperature on the DBTT of W-alloys. Neutron irradiation produced hardening in the refractory metals can be annealed out at elevated temperatures. Therefore, it is expected that elevated temperature operation will result in a decrease of the DBTT shift in W-alloys.

Relative to Mo-alloys [6,9] the database of neutron irradiation effects on W-alloys is much smaller. The phenomenological model is rooted in the assumption that Mo, TZM, and W alloys will exhibit similar rate of changes in their DBTT as a function of irradiation temperature. The approach is based on the assumption that these alloys primarily will experience increases in DBTT due to friction-hardening. However, the onset of friction hardening and annealing will be shifted to higher temperatures for W-alloys relative to Mo-alloys.

9.6.1. Phenomenological DBTT Model

The forces responsible for resisting motion of a dislocation through the crystal can be characterized as long range or short range. The total applied shear stress necessary to move the dislocation is the sum of the long-range and short-range stresses:

$$\sigma_{\mathrm{friction}} = \sigma_{LR} + \sigma_s \tag{9.6.1}$$

where $\sigma_{friction}$ is the friction stress and the subscripts *LR* and *s* represent the long-range and short-range contributions, respectively. The long-range forces arise from the repulsive interaction between the moving dislocation and the components of the dislocation network of the solid, while the short-range forces are due to obstacles that lie in the slip plane of the moving dislocation. The short-range forces are active only when the mobbing dislocation comes very close to or contacts the obstacle. The friction stress due to a dispersion of barriers depends on the average separation between the obstacles in the slip plane of the moving dislocation. The increase in short range stress (σ_s^o)is proportional to $N^{1/2}$ (N: number density of depleted zones) [10]:

$$\sigma_s^o = \left[\frac{U_o}{4(2/3)^{1/2}}\right]^{3/2} \frac{1}{b^2 G^{1/2}} \frac{N^{1/2}}{r} \tag{9.6.2}$$

where U_o is the cutting energy for a dislocation, b the burgers vector, G the shear modulus, r the radius of obstacle and N is the number density of depleted zones. The effect of temperature on the depleted-zone hardening can be expressed by:

$$\sigma_s = \sigma_s^o \left[1 - \left(\frac{T}{T_c}\right)^{2/3}\right]^{3/2} \tag{9.6.3}$$

where T_c is the characteristic temperature at which the depleted zones are annealed out (about 0.44 T_m).

The saturation of radiation hardening, in the absence of destruction mechanism, is based on the time rate of change of fast-neutron induced clusters (depleted zones N):

$$\frac{dN}{dt} = \alpha\, \Sigma_s \phi (1 - \nu N) \tag{9.6.4}$$

where α is number of cluster zones per neutron (~1), Σ_s is the macroscopic scattering cross-section, *v* is the capture volume around a depleted zone, and Φ is the neutron fluence. Integration of the preceding differential equation yields:

$$N(t) = \left(\frac{1}{v}\right)\left[1 - \exp(-\sigma \Sigma \phi v t\right] \quad . \tag{9.6.5}$$

Thus in the absence of a depleted zone destruction mechanism the friction stress is proportional to N(t). However, thermal annealing is a potential mechanism for destroying depleted zones. Thermal annealing of depleted zones at high temperatures affects the zones number density, which can be expressed using the depleted-zone decay time (τ), which is a function of the temperature. Thus the number density of depleted zones can be approximated using:

$$N(T,t) = \left\{ \frac{1}{\nu + [1/\alpha \sum \phi \tau(T)]} \right\} \left(1 - \exp\left\{ -\left[\alpha \sum \phi \nu + \frac{1}{\tau(T)} \right] \cdot t \right\} \right) \quad . \tag{9.6.6}$$

Calculated number densities of depleted zones in Mo and W based on a fluence of 2.5×10^{26} n/m^2 and 5×10^{25} n/m^2 are shown in Figures 9.6-5 and 9.6-6, respectively. The corresponding changes in the friction stress of these two materials are shown in Figures 9.6-7 and 9.6-8. The calculated changes in the DBTT of Mo are within the range of the experimental data (Figure 9.6-9). Therefore, the calculated changes in the DBTT of tungsten, based on the same model can serve as a first approximation. The predicted changes in the DBTT of tungsten might fall within experimental data. The model shows that at operating temperatures above 1000°C, the DBTT of W alloys will not be drastically affected (Figure 9.6-10).

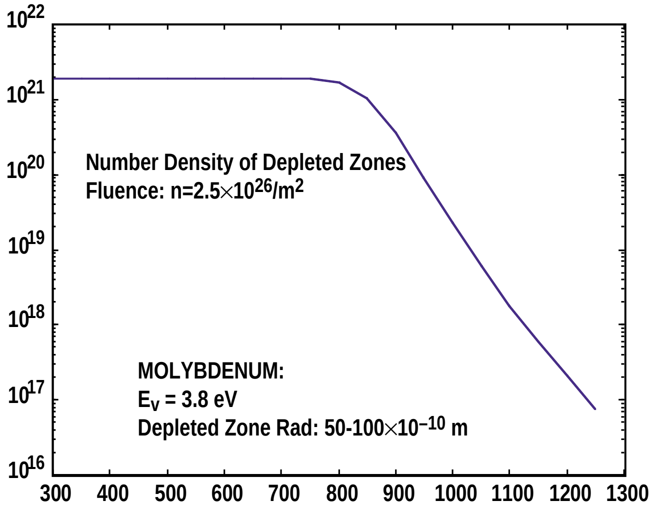

Figure 9.6-5. Calculated number of depleted zones in molybdenum as a function of temperature.

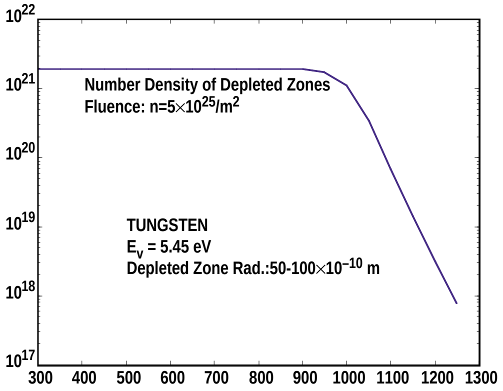

Figure 9.6-6. Calculated number density of depleted zones in tungsten as a function of temperature.

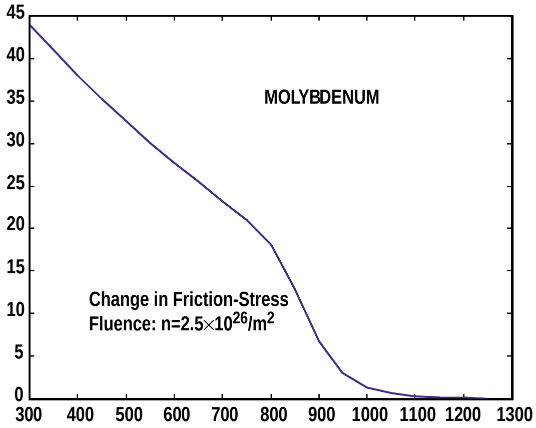

Figure 9.6-7. Calculated change in friction stress (σ_s) in molybdenum as a function of temperature.

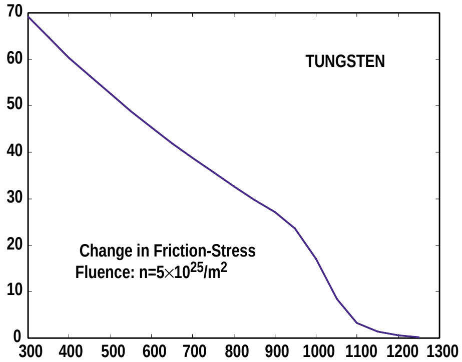

Figure 9.6-8. Calculated change in friction stress (σ_s) in tungsten as a function of temperature.

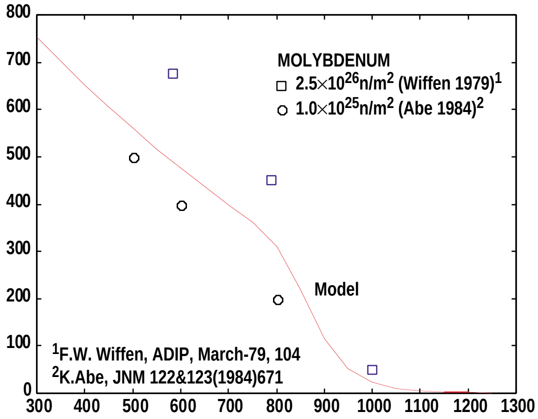

Figure 9.6-9. Calculated (solid line) and experimental (data points) values of the average DBTT of recrystallized and of neutron irradiated Molybdenum as a function of temperature.

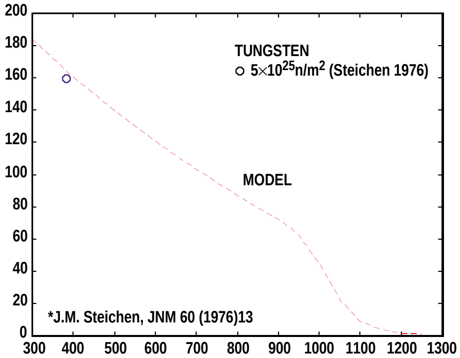

Figure 9.6-10. Calculated (solid line) and experimental (data point) value of the average DBTT of f neutron irradiated tungsten as a function of temperature.

In conclusion, the use of W-alloys at elevated temperature (above 1000°C) in EVOVLE should not result in a drastic increase in the DBTT. Therefore, it recommended that EVOVLE uses the materials parameters previously recommended by the APEX team (Chapter 13 in the APEX interim report).

References

[1] J.W. Davis, et al., J. Nucl. Mater. **258-263**, 308-312 (1998).
[2] V. Barabash, et al., Physica Scripta **T81**, 74-83 (1999).
[3] V. Barabash, et al., J. Nucl. Mater. **283**, 138-146 (2000).
[4] G.M. Kalinin, et al., J. Nucl. Mater. **179-181**, 1193 (1991).
[5] I.V. Gorynin, et al., J. Nucl. Mater. **191-194**, 421-425 (1992).
[6] B.L. Cox, et al., J. Nucl. Mater. **85-86**, 901-905 (1979).
[7] J.M. Steichen, J. Nucl. Mater. **60**, 13-19 (1976).
[8] R.K. Williams, et al., Metal. Trans., **14A**, 655-665 (1983).
[9] K. Watanabe, et al., J. Nucl. Mater. **258-263**, 848-852 (1998).
[10] D.R. Olander, “Fundamental Aspects of Nuclear Fuel Elements,” ERDA (Energy Research and Development Administration), TID-26711-P1 (1976).

9.7. EVOLVE’s Base-line W-Alloy

Although the Larson Miller estimates indicated a higher design stress limit for W-Re-HfC based alloys than simple W-Re alloys, it is recommended to keep W-5Re as the "reference" tungsten alloy for the APEX Evolve design, because a reasonably full set of physical and thermomechanical properties are available for this material.

Recent efforts to fabricate any high-quality W-TiC specimens have not materialized, however, pending delivery of such samples tests are planned at ORNL. The dispersion strengthened tungsten alloys may offer some improved performance, but the necessary fracture toughness measurements, etc. have not yet been performed. Based on 1999 results obtained on Mo-TiC specimens irradiated in HFIR, the TiC dispersion may not provide effective resistance to radiation embrittlement in the refractory metals.

9.8. Recommendations for Developing New W-Alloys

Regarding the strategy for new W alloys, it is clearly a daunting task to develop an improved refractory alloy (various programs have been trying to do this off and on for ~40 years). It is likely that the un-irradiated low-temperature (<300°C) mechanical behavior of all existing tungsten alloys might be strongly influenced by impurities.

One possible development approach for tungsten alloys might focus on fabricating and determining the properties of ultra-high purity tungsten (including interstitial impurities) to answer the question whether ductile tungsten can be produced simply by applying modern impurity control processes or by adding appropriate mass-balanced impurity gettering agents. There is some evidence that it is possible to produce high ductility Mo alloys (at room temperature) using intragranular Zr doping. However, this approach has not yet been demonstrated for the other group VI refractory metals, except for the so-called tungsten heavy alloys (W-Fe-Ni). The short synopsis of the current situation regarding W-alloys is that all of the available alloys have shortcomings, and there is no obvious development path for producing improved material.

A small, targeted research program that at least shows there is a light at the end of the tunnel would be the best strategy for developing W alloys for fusion. However, using realistic assumptions for available budgets, it will take years before an impact of this R&D will be seen. Success is not ensured even if there was a significant amount of available funding (remember that other programs have spent decades trying to develop improved W alloys). The Materials Program “B-budget” presented recently at the VLT meeting (Aug. 2000) Germantown included a moderate-sized (~270k$/yr.) task on refractory alloys.

Regarding the W alloy development issue, since we do not understand why W can be ductile with alloying, it will be futile to develop a whole series of alloys with out first directing our attention to the science issues related to the ductility (or lack thereof) of W and its alloys. Recently, W alloy research proposal have been suggested, which in essence extend the current W-Re and W-TiC alloys. However, first thorough understandings of the underlying physical mechanisms, which produce improved ductility in W-Re (and perhaps W-TiC), are needed before more complicated alloys are made.

A similar comment could be made regarding W-Fe-Ni. Once the role of Ni in the heavy alloys is understood, then a reduced-activation substitute element can be chosen. The main problem with W-Fe-Ni alloys is that the upper operating temperature would be much lower than conventional W alloys - probably too low for use in EVOLVE. We should direct our attention to the science issues related to the ductility (or lack thereof) of W and its alloys.

As far as Evolve is concerned, we can use the properties of W-Re alloys for the time being, while an effort is made at the science front.

10. Conclusions and Critical Issues

Task IV of the Chamber Technology APEX program has made significant progress in the understanding of the application of refractory W-alloy for the FW/blanket design in order to achieve the very high gross thermal efficiency of 57%. We completed the second phase evaluation of the EVOLVE FW/blanket concept in which cooling is by vaporized lithium. During this phase, critical areas were evaluated and the results have provided us with further confidence in the possibility of utilizing this innovative concept to achieve a passively safe and high thermal performance FW/blanket design for fusion power reactors. We show that this innovative concept can minimize the problem of irradiation embrittlement of W-alloy by utilizing a low operating Li-vapor pressure of less than 0.5 atm. We also find that this first wall and blanket concept should have no problem in achieving adequate nuclear performance. Even though W-alloy will produce relatively high afterheat, with the addition of passive cooling loops, the concept has a strong possibility of achieving the safety requirement of not needing a public evacuation plan under the loss of power accident condition. Due to the relatively low system pressure of the design, it is shown to be able to withstand a large number of cracks at the first wall (with the initial crack length of 25 mm and a width of 10 μm), without detrimental impact to plasma operation in terms of fuel dilution from the coolant lithium.

Fundamental issues remain and some of them can only be addressed by experiments. The transpiration-cooled first wall approach is crucial to both the transpiration and boiling blanket concepts. For the transpiration-cooled first wall and blanket concept, we have identified the need to further quantify the data of lithium superheat from W-alloy heated surface and bulk lithium slabs. For the boiling blanket concept, based on previous work and the current state of knowledge regarding pool boiling of liquid metals in the presence of a magnetic field, a new experiment has been identified and initiated to study and identify stable boiling regimes. Real-time visualization of the developing flow patterns will be used. This experiment will allow us to determine the boiling rate and project the heat transfer for a given volumetric heat generation, which in turn will lead to the necessary pool depth determination to balance heat generation and heat removal. Fundamental issues of W-alloy properties under high neutron fluence and the technique of components fabrication are also very important. Satisfactory full-penetration welds have not yet been developed for W, despite intensive efforts over a >25 year time span (1960–1985). Studies have been initiated on W-alloy fabrication technology being developed for the helium-cooled FW/blanket design. Preliminary investigations of W-alloy fabrication and heat flux removal through SBIR programs have also been reported and results are encouraging.

Based on the performance advantages of the EVOLVE FW/blanket design and the identified critical issues, we recommend that the investigation of these issues be continued since this innovative design has a good possibility of achieving adequate nuclear performance, high thermal efficiency and passive safety, all of which are necessary characteristics for the utilization of fusion power.